CHARACTERIZATION AND DESIGN OF NON-ADIABATIC MICRO-COMPRESSOR IMPELLER AND PRELIMINARY DESIGN OF SELF-SUSTAINED MICRO ENGINE SYSTEM

by

Borislav T. Sirakov

Bachelor of Science in Aeronautical Engineering, United States Air Force Academy, 1999
Master of Science in Aeronautics and Astronautics, Massachusetts Institute of Technology, 2001

Submitted to the Department of Aeronautics and Astronautics
in partial fulfillment of the requirements for the degree of

Doctor of Philosophy
at the

Massachusetts Institute of Technology

February 2005

Author _____
Department of Aeronautics and Astronautics
September 29, 2004

Certified by _____
Dr. Choon-Sooi Tan
Senior Research Engineer, Committee Chairman

Certified by _____
Professor Alan H. Epstein
R. C. Maclaurin Professor of Aeronautics and Astronautics

Certified by _____
Dr. Yifang Gong
Research Engineer

Certified by _____
Professor Edward M. Greitzer
H. N. Slater Professor of Aeronautics and Astronautics

Certified by _____
Professor Hung Cheng
Minor Advisor, Associate Professor of Applied Mathematics

Certified by _____
Professor Jaime Peraire
Professor of Aeronautics and Astronautics
Chair, Committee on Graduate Students

Characterization and Design of Non-Adiabatic Micro-Compressor Impeller and Preliminary Design of Self-Sustained Micro Engine System

By
Borislav T. Sirakov

ABSTRACT

As part of the MIT research program on micro-engines (of size ~ 1 cm), this thesis defines concepts and designs to improve micro-turbomachinery and overall system performance.

Three-dimensional Reynolds-averaged Navier-Stokes computations (FLUENT) have been carried out to quantify the performance limiting processes in micro-impellers. These processes include (i) heat transfer to the compressor flow responsible for up to 25 points efficiency penalty, (ii) impeller casing drag (17 points penalty) and (iii) passage boundary layer loss (10 points penalty). The magnitude of the first effect is a result of the engine small length scale selection and is characterized by the total heat to impeller flow as fraction of inlet flow enthalpy. The magnitudes of the last two effects can be attributed to low Reynolds number. Scaling laws for elucidating the parametric controlling trend in these effects have been formulated.

A mean-line analysis and design tool based on the above micro-impeller characterization is developed to formulate design guidelines. The guidelines show that the optimal micro-impeller geometry changes with impeller wall temperature, an effect, not present for large turbomachinery. In particular, impeller inlet angle, back-sweep angle, solidity and radial size for peak efficiency decrease with increasing impeller wall temperature. This behavior is a result of the competing effects of geometry on (i) aerodynamic loss and (ii) on heat transfer to impeller flow. In accord with these findings, CFD calculations show that configuring a micro-impeller excluding the heat addition as a design variable can incur a penalty of more than 10 efficiency points.

An aero-thermal system model is developed to enable micro-engine system analysis and selection of system design parameters. It is shown that, in contrast to large engine design, an optimal turbine inlet temperature, associated with peak system efficiency, exists for the micro-engine thermodynamic cycle. This condition is related to the competition between the benefit in cycle performance associated with increasing turbine inlet temperature, and the degradation in compressor performance associated with increasing heat transfer. Furthermore, system efficiency approximately doubles as turbomachinery size is scaled up two times. This is related to the different scaling of heat transfer, parasitic power loss, and Reynolds number in micro-engines. Minimum requirements on advanced technology levels are established for a self-sustaining micro-engine.

Two designs, based on different advanced technologies, producing 10-20 Watts of net shaft power with chemical-to-shaft mechanical conversion efficiency of 1.5-2.0% are proposed for micro-engine development.

Thesis Supervisor: Dr. Choon-Sooi Tan
Title: Senior Research Engineer

I dedicate this thesis to my parents, Todor and Jivka Sirakovi.

ACKNOWLEDGEMENTS

The completion of this thesis would not have been possible without the support, encouragement, good will and friendship of great many people. I consider myself a very lucky person! Although I spent the last ten years away from my family and many of my dear friends I found many new friends, and great teachers here in America. My dream to learn at MIT was realized.

First I would like to thank my advisor Dr. Choon Tan for being a great mentor, teacher and friend for the last five years. I enjoyed working with Dr. Tan both for my Master and Doctoral degrees and I learned a great deal from him for which I am indebted. I would also like to thank the other members of my committee Prof. Alan Epstein, Dr. Yifang Gong, Prof. Edward Greitzer, and Prof. Hung Cheng for their guidance and teaching. I am grateful to Prof. Epstein for giving me the opportunity to join the micro-engine team and to participate in the design of the self-sustained engine and for teaching me so many things about gas turbines. I cannot thank enough Yifang for being such a great teacher and friend. Every single day Yifang was available for discussions and he was always happy to teach me something new. I would also like to thank Prof. Greitzer and Dr. Tan for revealing the secrets of internal flow to me. I would have been completely lost in my research without this knowledge. I thank my minor's advisor Prof. Cheng for showing me some amazing tricks in math and for enriching my mind.

My study at MIT would not have been possible without the encouragement and support by Dr. Bill Heiser, Col. Brenda Haven, and Gen. Michael Smith from the US Air Force Academy and Dr. David Quick from Rolls Royce for which I am grateful.

I would also like to thank the rest of the faculty, research and support staff, and the students at GTL for their teaching, friendship, and help. I thank Prof. Darmofal, Prof. Drela, Dr. Ehrich, Prof. Kerrebrock, Dr. Jacobson, Dr. Paduano, Dr. Guenette, Dr. Merchant, Dr. Li, Prof. Spakovszky, Prof. Spearing, Prof. Waitz, and Prof. Willcox for their help and teaching. I thank Lori Martinez, Holly Anderson, Diana Park, Suzan Parker, Julie Finn, Paul Warren, Barbara Lechner, and Marie Stuppard for their support and friendship. I also thank all my fellow students at GTL: Duc, Tony, Vai-Man, Nate, Juan, Kiril, Nayden, Parthiv, Kelly, Hyung-Soo, Taek, Jin-Woo, Jin-Wook, Spad, Chris, Nick, Dan, Alexis, Pierre, Jessica, Steve, Luis, Geoff, Caitlin, Benny, CJ, Sean, and Jeremy.

Finally, I would like to thank my family and my wife Nadia for their unconditional love through the years!

CONTENTS

LIST OF FIGURES

LIST OF TABLES

CHAPTER 1

1 INTRODUCTION

1.1 BACKGROUND

The increasing need for compact power sources for applications in portable electronic devices and robots has spurred research on miniaturized energy conversion devices. The pioneering concept was the micro-gas-turbine engine invented by Epstein at MIT, which has the potential of achieving high power density compared to batteries [1,2,3]. This is a centimeter-scale engine, which operates on a Brayton cycle with electric power generation as its primary application. Micro jet engines for propulsion, motor-driven compressors for fluidic pumping and pressurization, and micro rockets have also been proposed [4,5,6,7,8].

In the context here, a micro-engine is characterized by sub-millimeter component features (turbomachinery blade height and disk thickness, journal bearing gap and length, flow channel dimensions) and is expected to produce 10~20 Watts of electric power. This micro-electro-mechanical system (MEMS) device is manufactured from ceramic materials using semiconductor fabrication techniques (for silicon) and chemical vapor deposition (for silicon carbide). To build such an engine it is required to develop technologies for fabrication and operation of high speed turbomachinery, high speed gas bearings, advanced materials, high-temperature micro-scale packaging, compact combustion systems, and high power micro electrical motors and generators.

The original concept by Epstein led to a multidisciplinary research program at MIT to build high power density micro-gas turbine engines based on micro fabrication technology. The program was initiated in 1995 at the Gas Turbine Laboratory (GTL) and Microsystems Technology Laboratory (MTL). This thesis is part of the research effort to overcome the challenges in the design and development of micro engines.

1.2 STATEMENT OF TECHNICAL PROBLEM

The goal of the micro-engine project is to develop a micro-engine system that produces positive net power. One of the main technical challenges is the minimum requirement on micro-turbomachinery performance levels. Flow mechanisms in micro-turbomachinery that operates in non-adiabatic, low Reynolds number (1,000-10,000) conditions are qualitatively and quantitatively distinct from those in conventional scale turbomachinery. They constitute important sources of irreversibility and limit performance levels achievable in micro-turbomachinery. This thesis develops some of the key elements needed for the realization of micro-gas turbine engines technology. These include design and improvement in micro-turbomachinery, and development of an appropriate system model and methodology for overall micro-engine system design.

1.3 OVERVIEW AND PREVIOUS WORK

This section describes the layout of the micro-engine system, the constraints and limitations specific to micro-engines, and relevant previous work.

1.3.1 MICRO ENGINE SYSTEM LAYOUT AND MICRO-TURBOMACHINERY

The micro engine system consists of a rotating and a stationary component. The rotor includes the compressor impeller, turbine rotor blades and disks, and a thermal isolation shaft between the two disks. The rotor is supported by gas bearings – a journal bearing on the compressor outer perimeter side (or turbine side or both) and two thrust bearings on the compressor and turbine sides. The stationary part includes the compressor stator and turbine nozzle guide vanes, the annular combustor and the engine casing along with the flow paths – primary and secondary. The radial extent of the engine examined in the GTL is 1-2 cm. The engine thickness is about 5mm. The size of the engine and the turbomachinery can be seen in Fig. 1.1 ,which presents a micro-engine device with a standard postage stamp as background. The micro-impeller is shown in red.

The micro-turbomachinery explored for the micro-engine consists of a radial compressor and turbine with diameter in the range of 5mm to 20mm, peripheral speed ~ 400-500 m/s, and blade height of 200-1000 μm.

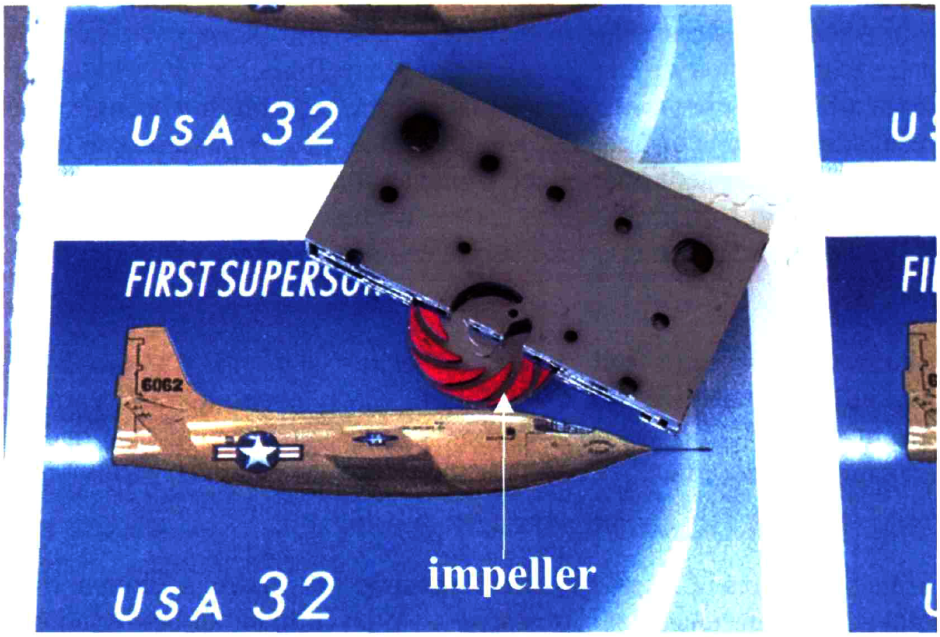

Figure 1.1 Micro-engine and micro-turbomachinery

1.3.2 CONSTRAINTS AND LIMITATIONS

The constraints and limitations on the design and manufacturing of micro-engines are the following:

- current micro-fabrication capabilities (etch depth, precision, and uniformity, two-dimensional extruded geometry)
- rotordynamic instabilities in gas bearings
- low Damkohler number, non-adiabatic combustor operation
- low Reynolds number, high Mach number, non-adiabatic turbo-machinery operation,
- material properties (Si and SiC) and behavior at elevated temperatures and stresses
- lack of accurate experimental measurement techniques and data

The two major barriers to self-sustained micro-engine operation are rotor dynamic instabilities preventing high-speed rotor operation and unexpectedly low turbomachinery performance. The focus in this thesis is on the challenges related to turbomachinery and its impact on system performance. Rotor dynamic issues will not be addressed in this work and rotor design speed will be assumed achievable.

Consequences of Current Micro-Fabrication Capabilities:

1. The micro-engine is constructed by bonding silicon wafers. Therefore, the overall size of the device and the components is limited by the ability to bond wafers and by the dimensions of the wafers. It will be shown that system performance improves with size.

2. The geometry of all parts is limited to two-dimensional, constant height, extrusions because all shapes are created by planar etching. Thus turbomachinery blade height is limited to a constant value in the component flow passages. Inability to tailor the hub and casing geometry of the flow passages in the impeller can lead to separation due to the large effective exit-to-inlet area ratios and the large density changes in the flow. This can results in blockage and reduced engine mass flow. Separation can also increase the flow angle at impeller exit and reduce work input and pressure ratio. Blade thickness can be used to control diffusion. This, however, leads to elongated passages with increased boundary layer loss, increased back sweep angle (reduced work input), and reduced mass flow.

3. Limits on minimum and maximum feature size that can be fabricated also exist. Maximum feature size puts a limit on the blade height, journal bearing depth, combustor height. Blade height in micro-turbomachinery controls passage hydraulic diameter and passage Reynolds number and thus the relative importance of viscous losses. Currently blade height is limited to 500 μm with possibility to increase to 1mm.

All of these features of micro-fabricated components impose additional limitations on micro-turbomachinery performance compared to conventional turbomachinery. Information on micro-fabrication techniques is given in references [9,10,11]

Micro-turbomachinery Requirements:

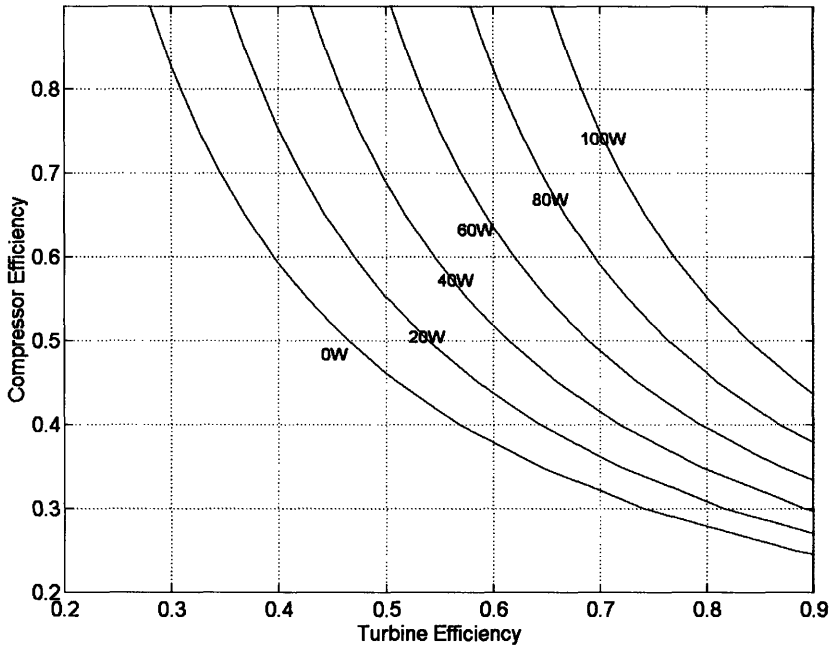

Figure 1.2 Power output at various compressor and turbine performance levels. Mass flow is set to 0.5 g/s, turbine inlet temperature to 1600 K, cycle pressure ratio to 2.5, combustor P_T loss to 5% of combustor inlet flow stagnation pressure, and parasitic power loss to 11W [12].

To examine the requirements on the micro-turbomachinery efficiency it is necessary to explain the figures of merit used in this thesis. Isentropic efficiency compares the actual work (absorbed or produced) to the ideal work (absorbed or produced) by the component for the same pressure ratio if the flow processes in the component were isentropic (reversible and adiabatic). Isentropic efficiency has the same meaning as when used for conventional large turbomachines and is applicable to micro-turbomachinery operating in both adiabatic and non-adiabatic conditions. For instance the micro-compressor isentropic efficiency is defined as follows:

$$\eta_{compressor} = \frac{W_{ideal}}{W_{actual}} = \frac{\dot{m} CpT_0(\pi^{\frac{\gamma-1}{\gamma}} - 1)}{W_{actual}} = \frac{\dot{m} CpT_0(\pi^{\frac{\gamma-1}{\gamma}} - 1)}{M\Omega} \tag{1.1}$$

where M is the torque for the rotating component, Ω is the rotating speed, W is the work, m is the mass flow, T is the temperature, π is the pressure ratio, γ is the specific heat ratio, and Cp is the specific heat at constant pressure of the gas.

The term adiabatic efficiency in this thesis has the same meaning as isentropic efficiency. However, it is used to assess the performance of components operating in adiabatic conditions only to avoid any confusion.

The term polytropic efficiency is used to describe the aerodynamic quality of turbomachinery operating in adiabatic conditions in the same way it is used for large machines.

Figure 1.2 describes the requirements on turbomachinery performance so the thermodynamic cycle can produce net work. The results are based on analysis of the micro-engine system by Gong [12]. Each line represents requirements on compressor and turbine isentropic efficiency to produce the indicated level of power output. The zero watts curve is the break-even requirement indicating that the engine can self-sustain without producing power.

To produce positive power both compressor and turbine in a representative micro-engine system must have sufficiently high isentropic efficiency (for example both about 50%, or compressor 30% and turbine 85%, or any other combination above the zero power curve). Figure 1.2 thus establishes representative minimum requirements on turbomachinery performance (combination of compressor and turbine isentropic efficiency) to produce specified engine net power (the different curves on the figure).

Since micro-turbomachinery operates in very different regime compared to conventional turbomachinery a major issue is whether micro-turbomachinery performance can meet the requirements for a break-even cycle. Micro-turbomachinery operates in a low Reynolds number (1,000-10,000), non-adiabatic regime. Performance is limited by low Reynolds number operation to efficiency values much lower than those for large-conventional machines. The performance penalty in impeller efficiency can be as high as 10-25 percentage points compared to 5 points for large impellers [13]. The mechanisms responsible for this penalty are predominantly casing drag and passage boundary layer loss as will be shown in Chapter 3.

Another factor responsible for low micro-turbomachinery performance level is heat transfer. Due to the large temperature difference between hot and cold sections in the micro-engine, the small length scales, and the high thermal conductivity of silicon, micro-turbomachinery operates in a non-adiabatic regime. Heat addition is another important source of irreversibility [12].

Structural Integrity: Any useful engineering device is designed for structural integrity and for certain life. The material of choice for the micro-engine is silicon and the allowable component stresses and temperatures are limited by the properties of silicon. The maximum allowed stress in silicon is a function of temperature. Pure silicon experiences rapid thermal softening at temperatures above 900 K, which is about 200-300 K lower than conventional turbomachinery materials and imposes additional design limitations. At the high stresses and temperatures encountered in rotating machinery silicon also experiences significant rates of strain deformation (creep). Thus the design for structural integrity and requirements on micro-engine life impose severe constraints on rotating speeds (pressure ratio), blade height and component geometry (mass flow), component temperature (maximum cycle temperature, net engine power). For additional information on material properties and behavior see references [14,15].

1.3.3 PREVIOUS WORK

Micro-turbomachinery: The following limiting mechanisms that determine micro-turbomachinery performance have been identified:

Reynolds number effects

Casey [16] experimentally investigated the effect of Reynolds number (based on blade exit span) on shrouded compressor stage efficiency. He measured about 10 points stage efficiency drop from large Reynolds numbers (70,000-120,000) typical for conventional impellers to low Reynolds numbers (about 20,000) representative of micro-impellers.

Gong [12] characterized micro-compressor diffuser performance in terms of Reynolds number and swirl parameter (ratio of tangential to radial absolute velocity at diffuser inlet) using 3-D CFD (FLUENT). He concluded that pressure recovery in micro-diffusers is insensitive to inlet swirl factor for a large range of swirl factors (5-50). The pressure recovery coefficient, however, was found to be about 0.5-0.6 at the low Reynolds number of operation. Such pressure recovery is lower than what is achievable with large-scale diffusers (0.7) but does not deteriorate compressor performance to unacceptable levels (current improved compressor design has a total-to-static pressure ratio of 3.6 at an adiabatic efficiency of 70 %).

For the micro-turbine Gong [12] found that loss in nozzle guide vanes is also higher (about ten times) than the loss in large NGVs due to low Reynolds number. He characterized NGV performance in terms of Re and geometry and proposed design guidelines. Philippon [17] used 3-D CFD and established typical performance levels for micro-turbine rotor and stage. The investigated micro-turbine had an efficiency of about 60% for pressure ratio of 2 to 3.

It is important to emphasize that Re effects on micro-turbomachinery performance do not render a micro-gas turbine engine not viable.

Stationary Casing effect

There is an important source of loss associated with casing drag, which is also related to low Reynolds number. Kang investigated a scaled down version of an unshrouded large impeller [18]. He reported experimentally measured polytropic efficiency for a 12 mm diameter unshrouded micro-impeller (impeller not stage) of about 73 % compared to typical values of 90-95% [13] for the large version. This suggests that casing effects may also be important for micro-impellers since passage loss is not expected to cause such deterioration in performance based on the results by Casey [16]. Gong [12] found through numerical experiments that for the initial micro impeller design shrouding the impeller improves performance by 15-20 efficiency points. Shirley [19] collected experimental data on a dynamically scaled, conventionally sized, "macro-rig" facility. An impeller shroud was tested and it was deduced, contradicting the CFD results, that shrouding is detrimental to compressor performance. It is suggested by Gong that the discrepancy in the results is related to the seal geometry used in the experiment which allowed enough leakage flow to deteriorate compressor performance. The improvement in compressor performance due to shrouding suggested by CFD results is thus regarded as one of the key design steps towards a self-sustained engine.

Non-adiabatic effect

Gong [12], upon implementing 3-D calculations with realistic boundary conditions, realized that micro-compressor performance was unexpectedly low (a pressure ratio of 1.7 and an efficiency of 29 % for an unshrouded compressor with 800 K wall temperature). Such performance levels cannot meet the design requirements of a micro-engine. Gong found that a performance-limiting factor is the non-adiabatic operation of the compressor. He suggested that the performance of a non-adiabatic compressor is similar to the performance of the same adiabatic compressor with

inlet flow preheated with the same amount of heat addition [12]. The effect of heat addition was also investigated by Isomura, Murayama, and Kawakubo at IHI [20,21]. They calculated efficiency penalty of up to 40 points at 1000 K compressor wall temperature for their micro-impeller design in accord with the results obtained by Gong. Therefore, this performance limiting mechanism is another major barrier to self-sustained engine operation. Thermal isolation for micro-turbomachinery thus becomes an important requirement for a self-sustained engine.

Turbine discharge loss

Gong [12] found that turbine discharge loss is a performance limiting mechanism for the micro-turbine. Attempts to use a diffuser to recover the kinetic energy at exit were not successful due to the low Reynolds number flow regime. Gong characterized turbine discharge loss in terms of exit Mach number. A design implication is that larger turbine exit area will lower the exit Mach number and improve turbine performance. One option is to increase turbine radius. However, a larger turbine implies higher stresses, for a given RPM, and higher levels of heat transfer to compressor. Therefore, many constraints and performance limiting mechanisms are tightly coupled and a trade-off choice must be made to improve overall system efficiency and power output. Turbine discharge loss limits turbine performance to efficiency levels of 10-15% lower than these for large turbines.

Summarizing, the physical mechanisms uniquely important to micro-turbomachinery were identified as low Reynolds number, casing drag, and heat transfer and typical performance levels of components were established. The effect of heat addition on impeller performance has been determined by Gong [12]. A research task of this thesis is to develop basic models for the remaining two dominant performance limiting mechanisms: (i) casing drag and (ii) impeller passage loss. The derived scaling laws serve as the basis for characterization of micro-turbomachinery performance and the formulation of design guidelines.

Micro-Engine System Studies:

Several researchers proposed system designs and made recommendations for system improvement. These designs, however, could not operate in a self-sustained mode. Due to the deterioration of compressor performance with heat addition, the demonstration engine designed by Protz [22] could not produce positive power with the turbomachinery and system design at the time, unless turbomachinery performance were further improved. The engine designed by Protz used the rotor to cool the turbine to the desired temperature by conduction, passing heat to the compressor. Protz concluded that cycle performance is most sensitive to compressor efficiency and pressure ratio, which underlined the need for improved turbomachinery. He also found that cycle performance increased monotonically with increasing combustor exit temperature, T_{T4}. Kerrebrock [23], on the other hand, recommended reducing T_{T4} based on cycle analysis to decrease the overall heat transfer to the compressor so as to improve system power output. In view of these observed trends there is thus a need for a thorough quantitative analysis of micro-engine system behavior and for a development of consistent system model accounting for all dominant mechanisms and constraints.

The options considered to improve system performance were the following: to thermally isolate the compressor from the turbine and either film cool the turbine or allow it to operate at higher

temperatures by using stronger material (SiC) than silicon. Evans [24] developed a simplified system model accounting for the coupling between component and system performance through heat transfer and for the secondary flow system required for turbine film cooling. The "break-even" system design proposed by Evans, however, did not account for the many important constraints (structural, as well as fluid dynamic) and assumed unrealistic levels of cooling effectiveness (based on Philippon's [17] computed results). Evans interrogated his system model to identify potential design solutions and to delineate sensitivity of system performance to design parameters. His recommendations to improve system performance were to increase turbine radius, increase combustor exit temperature, and decrease isolation shaft area.

In summary, turbine cooling by conduction to compressor and turbine film cooling were investigated but not to the extent to permit a design of a viable break-even engine. A new integrated system model and design methodology are needed to properly describe the additional requirements and constraints imposed on micro-engine system behavior by heat transfer.

1.4 CONSIDERED OPTIONS TO IMPROVE SYSTEM BEHAVIOR

A major barrier to a break-even engine is the low turbomachinery performance (specifically the micro-compressor), as described in the previous sections. To understand how to improve micro-compressor performance, the micro compressor performance must first be characterized. The link between physical understanding (characterization) and compressor geometry (design) must then be established in the form of design guidelines. Improving the design of non-adiabatic micro-compressors is one way of improving component and thus system performance. A second way is to thermally isolate the compressor to prevent heat flowing from the turbine and the other hot sections to the compressor flow. A third option is to develop an integrated system model to account for heat transfer in the engine and the heat transfer induced coupling between components. The model will enable selection of system parameters for improved performance. These options are illustrated in Figure 1.3 and described next:

1. Improvement in compressor performance for non-adiabatic operating conditions. This can be achieved by quantifying controlling parameters that characterize micro-compressor performance and by developing design guidelines to optimize non-adiabatic performance.

2. Reduction of heat transfer to compressor by a thermal isolation shaft between compressor and turbine and/or

   (a) film cooling the turbine – research aimed at proposing cooling schemes and improving micro turbine film cooling effectiveness is required

   (b) use of SiC in the turbine – research aimed at incorporating SiC into the micro turbine is required

3. Search the micro-engine system design space (pressure ratio, turbine inlet temperature, etc) with an integrated system model for a region offering self-sustained engine operation with mitigated requirements on component performance and technology levels

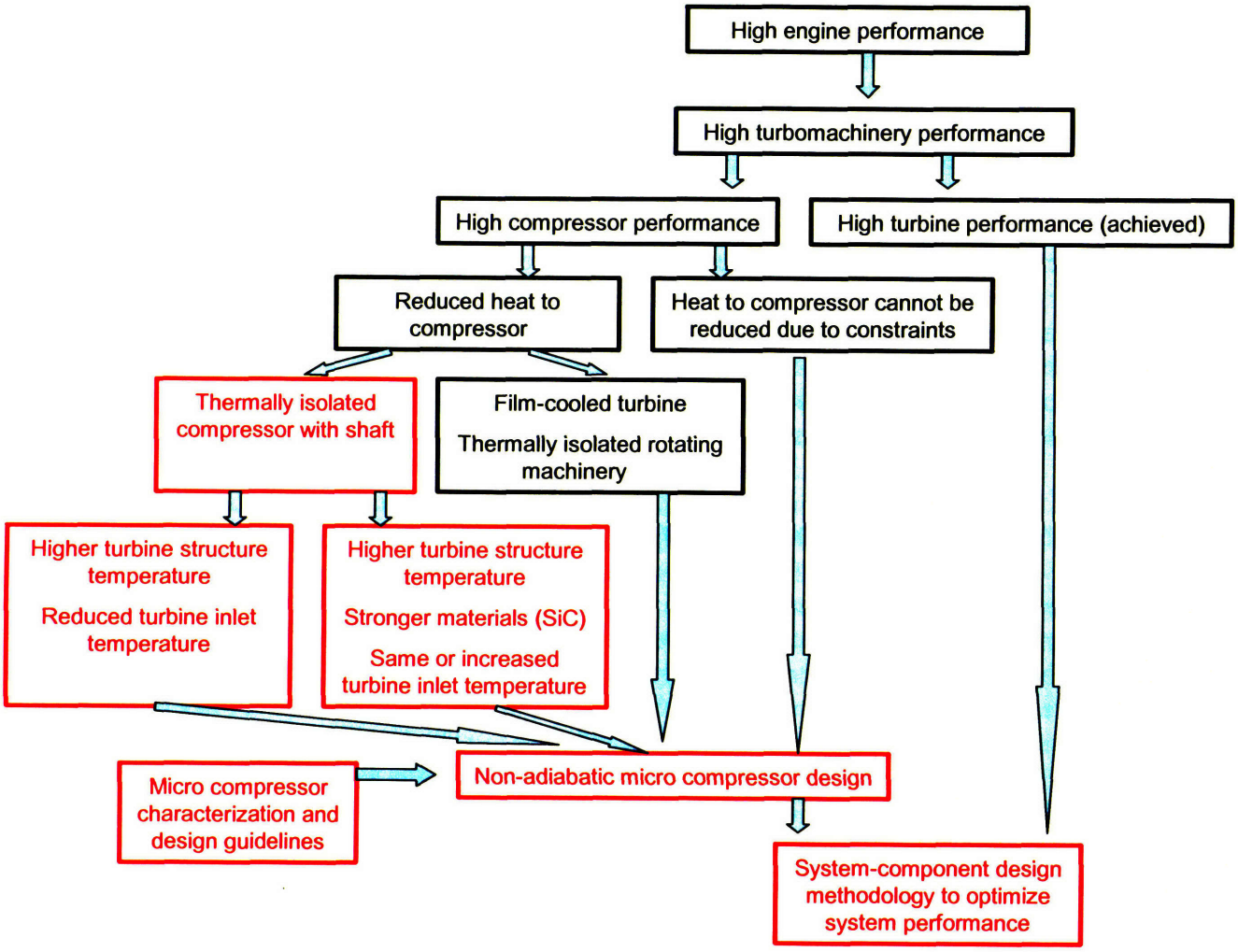

Figure 1.3 Options considered to improve system performance (options pursued are in red). Arrows indicate requirements.

1.5 RESEARCH OBJECTIVES

Both options 2 (a) and 2 (b) from the previous section rely on the development of new advanced technologies. The research proposed in this thesis is mainly aimed at options 1 and 3 and it attempts to provide answers to the micro-engine problem in case the technologies from option 2 are not available or only partially available. The requirements on the technology levels (etch depth , SiC deposition, turbine disk film cooling) and turbomachinery performance levels needed to enable a self-sustained engine will be established. Any advances in option 2 (b) will also be considered.

The specific research objectives of this thesis are:

1. To establish general design guidelines for micro-compressor impellers

This requires first identifying and quantifying sources of limitations in non-adiabatic micro-impellers. Establishing governing scaling laws for the dominant performance limiting mechanisms followed by characterizing impeller performance is needed. Incorporating the effects of the dominant mechanisms into a mean-line design procedure will enable formulation of micro-impeller design guidelines.

2. To set minimum requirements on technology levels and to enable the selection of cycle parameters for a self-sustained micro-engine

This requires first developing a tool to perform micro-engine cycle analysis on a rational basis. An integrated system model will be synthesized to account for additional system coupling through heat transfer and to enable the selection of cycle parameters. Mapping of engine design space will follow to assess the effect of each advanced technology level on system performance and to establish minimum requirements for a self-sustained engine.

1.6 SUMMARY OF KEY RESULTS AND CONTRIBUTIONS

1) A mean-line analysis tool for micro-impellers is developed, based on models for the dominant performance limiting mechanisms and on impeller performance characterization. This tool is used to investigate the effect of impeller geometry on impeller performance and to provide guidance to micro-impeller geometry selection. The meanline analysis tool enabled the following contribution:

   A key difference between the design of conventional and micro-impellers is identified. This is the fact that optimal micro-impeller design changes with impeller wall temperature. Design guidelines are formulated.

   Two competing mechanisms govern non-adiabatic micro-impeller design: levels of aerodynamic loss and heat addition. At high impeller wall temperatures the optimal impeller geometry changes in such a way as to cause the following changes: (i) aerodynamic loss increases relative to its value for an impeller designed for adiabatic operation and (ii) the detrimental thermodynamic effect of heat addition on impeller performance decreases relative to its level for an impeller designed for adiabatic condition and operated at the given high wall temperature. The net effect is beneficial for impeller efficiency. As impeller wall temperature increases the optimal inlet angle, back sweep angle, solidity, and radial size leading to peak efficiency operation all decrease from their values at adiabatic conditions. If a micro-impeller is optimized for adiabatic conditions but is operated at high wall temperature an additional penalty of 10-15 points on isentropic efficiency can be incurred.

2) A system model and design methodology are developed and formalized. Cycle analysis based on the assumption for constant components performance is ineffective for micro-

engine selection. Micro-component performance changes for each choice of system parameters as a result of heat transfer. The system model accounts for the heat transfer induced coupling between system and components. Component performance is thus adjusted for each set of cycle parameters. Structural, fluid dynamic, and thermodynamic constraints are accounted for. The system model and methodology enable the generation of system design space maps and the selection of system design parameters. The integrated system model enabled the following contributions:

Key differences in the selection of thermodynamic cycle and size for micro and large engines are identified. These differences consist of the following: (i) an optimal turbine inlet temperature for micro-engine cycle exists, in contrast to conventional engines where the largest temperature consistent with material properties is used. (ii) system efficiency improves with increasing turbomachinery size for micro-engines.

The selection of turbine inlet temperature depends on turbomachinery technology level and size and heat transfer levels. Relevant non-dimensional parameters are identified and described. The existence of optimal turbine inlet temperature is a consequence of two competing effects as turbine inlet temperature increases: (i) improving cycle output and efficiency (ii) increasing heat transfer to compressor, degradation of compressor and thus cycle performance.

Effect of turbomachinery size on system performance is established. System performance changes are governed by the scaling of heat transfer and parasitic power loss with size.

Minimum requirements on performance and technology levels for a self-sustained engine are established. A 60% increase in turbomachinery size, or turbine disk reinforcement with 30% SiC or film cooling for nearly adiabatic turbine disk operation and an appropriate thermal isolation shaft (with thermal resistance equivalent to the one of a column shaft with cross sectional area of 1% of compressor disk area, length of 500 microns, made of silicon) are required for self-sustained engine operation.

The impact of each advanced technology on system performance is investigated. A candidate design for a self-sustained engine is selected based on projection for technology capabilities, probability for success, and development technical risk.

A preliminary design of a self-sustained micro-engine system producing 23 Watts of net shaft power at efficiency of 1.6% is proposed.

1.7 ORGANIZATION OF THESIS

This chapter described the micro-engine concept, the challenges related to micro-engine system design, and delineated the contributions of the thesis.

Chapter 2 presents the foundations for micro-compressor technology. The focus is on the characterization of micro-impellers in terms of non-dimensional parameters and groups.

Dominant performance limiting mechanisms in micro-impellers are quantified, and models are developed to delineate the scaling laws for the effects.

Chapter 3 presents a micro-compressor analysis and preliminary design tool based on the impeller passage loss model developed in Chapter 2 and the non-adiabatic impeller performance model by Gong [12]. This tool is used to formulate design guidelines for non-adiabatic micro-impellers. It establishes a link between physical understanding of micro-impellers and geometric design. Key differences are identified between the design of conventional and micro-impellers.

Chapter 4 presents a detailed description of a new integrated system model developed to enable selection of cycle parameters for micro-engine systems. This model forms the backbone of a fundamentally new design methodology for micro-engines.

Chapter 5 provides insight into system behavior and also details the results of an engine design study. The integrated system design methodology developed in Chapter 4 is used to generate system design space maps and to enable and guide the selection of a self-sustained micro engine. The results from the study are used to establish minimum requirements on component performance and technology levels for a "break-even" engine. Key differences in the selection of thermodynamic cycles for micro and conventional systems are identified. Preliminary design of a "break-even" engine is proposed.

Chapter Six summarizes the conclusions in the thesis. Areas of focus for future research are suggested.

CHAPTER 2

2 PERFORMANCE CHARACTERIZATION OF MICRO-COMPRESSOR IMPELLERS

2.1 INTRODUCTION

The micro-impeller is a critical component of the engine system. It determines the overall system pressure ratio and mass flow. The efficiency of the micro-compressor determines to a large extent whether the micro-engine produces net power. The work presented in this chapter lays the scientific foundation for micro-compressor technology. It establishes the relative importance of the performance limiting fluid phenomena and determines the governing scaling laws. Based on analytical models and 3-D CFD solutions impeller performance is characterized in terms of non-dimensional parameters.

This chapter begins with delineation of the approach used in the characterization of micro-impellers, followed by a description of the numerical tools used. Results from a numerical study are presented next followed by development of simplified models for the important effects. The chapter concludes with formulating the micro-impeller characterization.

The ideas presented in this chapter are further developed in Chapter 3 to provide design guidelines for non-adiabatic micro-impellers.

2.2 APPROACH

A set of numerical experiments are implemented to quantify performance-limiting mechanisms in micro-impellers. Then analytical models are developed to describe the effect of these mechanisms on impeller performance in terms of controlling non-dimensional parameters.

Steady, Reynolds-averaged, Navier-Stokes simulations were carried out with FLUENT CFD code [25] to study micro-impellers. One of the MIT micro-impeller designs is selected as a baseline geometry and boundary conditions are varied to isolate effects of different mechanisms. The baseline design has 20 impeller blades, 8mm rotor diameter with blades running from 2 to 4 mm radius (impeller diameter ratio = 2). Blade span varies linearly[1] from 400 microns at inlet to 200 microns at exit (made possible by a pioneering micro-fabrication technology developed at the University of Maryland [26,27]). Tip clearance gap is 20 microns, 5 to 10 % of blade height depending on location. Impeller blade inlet angle is 55 degrees and exit back-sweep angle is 45 degrees. The impeller tip speed is 500 m/s, rotating at 1.2 million RPM (see also Table 3.1 in Chapter 3).

[1] For the self-sustained engine design turbomachinery blade span is kept constant. Variable span technology may become available for the next generation engine

The effect of heat transfer was studied by comparing an adiabatic wall case to cases with specified wall temperature. The casing effects associated with casing drag and tip clearance flow were studied by shrouding the impeller and comparing it to an un-shrouded one with the same geometry. The effect of the flow turning through a right angle in the inlet from axial to radial direction (a consequence of the two dimensional micro-fabrication constraints imposed) is studied by prescribing inlet condition of flow already in the plane of the impeller which does not have to make a turn. Finally, the loss associated with a shrouded, adiabatic impeller without any turn at inlet is attributed to blade passage boundary layers as will be shown later.

2.3 NUMERICAL TOOLS

The Computational Fluid Dynamics code selected for this investigation is FLUENT [25]. It is a commercial code capable of using structured and unstructured grids for numerous applications. It offers a selection of solvers (implicit, explicit), boundary and initial conditions, fluid specification (chemical composition), turbulence models. For this work unstructured grids were prepared using GAMBIT [28] and exported to FLUENT. The baseline computational grid has 237,379 nodes, which is sufficient to obtain grid independent values for the figures of merit and to provide enough details for flow analysis. The steady coupled explicit solver was used to obtain solution for the flow-field within the impeller passage. Since the Reynolds number within the impeller passage based on passage exit blade span and passage through-flow velocity at design condition is ~ 4000, the flow in the impeller is taken to be turbulent and the κ–ε turbulence model was selected. The enhanced wall treatment option was used to solve for the flow near walls. This option combines a two-layer model with wall functions. If the near-wall grid were not fine enough to resolve the viscous sub-layer, then the enhanced wall treatment model would use wall functions. Three levels of multi-grid were used and the code was run in parallel to reduce wall-clock time for a converged solution. Results from the selected CFD code compare favorably to available experimental data [12,29].

2.4 RESULTS

The results for the baseline impeller investigation are summarized in Fig 2.1. This figure indicates the relative importance of the performance limiting mechanisms for the investigated micro-impeller. The highest penalty to impeller performance is caused by heat addition, followed by casing drag and passage boundary layer loss.

The dominant mechanisms have been quantified with the following set of computational cases:

1. 900 K wall temperature, unshrouded impeller with right-angle turn at inlet
2. 600 K wall temperature, unshrouded impeller with right-angle turn at inlet
3. adiabatic wall, unshrouded impeller with right-angle turn at inlet
4. shrouded, adiabatic impeller with right-angle turn at inlet
5. no turn at inlet, shrouded, adiabatic impeller

Comparing case (1) to (3) the penalty in impeller efficiency associated with heat addition is up to 25 points. Heat addition to impeller flow, therefore, has the largest impact on impeller isentropic

efficiency. For case (1) the heat transfer to the impeller flow is comparable to the work input to the impeller rotor.

By comparing case (3) to (4), another loss source is quantified, associated with casing effects including casing drag, and tip clearance flow, of which casing drag dominates. Shrouding the impeller leads to 17 points improvement in efficiency of which 13 points are directly linked to casing drag. The remaining 4 points may be attributed to tip clearance flow. This is in accord with the estimates by Kang et al. at Stanford for a 10% tip-clearance-to blade height ratio [18].

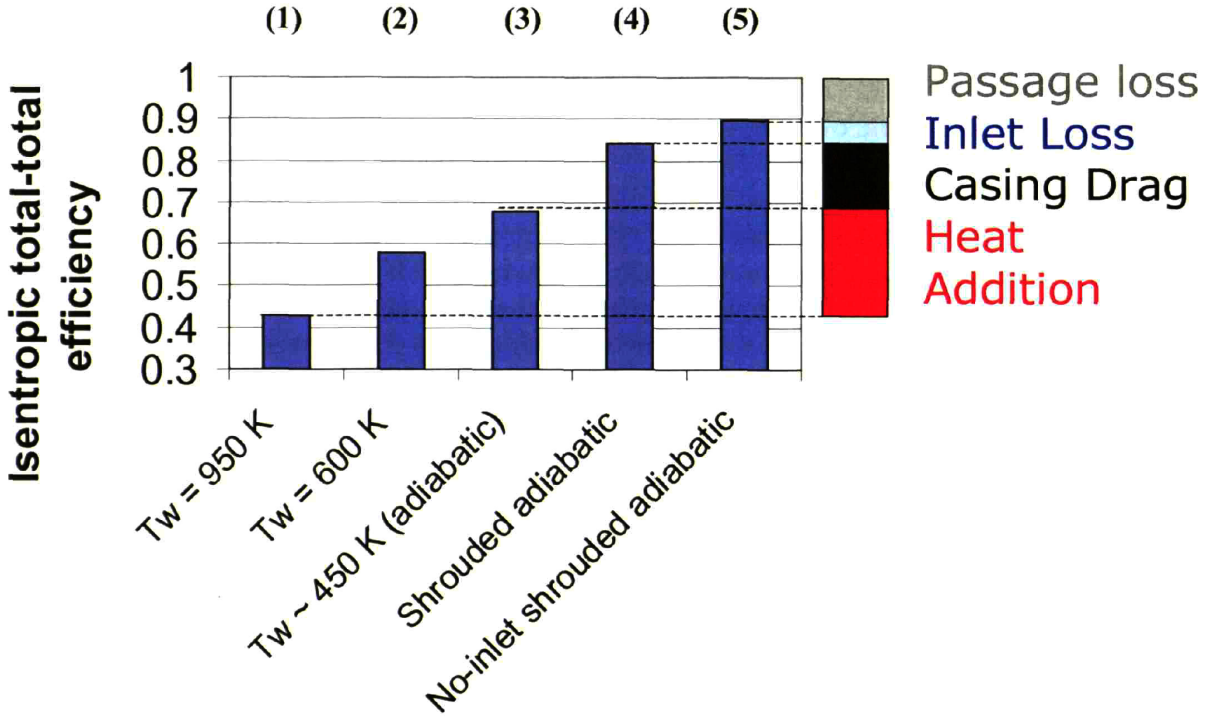

Figure 2.1 Peak isentropic impeller efficiency for cases of interest. Quantification of performance limiting mechanisms for the micro impeller.

By comparing case (4) to (5) the effect of flow turning in the inlet (leading to inlet flow separation, loss due to mismatched velocity triangles at impeller inlet, and downstream mixing loss) is isolated. The loss associated with the flow turning in the right angle inlet is about 5 efficiency points.

By comparing impeller performance in case (5) to an ideal 100% efficient impeller the passage loss is estimated to be about 10 efficiency points.

The results obtained in this study are in agreement with the available experimental and computational results discussed in Chapter 1.

2.5 MICRO-IMPELLER MODELING

2.5.1 HEAT ADDITION

A model for the effect of heat addition on impeller performance, developed by Gong [12], will be briefly described here for completeness. The main idea is that impeller with heat addition has similar performance to an adiabatic impeller whose inlet flow is preheated with the same amount of heat addition. The effect is explained by the physical fact that compression of air to a certain pressure at higher temperature requires more work. The results from the model are compared to CFD calculations for different impellers and heat addition levels and there is good agreement [12]. The effect of heat transfer on impeller performance is governed by the heat addition parameter, q*, defined as the total amount of heat transferred to impeller flow divided by the inlet flow stagnation enthalpy. Gong [12] described the effect of heat addition on impeller efficiency as in equation 2.1. Based on the same idea Sirakov [12] developed an expression for pressure ratio (Eq. 2.2) and Protz [12] developed an expression for mass flow (Eq.2.3).

$$\eta = \eta_{adb} \frac{1}{1+q^*} \tag{2.1}$$

$$\pi = \left(\left(\frac{1}{1+q^*} \right) \left[\pi_{adb}^{\frac{\gamma-1}{\gamma}} - 1 \right] + 1 \right)^{\frac{\gamma}{\gamma-1}} \tag{2.2}$$

$$\dot{m} = \dot{m}_{adb} \frac{1}{1+q^*} \tag{2.3}$$

According to the model, impeller non-adiabatic performance can be estimated from knowledge of impeller adiabatic performance, heat addition parameter, and equations 2.1-2.3. For example, if the impeller adiabatic efficiency is known, Eq 2.1 provides an estimate for impeller isentropic efficiency for non-adiabatic operation.

The physical interpretation of the equations is as follows: If the air to impeller inlet were preheated, for given work input per unit mass flow the achieved pressure ratio is lower compared to a case without preheating (hence the pressure ratio penalty reflected in Eq. 2.2). Isentropic efficiency is lower for the preheated case consistent with the lower pressure ratio for the same given work input per unit mass flow (Eq. 2.1). Mass flow is also affected simply due to the change in density of the flow entering the impeller after preheating (Eq. 2.3).

As mentioned earlier, the effect of heat addition on impeller performance can be described with the non-dimensional parameter q* and Figure 2.2 presents the effect of heat addition on impeller performance. The thick black line represents the effect of heat addition parameter on isentropic efficiency and mass flow. The other lines represent the effect of heat addition parameter on pressure ratio for different adiabatic pressure ratios. The results of Figure 2.2 show that impeller performance is sensitive to the value of q*.

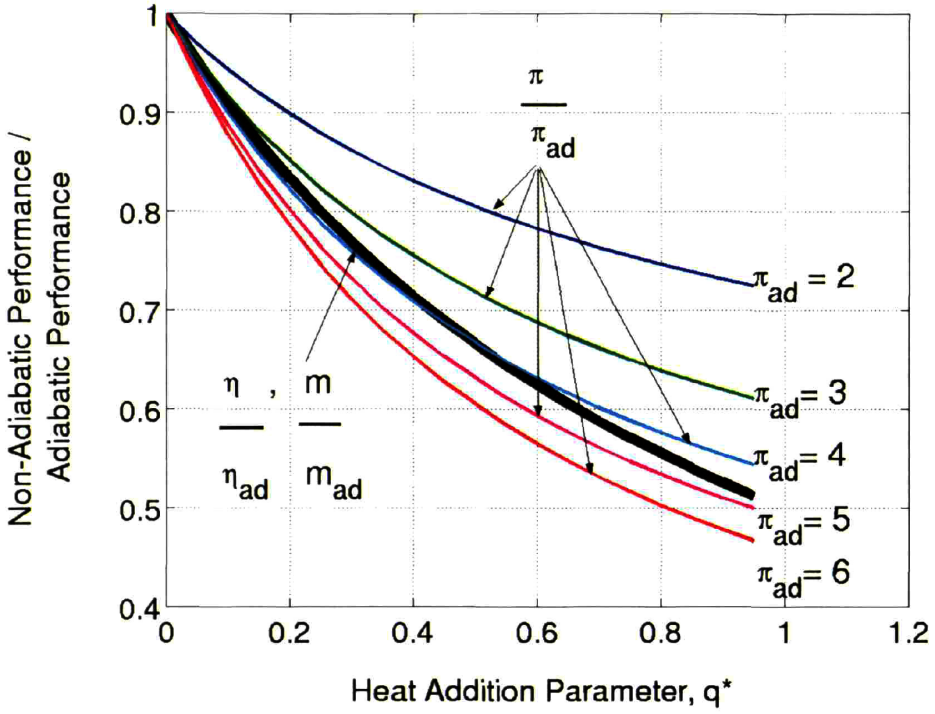

Figure 2.2 Effect of heat addition on micro-impeller performance.

In the model the non-adiabatic compression process is conceptually divided into preheating first followed by adiabatic compression. The results so obtained are in agreement with those from CFD. Therefore, the effect of heat addition is mainly thermodynamic and can be treated separately from the aerodynamic effects. Heat parameter, q*, will depend on the boundary conditions imposed on the impeller by the rest of the system and a designer must take this into account.

The added heat is proportional to the wetted area in the impeller and to the temperature difference between the hot sections and the compressor flow while the inlet enthalpy is proportional to impeller mass flow. To decrease the detrimental effect of heat addition on impeller performance a decrease in q* is required. This is the topic of Chapter 3.

2.5.2 CASING DRAG

Unshrouded impellers suffer additional performance penalty due to casing drag. To counteract the effect of casing drag on the flow, additional power must be supplied to the impeller. To estimate this power, the flow in the casing region is modeled as flow in a enclosed rotating disk [30]. The flow within the micro-impeller can be viewed in the following manner: The flow within the blade passage is approximated to be in solid body rotation with a characteristic angular velocity. Because the blades in micro-impellers have back-sweep and experience slip velocity at exit, the characteristic angular velocity of this flow is obtained by correcting the actual rotor angular velocity for these two effects. The correction is performed at the exit radius. Next, the flow in the casing region (between the casing and the plane of the blade tips) is approximated as flow in an enclosed rotating disc with superposed radial outflow. For the

investigated impellers the regime is turbulent with small clearance gap. To obtain an estimate for the torque on the disc (or the casing) an expression developed by Dorfman for this regime is used [31]. When the casing torque is multiplied by the angular velocity of the impeller an estimate for the lost power due to casing drag is obtained.

The rotational Reynolds number defined in Eq. 2.4, is based on rotor exit radius and gas properties at the exit radius. The tip clearance ratio G given in Eq. 2.5 is the ratio of tip clearance to rotor radius. From Dorfman's expression (based on solving the integral-momentum boundary layer equations [31]) it follows that the moment coefficient of the rotor as given in Eq. 2.6 is a function of Reynolds number and clearance ratio (geometry). To obtain power the torque M in Eq. 2.6 is multiplied by angular velocity. This consumed (lost) power given in Eq. 2.7 scales with angular velocity to the third power and exit radius to the fifth power.

$$\mathrm{Re}_{rot} = \frac{\rho \Omega r_{exit}^2}{\mu} \tag{2.4}$$

$$G = \frac{t}{r_{exit}} \tag{2.5}$$

$$C_m = \frac{M}{\rho \Omega^2 r_{exit}^5} \sim \mathrm{Re}_{rot}^{-\frac{1}{4}} G^{-\frac{1}{4}} \tag{2.6}$$

$$\frac{\dot{W}_{lost}}{\rho \Omega^3 r_{exit}^5} \sim \mathrm{Re}_{rot}^{-\frac{1}{4}} G^{-\frac{1}{4}} \tag{2.7}$$

From Eq 2.7, the contributions to the lost power from near the outer radius will be larger than near the inlet radius. This justifies the correction of angular velocity at the exit radius, and the use of gas properties in the model based on exit radius.

The estimate from the model is compared to CFD results in Fig. 2.3. Figure 2.3 presents the dissipated work for the baseline unshrouded impeller for different rotating speeds and operating conditions. The inputs to the model are extracted from the CFD solutions, lost power is estimated with the model, and compared to the lost power calculated from casing torque and rotor angular velocity. The torque on the casing is directly related to the torque on the flow at the plane of the blade tips.

At design condition (125 Krad/s) the power supplied to the compressor is about 100 Watts and it can be seen in Fig. 2.3 that the casing drag consumes around 10-15% of it. This can be eliminated by shrouding the impeller. Preliminary estimates suggest that the friction between the rotating shroud and stationary casing consumes only about a third of the benefit due to shrouding and the micro-compressor designer should take this into account.

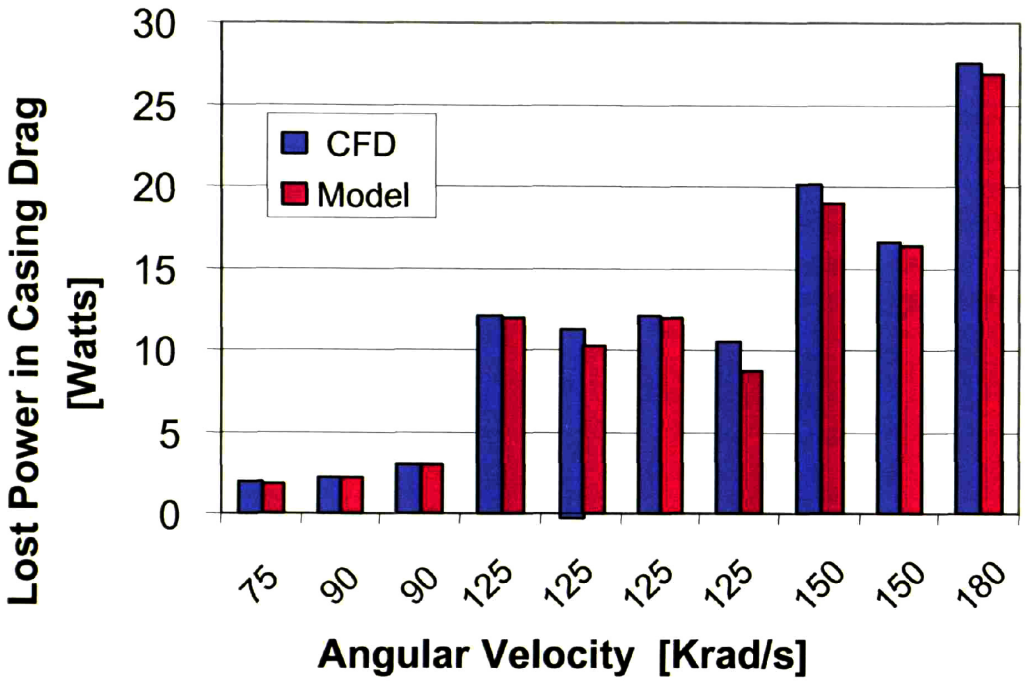

Figure 2.3 Lost power due to casing drag plotted dimensionally for clarity for different impeller speeds and geometries.

The performance penalty from casing drag is related to low Reynolds number effects. An important observation can be made in Fig. 2.4 presenting entropy generation in the impeller passage. The most intense entropy production in the passage occurs in a thin layer between the casing and the blade tip plane at the outer radius of the impeller as indicated by the red region. This supports the assumptions and conclusions of the model.

Another important observation is that viscous forces participate in driving the flow through the blade tip clearance unlike the situation for large machines where the tip clearance flow is mainly pressure driven. The importance of the viscous effects in the tip clearance region is confirmed in Fig. 2.5, which shows a velocity profile in the tip gap resembling Couette flow. This importance of viscous forces in driving the tip flow can be explained in the following manner next.

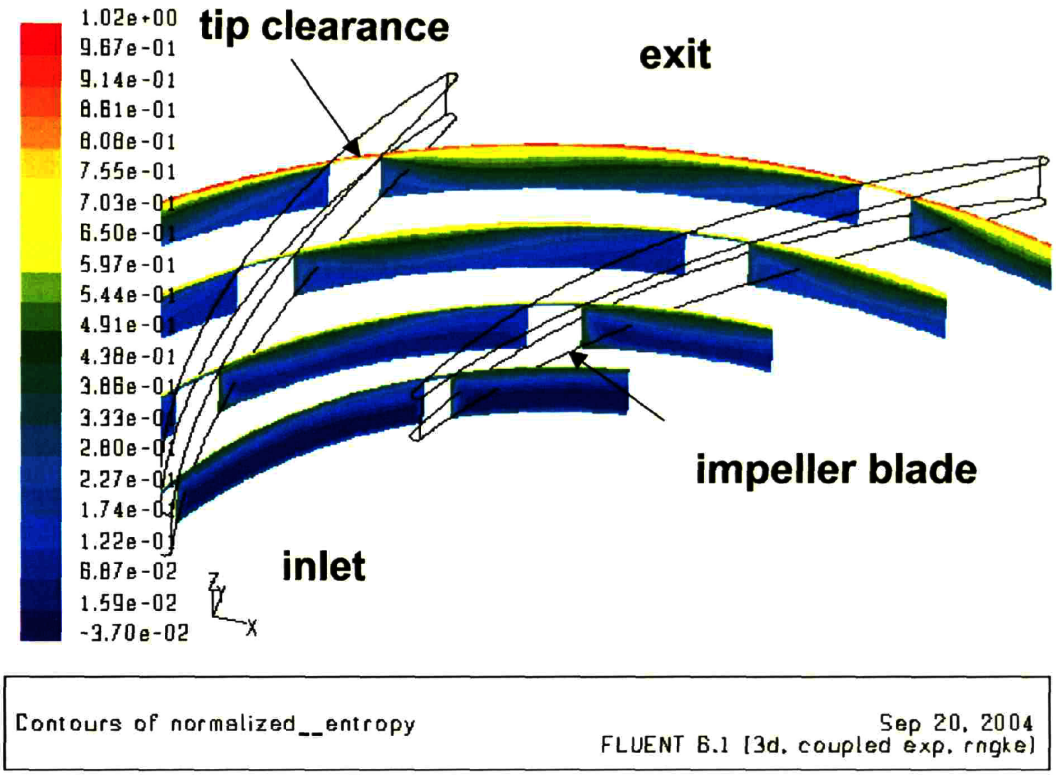

Figure 2.4 Normalized entropy production [$T_0(s_{local}-s_{avr\_inlet})/(0.5V_{tip}^2)$] contours in a micro-impeller passage showing regions of intense entropy increase.

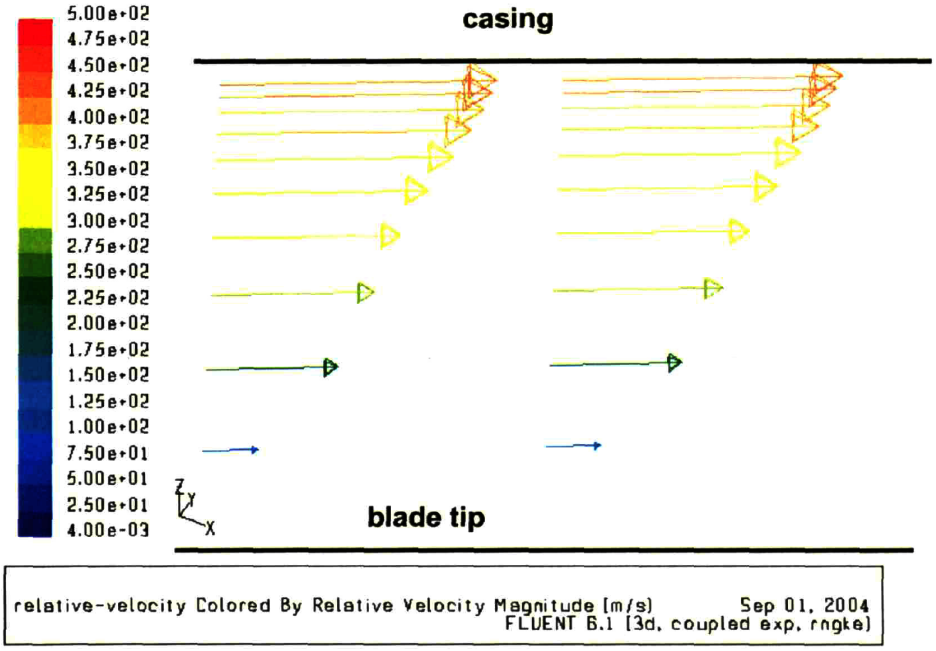

Figure 2.5 Relative velocity profile in tip clearance gap of a micro-impeller.

The tip clearance gap is on the order of 20 microns. The blade thickness at tip is between 100 and 200 microns. Therefore, the tip flow passes through a narrow channel to exit the tip gap. For conditions representative for micro-impellers the tip flow locally within the clearance gap would always be laminar based on hydraulic diameter.

If only pressure forces drive the tip flow, the velocity inside the tip gap can be approximated in the following manner using simple Poiseuille flow expression (Eq. 2.8).

$$V_P = \frac{1}{12}\frac{t^2}{\mu}\frac{\Delta P}{L} \tag{2.8}$$

where V_P is the tip flow velocity, t is tip clearance gap, L is blade thickness or flow path length in the tip clearance gap, μ is viscosity and ΔP is the driving pressure difference.

If only viscous forces drive the flow the average velocity in the tip gap can be expressed simply as:

$$V_{VIS} = \frac{V_{tip}}{2} = \frac{\omega R}{2} \tag{2.9}$$

assuming a Couette flow profile, as suggested by the computed profile in Fig 2.5, where V_{VIS} is the tip flow velocity, V_{tip} is blade tip speed, ω is rotor angular velocity, and R is radius.

To assess the relative importance of the two driving mechanisms we examine the ratio of the two velocities:

$$\frac{V_P}{V_{VIS}} = \frac{1}{12}\frac{t^2}{\mu}\frac{\Delta P}{L}\frac{2}{\omega R} \tag{2.10}$$

The tip clearance gap t is an order of magnitude smaller than the blade thickness L. The ratio represents the aspect ratio of the tip gap channel. The pressure difference across the blade can be approximately related to blade loading and to the Coriolis force in the passage as shown in equations 2.11-2.13. The relative velocity in the impeller passage w_r is proportional to the rotating velocity of the impeller (Eq 2.12). The circumferential direction or distance is denoted by s:

$$\frac{\partial p_{reduced}}{\partial s} = -2\rho\omega w_r \tag{2.11}$$

$$w_r \sim \omega r \tag{2.12}$$

$$\Delta P \approx 2\rho\omega^2 sR \tag{2.13}$$

Therefore, the ratio becomes:

$$\frac{V_P}{V_{VIS}} \sim \frac{2}{12}\frac{t^2}{\mu}\frac{\Delta P}{L}\frac{1}{\omega R} \sim \frac{2}{12}\frac{t^2}{\mu}\frac{2\rho\omega^2 sR}{L\omega R} \sim \frac{1}{3}\frac{\rho\omega R t}{\mu}\frac{s}{R}\frac{t}{L} = \frac{\mathrm{Re}_{Vtip,t}}{3}\frac{t}{L}\frac{1}{\sigma} \qquad (2.14)$$

or

$$\frac{V_{VIS}}{V_P} \sim \left(\frac{\sigma}{\mathrm{Re}}\right)\left(\frac{L}{t}\right) \qquad (2.15)$$

where Re is Reynolds number based on impeller tip speed and tip clearance gap and σ is impeller solidity. When the Reynolds number is high, the pressure force will drive the tip flow and the effect of viscous drag would be small. As Reynolds number decreases and becomes relatively low (~300), as is the case for the micro-impeller, the importance of the viscous forces increases and the pressure difference becomes less effective in driving the tip flow (V_{VIS}/V_p >1). If we take this argument to extreme (very low Re) the tip clearance gap would act like a viscous seal to dissipate the pressure difference and prevent pressure driven flow. The tip flow then would be driven by the casing drag.

2.5.3 IMPELLER PASSAGE BOUNDARY LAYER LOSS

The next mechanism governing impeller performance is passage boundary layer loss. The loss in the impeller passage (for shrouded impellers) is predominantly boundary layer dissipation. Intuitively, one might link flow separation to large mixing losses downstream of the trailing edges and such thinking led to the initial MIT designs with high back-sweep angle (70 degrees) and long passages to control diffusion. These designs resulted in impellers with low efficiency (~30%). The viscous dissipation was increased due to the increased passage length. Work input to the flow was decreased due to the high back-sweep. The mass flow was decreased due to the reduced flow exit area. However, the mixing loss behind the rotor is negligible (based on CFD). The reason is the high swirl at exit (absolute tangential velocity divided by radial velocity) and Cumpsty [32] explains this point in the following manner: in the absolute frame at rotor exit the wake fluid and the mainstream fluid have similar large swirl velocity components and very small radial velocity components. The mixing loss is caused by the difference in the radial components. Since they are very small, the mixing loss is negligible. It is difficult to avoid separation in impellers (most impellers have very high effective exit-to-inlet area ratios both due to geometry and significant density changes) but fortunately its impact on rotor efficiency is not dramatic for impellers with strong exit swirl as explained above. The price for having large swirl at impeller exit is paid for by the diffuser performance but this is the case for most radial compressors [33].

To estimate impeller passage loss it is useful to model impeller passages as channels of given hydraulic diameter. Simple channel flow ideas like Darcy friction factor [34] provide loss estimates (Eq 2.16). The definition of Darcy friction factor can be manipulated to provide a link between Darcy friction factor (Reynolds number), lost work, geometry, and operating conditions:

$$f_{Darcy} = \frac{\Delta P D_h}{\frac{1}{2}\rho V^2 L} = \left(\frac{V}{V}\right)\frac{\Delta P D_h}{\frac{1}{2}\rho V^2 L} = \frac{8 W_{lost} A_{in}}{m V^2 A_{wet}} \tag{2.16}$$

where ΔP is pressure loss, D_h is hydraulic diameter, V is characteristic relative velocity, L is passage length, ρ is density, W is lost work, m is mass flow, and A is area.

Eight different impeller designs were investigated to assess impeller passage loss. The Reynolds number in the impellers is sufficiently high (3000-5000) so that the flow is turbulent. The geometric parameters that were varied from design to design were blade back-sweep angle (25, 45 and 70 degrees), inlet angle (45, 55, and 65 degrees) and blade inlet–to-exit span ratio (1:1, 2:1, and 3.3:1). The results are presented in Fig. 2.6 in which impeller lost work is given as function of impeller inlet flow kinetic energy.

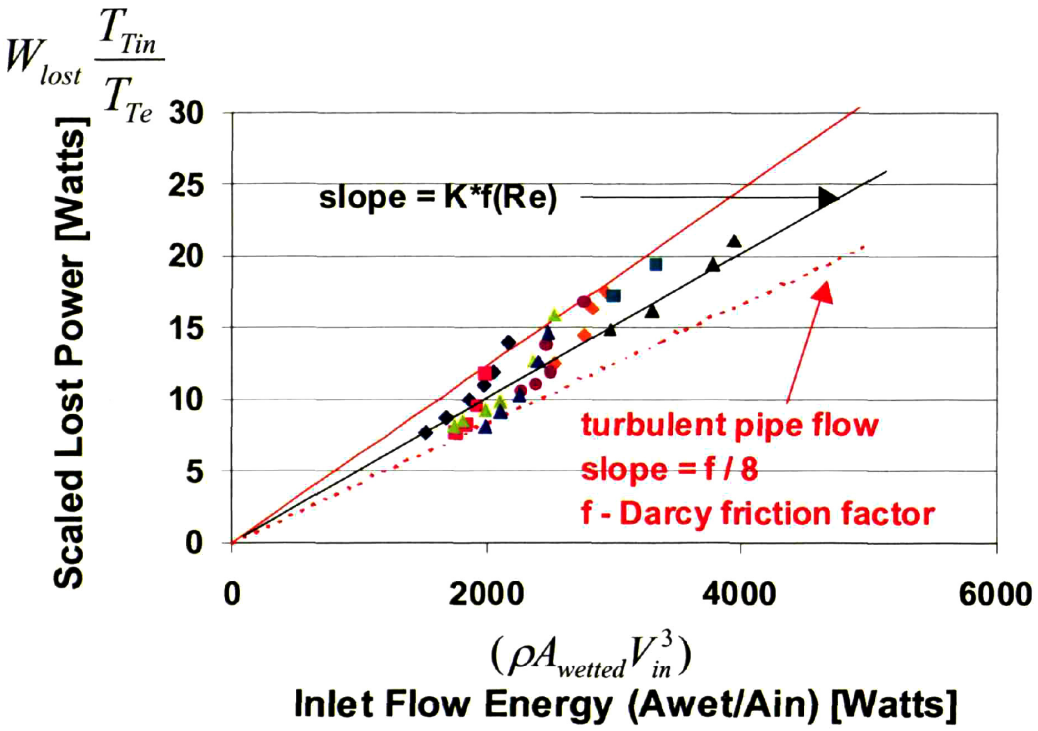

Figure 2.6 Impeller passage loss as a function of inlet flow kinetic energy and passage Reynolds number. Points are calculated from CFD. Red lines are estimated from friction factor.

The lost power in the eight impellers is calculated from CFD solutions. Power input is calculated from torque and rotor angular velocity. Efficiency is calculated from impeller total pressure ratio, mass flow, and power input. The lost power is obtained from efficiency and power input. The lost impeller power for each case is scaled down with the impeller temperature ratio for comparison purpose. This will be explained in the next paragraph. The lost power per unit wetted area is calculated from geometry. At the same time, the inlet flow kinetic energy per unit inlet area is calculated from inlet velocity and density. The ratio of the two is proportional to Darcy friction factor, which is also the slope of the lines on Fig 2.6. Dissipation coefficient can also be used instead of friction factor.

It can be inferred from Fig. 2.6 that passage loss in all eight impellers when appropriately scaled and non-dimensionalized (lost power as fraction of inlet flow energy, Eq. 2.19) is only a function of Darcy friction factor (Reynolds number). The estimate of friction factor assumes smooth walls. Boundary layers are relatively thick due to the low Re (4000) and typical wall roughness on the order of several microns has little effect on the flow [30]. The actual lost power scales with friction factor, wetted area, inlet velocity cubed and impeller temperature ratio. The dependence on inlet velocity cubed is not surprising if one is familiar with boundary layer dissipation coefficient [35]. The dependence on impeller temperature ratio (or work input) is explained in a subsequent section.

Both, friction factor and dissipation coefficient are functions of Reynolds number and the parametric dependence of lost power can be expressed in the following manner using the result from Eqn. 2.16:

$$\mathrm{Re} = \frac{\rho V_{in\_rel} s_{exit}}{\mu} \tag{2.17}$$

$$C_d \sim \mathrm{Re}_\theta^{-\frac{1}{6}} \tag{2.18}$$

$$\frac{\frac{\dot{W}_{lost}}{A_{wet}}}{\rho_{in} V_{in\_rel}^{3}} \left(\frac{T_{Tin}}{T_{Te}}\right) \sim C_d \sim \mathrm{Re}^{-\frac{1}{6}} \sim \frac{f}{8} \tag{2.19}$$

The friction factor f has been estimated using a Reynolds number based on hydraulic diameter or exit span (s_{exit}), rotor passage inlet velocity, and flow properties at impeller exit as shown in Eq. 2.17. For dissipation coefficient C_d, Reynolds number (Re_θ is based on boundary layer momentum thickness (Eq. 2.18). Friction factor (slope of lines on Fig. 2.6) is calculated for the highest and lowest Reynolds numbers for the eight impellers at different conditions and the two red lines bound all data points. This demonstrates the utility of the above expressions for impeller lost power estimation due to passage loss. It can, therefore, be deduced that shrouded impeller passage loss is predominantly generated in the boundary layers and can be estimated with a simple channel flow model.

The scaling of impeller lost power due to boundary layer dissipation with the amount of impeller work input (related to peripheral speed and temperature ratio) can be explained with the help of Fig 2.7. Figure 2.7 is a T-s diagram for compression processes. It shows that the lost work that would result from a flow process through a stationary channel before compression ($W_{lost\_channel}$) is amplified if the flow is subsequently isentropically compressed. The actual lost work in the impeller compression process ($W_{lost\_imp\_channel}$) depends on the level of work lost before compression and the work input to the flow (the temperature ratio).

To compare boundary layer loss for different impellers and levels of work input it is necessary to scale the actual impeller lost power with the impeller temperature ratio to obtain the "equivalent" stationary channel lost work. For a micro impeller it was shown that loss scales as velocity cubed. Therefore, the highest losses will be generated near the impeller inlet where the relative

velocity is the highest. At the same time, most of the compression happens near impeller exit, where the rotational speed is the highest. Conceptually, the flow processes within the impeller channel can be divided into loss generation first followed by isentropic compression. Assuming isentropic compression, the lost power, as shown in Fig. 2.7, due to compression to a given pressure ratio at higher entropy (from E to D as opposed to from A to B), after the boundary layer loss is generated in the channel, is ΔsTe. If the impeller passage were stationary (no compression and work input), the lost work in the channel boundary layers would simply be ΔsTin (A to E as opposed to A to C). The loss process, however, is the same for both situations. Therefore, the effect of entropy increase before compression on impeller lost power scales with compressor exit temperature.

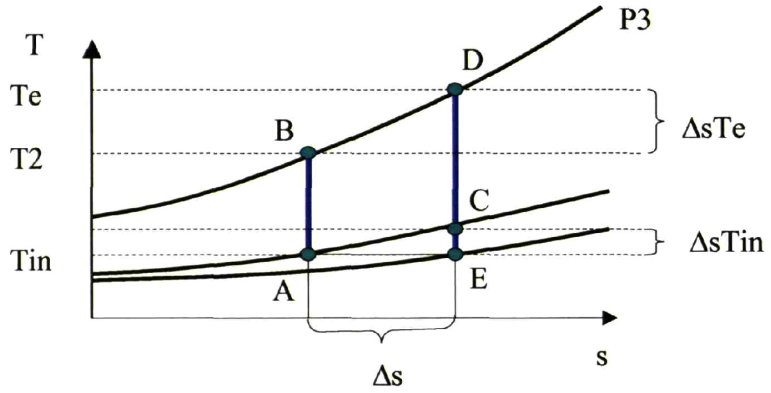

$$W_{lost\_channel} = W_{lost\_imp\_channel} \frac{T_{in}}{T_e}$$

Figure 2.7 Amplification of channel lost work due to viscous dissipation from stationary to rotating passages depicted on a T-s diagram.

The higher the impeller rotating speed, the larger the impeller exit to inlet temperature ratio becomes and, therefore, the higher the actual lost power becomes for the same initial loss process before compression. In the above description it is assumed that the effect of rotation on boundary layer behavior is small because Rossby number at inlet where most of the loss occurs is higher than one. At the impeller inlet the relative velocity is the highest while the rotation speed is the lowest. Another way of stating this is that the effect of work input and temperature ratio on the scale of lost work dominates any local effects of rotation on boundary layer development and loss.

Based on the expression for impeller passage loss given in Eq. 2.19 and the definition of adiabatic efficiency, the impeller adiabatic efficiency can be expressed in the following manner:

$$\eta \approx 1-\left(\frac{f}{8}\right)\left(\frac{2N}{\pi}\frac{c}{D_{in}}\frac{s_{avr}}{s_{in}}+4N\frac{D_{in}}{s_{in}}\left(\left(\frac{D_e}{D_{in}}\right)^2-1\right)\right)\left(\frac{D_{in}}{D_e}\right)^2\frac{1}{\sin^2(\alpha)\cos(\alpha)}\left(1+\frac{\Omega^2 r_e^{\,2}}{C_p T_{Tin}}\right) \quad (2.20)$$

In the above expression efficiency is linked to friction factor, geometric factors, and work input factor. The eetted area is approximated in terms of rotor geometry. The work input factor

(giving temperature ratio) is approximated from the exit radius and the rotor angular velocity. The passage Reynolds number is used to calculate Darcy friction factor. For simplicity the expression given is for adiabatic impellers without back-sweep or slip velocity. N is the number of blades, c is the blade chord, s is the blade span, α is the blade inlet angle, and D is the rotor diameter. A similar, although more complicated, expression can be developed to account for back-sweep, slip, and effects of heat addition and casing drag on impeller efficiency. Such an expression will be interrogated to provide insight to impeller design in the next chapter.

2.6 CHARACTERIZATION

The simplified models discussed in section 2.5 describe the effects of the dominant limiting mechanisms on impeller performance. These models establish the scaling laws for the mechanisms and delineate the governing non-dimensional parameters. Based on the models for the effects of heat addition (q*), casing drag and passage boundary layer loss (Re and geometry), the impeller performance can be characterized in terms of non-dimensional parameters as follows:

$$\eta = f\left(\frac{m\sqrt{T_0}}{p_0}, \frac{N}{\sqrt{T_0}}, \mathrm{Re}, geometry, q^*\right) \tag{2.21}$$

$$\pi = g\left(\frac{m\sqrt{T_0}}{p_0}, \frac{N}{\sqrt{T_0}}, \mathrm{Re}, geometry, q^*\right) \tag{2.22}$$

These expressions lead to the statement that the only new parameter entering the performance characterization of micro-impellers compared to large conventional impellers is heat addition parameter, q*. The other parameters characterizing micro-impeller performance are corrected speed, corrected mass flow, geometry, and Reynolds number. For large compressors operating at large enough Reynolds numbers, dependence on Reynolds number is often omitted [32]. This is because for large Reynolds numbers boundary layer dissipation coefficient is nearly constant. This is not the case for micro-impellers, as the models suggest, and the dependence on Reynolds number is included.

CHAPTER 3

3 NON-ADIABATIC IMPELLER DESIGN GUIDELINES

3.1 INTRODUCTION

This chapter establishes the link between non-adiabatic, low Reynolds number flow processes in micro-impellers and impeller design. General design guidelines for non-adiabatic impellers are formulated to provide guidance and insight into micro-impeller design.

As described in Chapter 2, micro-compressor performance is characterized by an additional heat addition parameter (q*) related to non-adiabatic operation. The heat addition parameter, as defined in Chapter 2, is the total heat transfer to compressor flow divided by the total stagnation enthalpy at compressor inlet. It was also shown that micro-compressor performance is sensitive to the value of q*: if heat transfer to compressor flow becomes equal to compressor inlet flow stagnation enthalpy (a situation representative of micro compressor without any thermal isolation) the impeller isentropic efficiency is only 50% of its adiabatic value. The heat flow is proportional to the wetted area and the temperature difference between compressor wall and flow. The stagnation enthalpy at inlet is proportional to the mass flow. For a given temperature of the compressor wall, it would be beneficial to decrease the wetted area and increase the mass flow (if possible) in order to decrease heat addition parameter. This can be achieved by changing the blade geometry so as to achieve a higher mass flow and lower wetted area. However, by designing for higher mass flow and higher velocities in the compressor, and by changing geometry, the adiabatic performance of the machine may not be optimal anymore. The main question to pose is whether changing impeller geometry and perhaps sacrificing adiabatic aerodynamic quality but reducing the heat addition parameter can improve overall performance of non-adiabatic impellers. Is the impeller geometry for peak efficiency the same for an impeller operating in adiabatic conditions and one operating with high wall temperature and heat addition?

For instance increasing velocity at inlet by modifying blade inlet angle and velocity triangles would increase mass flow and reduce heat parameter. However, it was shown in Chapter 2, that impeller passage loss scales as inlet relative velocity cubed. Therefore, the higher velocities would lead to higher losses. Similarly, decreasing the blade count (solidity) and the radial size decrease the wetted area. Less blades (lower solidity), however, would lead to more slip velocity and more separation at impeller exit. The relative importance of these competing effects would determine the optimal impeller geometry. To answer the questions posed in the previous paragraph a compressor analysis tool is developed based on the characterization of micro compressors and the models developed in Chapter 2.

3.2 DESCRIPTION OF COMPRESSOR ANALYSIS TOOL

The compressor analysis tool is a one-dimensional, mean-line tool for analysis of compressor geometry. It assumes a diffuser pressure recovery coefficient based on 3D-CFD analysis to obtain stage performance. The main focus of the tool, however, is the compressor impeller. The

objective is to adequately describe the competing effects of changing impeller geometry on impeller aerodynamic quality and heat addition parameter. The tool is developed for shrouded impellers but can be modified for unshrouded ones. Adiabatic efficiency for the impeller is estimated with the following expression based on equations 2.16 and 2.19 given in Chapter 2 for impeller passage loss:

$$\eta \approx 1 - \frac{W_{lost}}{W_{in}} - \Delta\eta_{inlet} = 1 - \left(\frac{f}{8}\right)\frac{\rho_{in} V_{rel\_in}^3 A_{wet}}{W_{in}}\left(\frac{T_{Te}}{T_{Tin}}\right) - \Delta\eta_{inlet} \qquad (3.1)$$

where V_{rel_in} is a characteristic velocity for the impeller passage selected as the velocity at impeller inlet (the highest in the passage), ρ_{in} is the density at inlet, A_{wet} is the passage wetted area, W_{in}, is the work input to the flow calculated from velocity triangles, and T_{Te} and T_{Tin} are the stagnation temperatures at exit and inlet respectively in the absolute frame of reference. As noted in Chapter 2, friction factor for the passage f is estimated from Reynolds number based on passage hydraulic diameter at exit. The investigated cases are for impellers with right-angle inlet and $\Delta\eta_{inlet}$ denotes the decrement in isentropic efficiency associated with the inlet loss (estimated by 3-D CFD for the baseline impeller geometry).

The effect of heat addition on impeller performance with changing geometry can be determined from Gong's model [12] as described in Chapter 2 (Eqns. 2.1-2.3). To estimate heat addition parameter it is assumed that total heat to compressor for given compressor temperature scales linearly with compressor wetted area. Impeller inlet stagnation enthalpy is calculated from inlet stagnation temperature, specific heat, and mass flow.

3.3 PERFORMANCE TRENDS

The results from the compressor analysis tool are compared to available CFD results in Figures 3.1-3.4. The trends from the model are referenced to a baseline impeller (Table 3.1) of 8mm diameter rotating at design speed of 1.2 million RPM. All impellers have the same inlet blade span (400 um) and diameter ratio (2:1). The variation between inlet and exit blade span is linear with radius. Both model and CFD simulation include the right angle inlet loss although the model uses a constant value.

Table 3.1 Baseline impeller design information.

blade count, N	20	Mach inlet relative	0.83
diameter ratio, D_{exit}/D_{inlet}	2	Mach exit relative	0.38
blade span ratio inlet/exit	2	Mach exit absolute	1
blade inlet angle [deg]	-55	V relative exit / V relative inlet	1.8
blade exit angle [deg]	-45	exit angle relative [deg]	-60.9
rotational speed [rad/s]	125000	exit angle absolute [deg]	78.4
peripheral speed [m/s]	500	exit slip, $V_\theta/V_{\theta\_ideal}$ absolute	0.86
Re (from Eq. 2.17)	7160	exit swirl, V_θ/V_r absolute	4.9
heat parameter, q*	0		

Figure 3.1 presents changes in impeller isentropic efficiency with impeller blade inlet angle for different impeller wall temperatures.

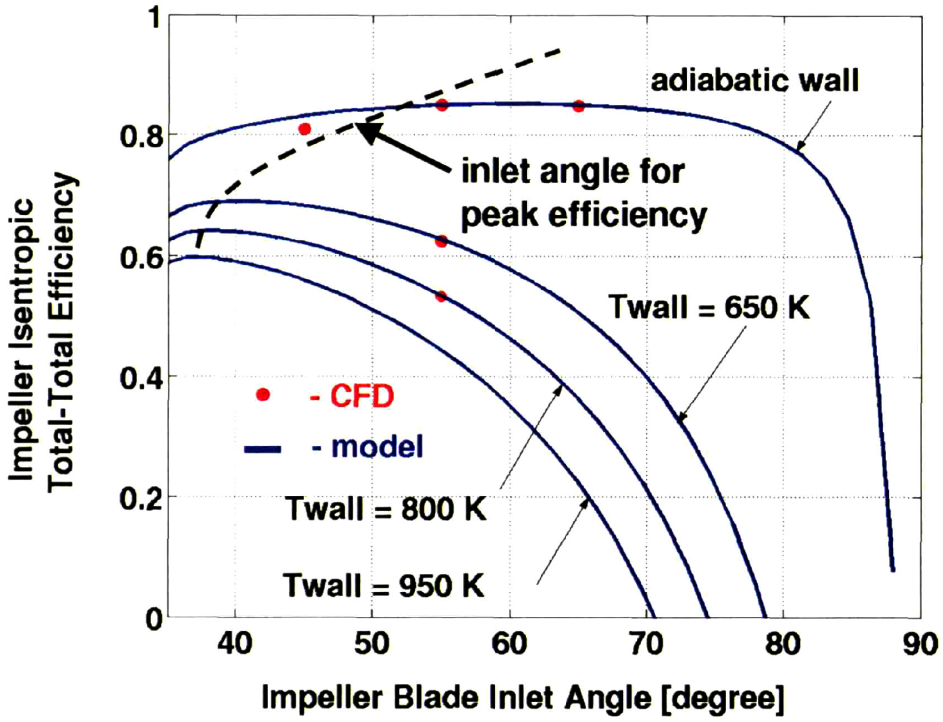

Figure 3.1 Shrouded impeller isentropic efficiency as a function of blade inlet angle and compressor wall temperature. Inlet angle for peak isentropic efficiency decreases with increasing temperature.

It is observed that the inlet angle corresponding to peak isentropic efficiency varies with impeller wall temperature. The inlet angle for peak isentropic efficiency decreases from that for the adiabatic impeller with increasing impeller wall temperature. Reducing inlet angle results in a higher design mass flow as well as higher inlet relative velocity. Increased mass flow leads to a reduction in heat addition parameter the benefit of which overwhelms the increased aerodynamic loss associated with the increased inlet relative velocity. The net effect on impeller efficiency is therefore beneficial.

The effect of blade back-sweep angle on impeller isentropic efficiency is presented on Fig. 3.2. The trend from the model shows deterioration in impeller performance for high back-sweep angles, a consequence of resulting elongated passages and reduced work input. This trend is in accord with CFD results. Again, it is observed that with increasing compressor wall temperature, the deterioration in impeller performance for high exit angles increases and begins at lower values of backsweep angle. The reasons are that wetted area increases with back sweep angle and thus heat transfer increases. At the same time, passage exit area decreases with increasing back sweep angle and thus mass flow decreases, increasing heat addition parameter. These trends are supported by CFD results. These trends explain the unexpectedly low performance of the initial MIT impeller designed with very high back sweep to control diffusion and operating at high temperatures.

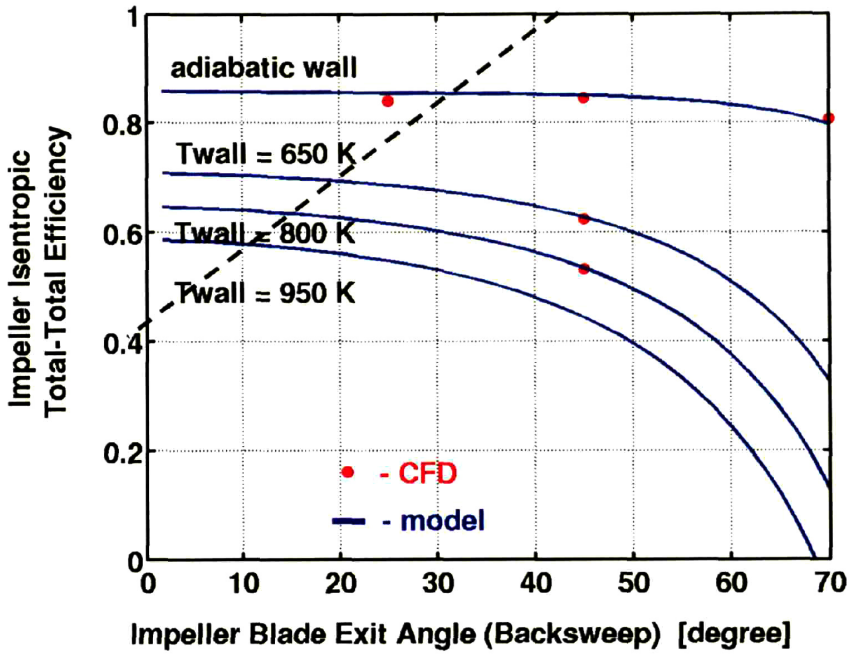

Figure 3.2 Shrouded impeller isentropic efficiency as a function of blade exit angle and compressor wall temperature . Maximum allowable exit angle value to avoid efficiency penalty decreases with increasing temperature.

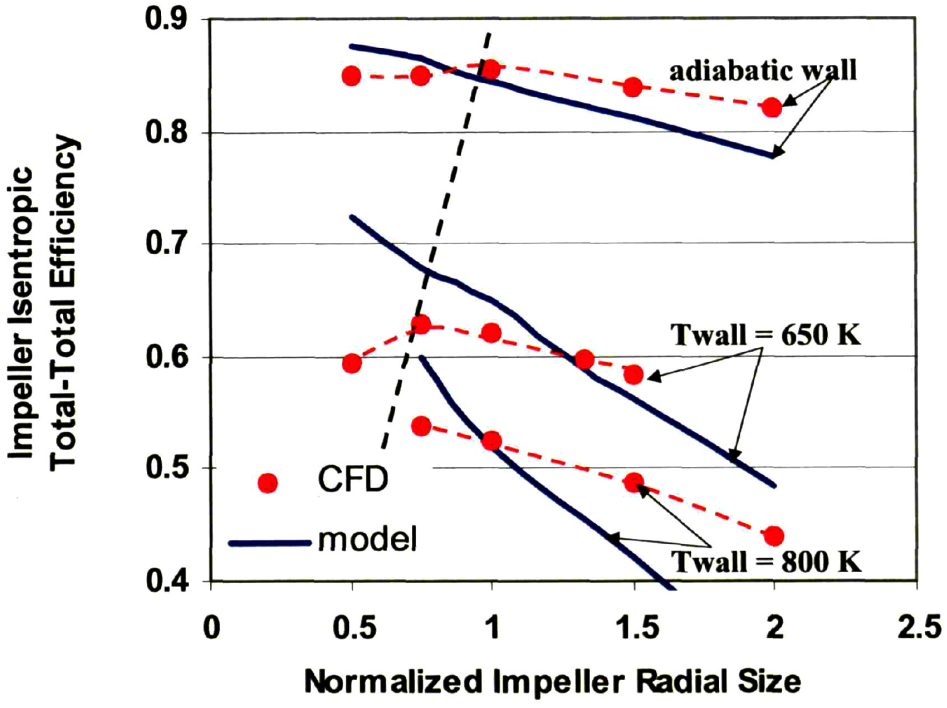

Figure 3.3 Shrouded impeller efficiency as a function of impeller radial scaling and wall temperature. Friction loss between rotating shroud and stationary casing is not included.

Figure 3.3 presents changes in impeller isentropic efficiency with impeller radial size for different impeller wall temperatures (tip speed fixed). It can be observed that there is a radial size for peak isentropic efficiency for micro-impellers of fixed tip speed and fixed blade span, which are real practical constraints for the micro impeller. They are related to the material strength and to the ability to etch silicon respectively. The impeller diameter for peak efficiency decreases with increasing wall temperature as shown by the CFD results.

The physical reason for the adiabatic efficiency increase as radial scale is reduced is the fact that wetted area decreases faster than mass-flow. Therefore, the relative importance of boundary layer loss decreases. This can be seen directly if we rewrite equation 3.1 as follows:

$$\eta \approx 0.95 - \left(\frac{f}{8}\right)\left(\frac{2N}{\pi}\frac{c}{D_{in}}\frac{s_{avr}}{s_{in}} + 4N\frac{D_{in}}{s_{in}}\left(\left(\frac{D_e}{D_{in}}\right)^2 - 1\right)\right)\left(\frac{D_{in}}{D_e}\right)^2 \frac{1}{\sin^2(\alpha)\cos(\alpha)}\left(1 + \frac{\Omega^2 r_e^{\,2}}{C_p T_{Tin}}\right) \quad (3.2)$$

In the above expression (Eq 2.20 in Chapter 2) efficiency is linked to the following geometric parameters: the number of blades, N, the blade chord, c, the blade span, s, the blade inlet angle, α, and the rotor diameter D.

If we scale down the impeller the only geometry term that changes in Eq. 3.2 is the ratio of inlet diameter to inlet span. This term decreases, hence the increase in efficiency.

Heat addition also scales with wetted area so that for cases with heat addition the benefit is larger. The competing effect responsible for the observed optima in impeller efficiency is that at some point, as the radial scale is further decreased, inlet effects are hypothesized to become important and to increase passage loss. These effects are not included in the model and predictions with the model do not suggest an optimal impeller size.

Figure 3.4 presents changes in impeller isentropic efficiency with solidity for different impeller wall temperatures. Trends in Fig. 3.4 suggest the existence of an optimal number of blades (solidity) for peak impeller efficiency. This is a reasonable trend because it is not hard to identify the competing effects. If we decrease the number of blades, the wetted area is reduced (and thus the heat flow is reduced) but the slip velocity and passage separation are increased. At adiabatic conditions both model and CFD suggest that the two effects are balanced for a large range of blade numbers and efficiency is nearly independent of blade number. With increasing wall temperature, however, the number of blades for peak efficiency decreases, because the benefit from reducing wetted area and heat transfer overwhelms the aerodynamic loss associated with reduced solidity.

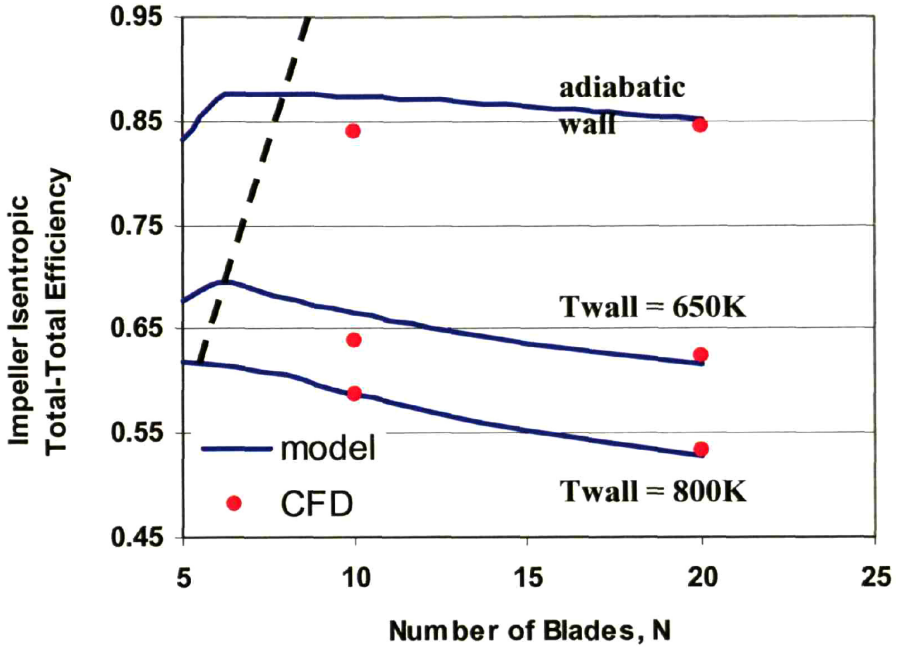

Figure 3.4 Impeller efficiency as a function of blade number and wall temperature. Results from model and CFD suggest decreasing optimum number of blades with increasing wall temperature.

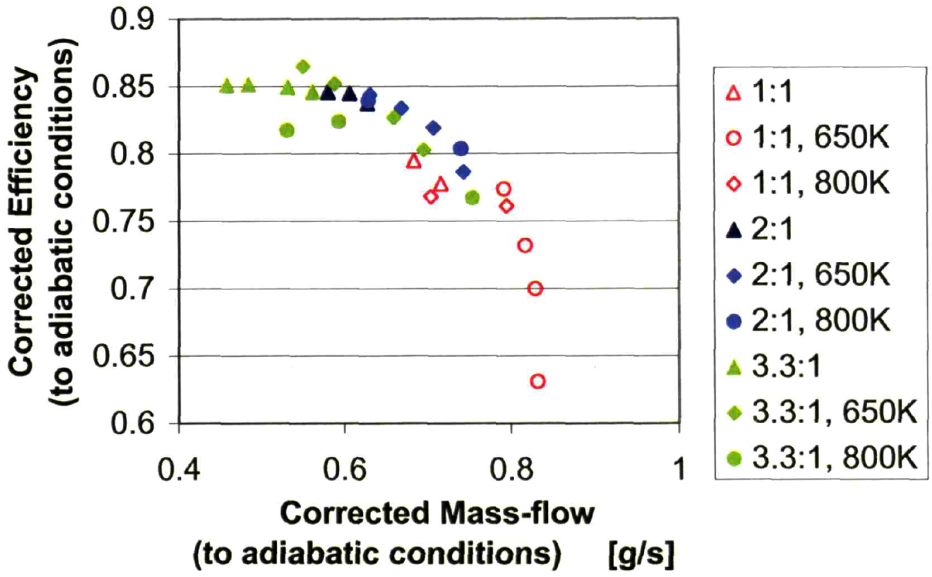

Figure 3.5 Effect of blade inlet-to-exit span ratio on impeller adiabatic and non-adiabatic efficiency. Note: All choked and near choking points are not shown except for 1:1, 650K case.

The effect of variable blade span geometry on impeller performance is also investigated. The ability to etch variable height blades is being developed by a team at the University of Maryland working in collaboration with MIT on the micro-engine project [26,27]. The effects of blade variable span are summarized in Fig. 3.5. Figure 3.5 presents impeller adiabatic efficiency as function of impeller mass flow for three different span ratio impellers at different operating wall temperatures.

Figure 3.5 implies that peak adiabatic efficiency improves with increasing inlet-to-exit span ratio. It is observed that higher variable span ratios shift the impeller operating range to lower mass-flows, lower inlet velocities and thus higher peak efficiencies. The improvement in peak adiabatic efficiency with reduction in inlet velocity can be explained if we use Eq. 2.19 from Chapter 2, and approximately express impeller efficiency on a given speed-line as follows:

$$\eta = 1 - \frac{W_{lost}}{W_{in}} = 1 - \frac{\sim V_{in\_rel}^3}{\sim V_{in}\omega^2 R^2} = 1 - (\sim \frac{\left(V_{in}^2 + \omega^2 R_{in}^2\right)^{\frac{3}{2}}}{V_{in}\omega^2 R^2}) \tag{3.3}$$

where W_{lost} is the lost work, W_{in} is the power supplied to impeller, ω is the rotating speed, R is the radius, V_{in} is the absolute inlet velocity, and V_{in_rel} is the relative inlet velocity.

A quadratic relation between inlet velocity (mass-flow) and efficiency follows for this type of machine, which is the curve on Fig. 3.5.

The possible shift of the operating range to lower mass flows and velocities with increasing span ratios is hypothesized to be related to passage diffusion limits. The effective area ratio in the impeller is high due to the increase in area with radius and the change in density from inlet to exit. As a consequence the flow in most impellers separates and little diffusion is possible in the passage. Thus a reduction in passage exit area (increase in span ratio) reduces separated regions and allows more diffusion and operation at lower mass flow and velocity. At a certain span ratio, however, the passage area ratio matches the required area ratio by the flow for maximum diffusion. Further increase in span ratio reduces mass-flow without any further diffusion and reduction in passage velocity. Consequently performance levels off. For the impellers of interest it is advantageous to fabricate span ratios of 2 but the benefit is negligible if the ratio is increased beyond 3 as can be seen from the results in Fig. 3.5.

3.4 DESIGN GUIDELINES

We can thus infer from the flow models and CFD solutions the following general design guidelines:

1. Micro-impellers should be thermally isolated as much as possible to avoid large performance penalties associated with heat addition.
2. Micro-impellers should be shrouded if possible to avoid significant penalty associated with casing drag (based on the results in Chapter 2).
3. Micro-impeller geometry for peak isentropic efficiency changes with wall temperature. If a micro-impeller is designed for adiabatic conditions but operates with high wall

temperature, a significant penalty may result which can be avoided by incorporating q* as a design variable.

4. There exists an inlet blade angle for peak isentropic efficiency, which decreases with wall temperature.
5. The maximum allowable blade back-sweep angle decreases with wall temperature.
6. Impeller solidity (blade count) for peak isentropic efficiency decreases with increasing impeller wall temperature.
7. Impeller diameter for peak isentropic efficiency (for given impeller tip speed) decreases with wall temperature.
8. Variable blade span is advantageous for micro-impeller performance with optimal inlet-to-exit span ratio near 2:1 for the investigated impellers.

Design charts such as these on Figures 3.1-3.4 can be generated with the impeller analysis tool for any impeller of interest for the selection of specific geometry. At the extremes of each parameter other effects may become important which are not included in the model. For example, at low inlet angles ($\alpha < 40$ degrees), the velocity triangles at design are such that the relative velocity entering the impeller blades becomes supersonic and there will be shock losses. Therefore, one should be careful if attempting to draw quantitative conclusions for flow conditions near parameter extremes without modifying the model. Intended design changes should be further investigated and confirmed with CFD.

3.5 DESIGN STUDY

To verify the validity of the observed trends and the suggested design guidelines a case study is performed as described in the following. Two impellers are optimized using the design guidelines for adiabatic operation (A) and for very high wall temperature (B) operation respectively. According to the design guidelines the two impellers should be different (Fig 3.6). For best performance, impeller B should have lower inlet angle to allow more mass flow, lower back sweep angle, blade count, and radial size to reduce wetted area and heat transfer.

The predicted performance by the model and CFD is shown. Design A performs slightly better than design B at adiabatic conditions as expected since design A is optimized for adiabatic operation. For operation with impeller wall temperature of 950K, however, impeller B outperforms impeller A significantly as suggested by the design guidelines. This result is confirmed by 3-D CFD analysis of the flow in the two impellers. The efficiency penalty for optimizing the impeller for adiabatic conditions and operating it at high wall temperature condition is higher than 11 points based on CFD. Therefore, it is important to design micro-impellers for given operating wall temperature using design charts generated by the analysis tool.

The operating temperature, however, cannot be obtained simply from knowledge of the impeller. Information about the whole engine system is required in order to estimate the temperature of the compressor. This emphasizes the importance of the coupling between components and system through heat transfer. There is thus a need for an integrated system model to account for this coupling on a systematic basis.

for adiabatic operation

for high wall temperature

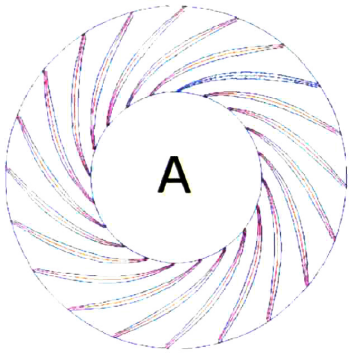

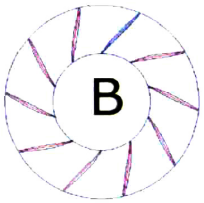

		Impeller A	Impeller B
Adiabatic	η	0.85 (0.85)	0.82 (0.82)
(Twall =450K)	π	4.7 (5.0)	4.6 (4.4)
	m	0.61 (0.41) g/s	0.88 (0.71) g/s
Hot	η	0.41 (0.42)	0.57 (0.53)
(Twall=950K)	π	2.3 (2.1)	2.9 (2.6)
	m	0.3 (0.29) g/s	0.59 (0.56) g/s

Figure 3.6 Adiabatic and non-adiabatic impeller design and performance from model and CFD (in brackets).

CHAPTER 4

4 DESCRIPTION OF INTEGRATED MICRO-ENGINE SYSTEM MODEL

4.1 INTRODUCTION

To function together as a system all of the components in the micro-engine must operate according to a given set of physical (matching) constraints. The interaction between the components is governed by conservation of mass, balance of power between compressor and turbine (or pressure ratio), and same rotational speed for the rotating components. In addition to the constraints relevant to a large engine the micro-engine components need to conserve energy by balancing the heat-transfer through the engine. This requirement changes significantly the behavior of the whole system. Most of the micro-engines represented by the results of preliminary cycle analysis are impossible to realize. The number of viable cycles is drastically limited due to the additional constraint. A system model is developed to enable cycle selection for micro-engines and to describe the system behavior with cycle parameters.

To analyze thermodynamic cycles for the system it is necessary to estimate heat flows within the engine (this amounts to synthesizing a thermal resistance network followed by its solution), adjust component performance for each set of system parameters, and account for all constraints (thermo and fluid dynamic, structural, material, fabrication, etc) and dominant performance limiting mechanisms. The developed system model outputs maps of the system design space, and delineates the effects of different parameters and constraints on system performance. The goal is to use the model as a design tool for identifying design options and for enabling the selection of a self-sustained micro-engine system. This chapter provides details about the modeling approach and a description of the developed models and modeling assumptions.

4.2 INTEGRATED SYSTEM MODEL OVERVIEW

The model as it is developed is of mixed analysis-design character and Figure 4.1 provides the framework of the modeling procedure.

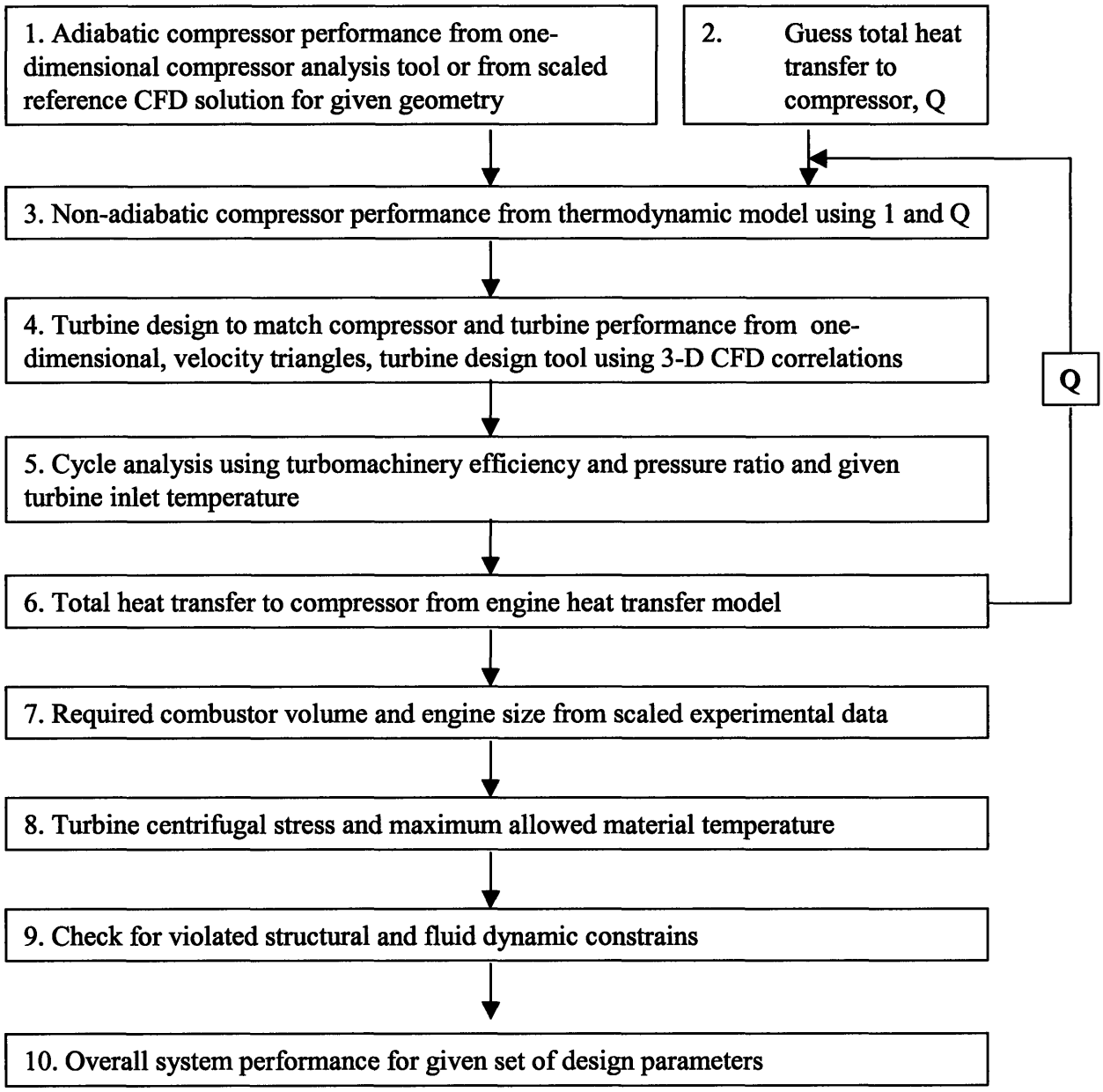

Figure 4.1 Diagram of modeling procedure.

The following sections describe the steps shown in Fig 4.1 in details.

4.3 ADIABATIC AND NON-ADIABATIC COMPRESSOR PERFORMANCE

The additional assumptions used in the determination of compressor performance are as follows:

1. **The compressor diffuser pressure recovery is established from 3-D CFD and is insensitive to operating conditions with high inlet swirl factor (10 to 50) and wall**

temperatures (400K to 950K): This assumption is based on micro-diffuser characterization by Gong using 3-D CFD [36].

2. **The impeller geometry may be designed for each selected rotating speed of the same aerodynamic quality (polytropic efficiency) as the one for the reference baseline compressor.**

3. **The compressor mass flow scales linearly with rotating speed:** For given blade geometry the velocity triangles at optimal condition remain similar and scale linearly with rotating speed.

4. **The compressor pressure ratio scales as shown in equation 4.2:** This expression is based on an estimate of compressor pressure rise using isentropic relations [33].

5. **The non-adiabatic compressor performance can be determined with the simple one-dimensional thermodynamic model by Gong from adiabatic performance and total heat to compressor:** The results from the thermodynamic model by Gong are in accord with 3-D CFD results (within 5%) [12].

The adiabatic compressor performance can be estimated in two ways. First, a representative 3-D CFD (FLUENT) solution for the geometry and near the operating conditions of interest can be used. To scale it to the exact conditions of interest which may change from case to case (peripheral speed) the polytropic efficiency is assumed to remain unchanged while the pressure ratio and mass flow can be scaled with rotor speed in the following manner:

$$\dot{m} = \dot{m}_{ref} \frac{\omega}{\omega_{ref}} \tag{4.1}$$

$$\pi = \left(\left(\pi_{ref}^{\frac{\gamma-1}{\gamma}} - 1 \right) \frac{\omega^2}{\omega_{ref}^2} + 1 \right)^{\frac{\gamma}{\gamma-1}} \tag{4.2}$$

Another way of estimating adiabatic compressor performance for different geometries and different operating conditions is to use the compressor analysis model as described in Chapter 3.

Once an estimate of the compressor adiabatic performance is obtained the non-adiabatic performance can be estimated from the adiabatic one and the total amount of heat transfer to compressor flow with the thermodynamic model by Gong (Chapter 2). Since the total amount of heat transfer is unknown an initial guess is required which is iteratively updated with the results from the engine heat transfer model.

4.4 MATCHED TURBINE DESIGN

The main assumptions for the turbine in addition to those used in the design code are:

1. **The turbine geometry designed with the one-dimensional tool and the predicted performance are representative of real 3-D micro-turbines:** This is a reasonable assumption because turbine rotor performance is extracted directly from 3-D CFD and the effects of the dominant performance limiting mechanisms in the turbine are predicted with correlations based on 3-D CFD

2. **The turbine blades can be manufactured with blade height of up to 1 mm:** This assumption is based on current micro-fabrication capability [37].

The design of the turbine is carried out for each set of system parameters with a one dimensional, velocity triangles code, developed by Gong. A detailed description of this code and the assumptions used in it can be found in Phillipon [17] and Evans [24]. The code uses correlations from 3-D CFD for some of the dominant performance limiting mechanisms like NGV loss and turbine exit loss. The code needs as input representative turbine rotor isentropic efficiency (85% for current turbine), which is obtained from 3-D CFD (FLUENT).

4.5 THERMODYNAMIC CYCLE ANALYSIS

The net shaft work produced by the engine system is the work of the turbine minus the work of the compressor and minus any other parasitic power loses as given in Eq.4.3 below. The parasitic power losses come from the journal and thrust bearings, turbine rim gap, compressor shroud, and shroud seal, and shaft flows. The parasitic power losses for the micro engine are significant compared to the power output. The power losses in the journal and thrust bearings are estimated with Couette flow models by Teo [38]. The other parasitic power losses are discussed in the following sections.

$$W_{net} = W_{turbine} - W_{compressor} - W_{parasitic} \tag{4.3}$$

Engine efficiency can be estimated by comparing the available net shaft power to the amount of energy added to the combustor flow in the form of fuel (Eq. 4.4). This energy is equal to the change in stagnation enthalpy of the flow from inlet to exit of the combustor divided by the combustor chemical efficiency.

$$\eta_{engine} = \frac{W_{net}}{\dot{m} C_{p\_avr}(T_{ce} - T_{ci})/\eta_c} \tag{4.4}$$

where $\dot{m}$ is the mass flow passing through the combustor, *Cp* is an appropriate average specific heat for the combustor flow, and *Tce* and *Tci* are the exit and inlet stagnation temperatures of the flow passing through the combustor.

The assumptions used in the cycle analysis are:

1. **The dissipated power in journal and thrust bearings can be estimated with Couette flow models:** Based on CFD calculations the dissipated power in the bearings can be

estimated with Couette flow models. More information about the validity of this assumption can be found in reference [38].

2. **The specific heat used in the combustor flow is the average of the specific heats of the flows at combustor inlet and exit:** A more accurate estimate would be to calculate the energy released by the fuel through accounting for the changes in the flow properties in the burner and integrating to find the change in enthalpy.

4.6 HEAT TRANSFER MODEL

The system heat transfer model consists of three heat transfer modules shown in Fig 4.2 to account for all heat sources and heat paths to the compressor flow.

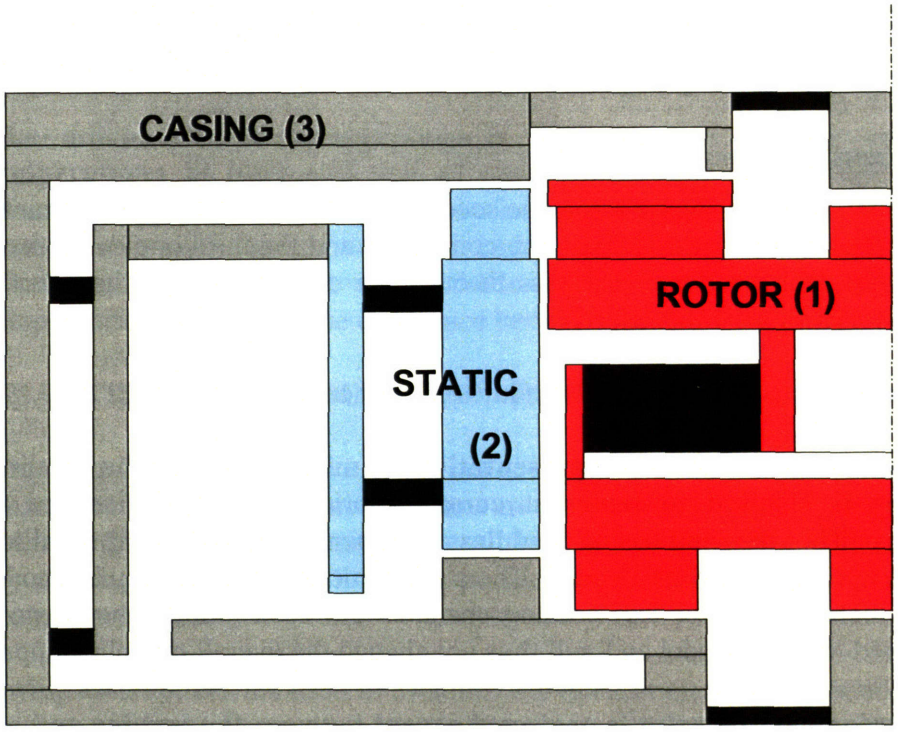

Figure 4.2 Baseline micro-engine layout. Three heat transfer modules for integrated system model: Rotor in red - (1), Static Structure in light blue- (2), Casing in grey - (3) and structural connecting bridges in black.

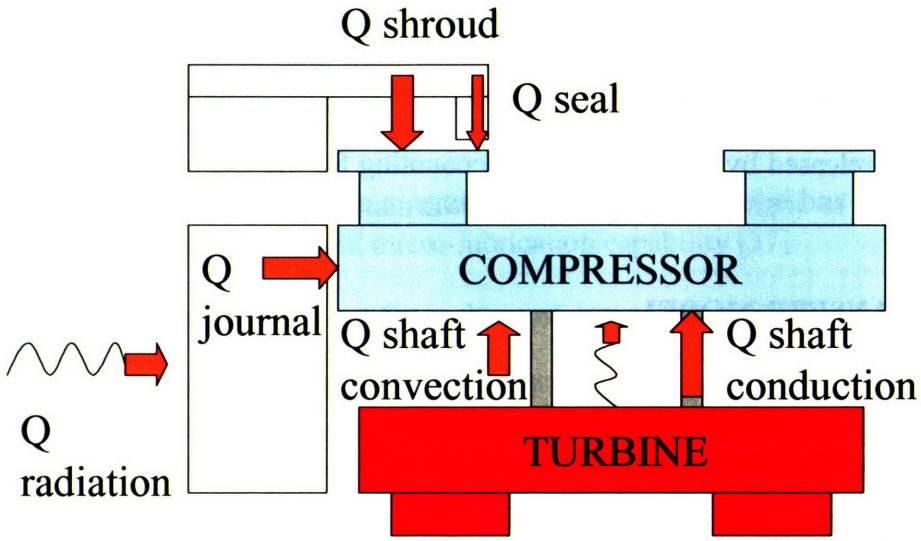

Figure 4.3 Heat transfer to micro-compressor

The first module includes the engine rotor, the second one consists of the static structure around the rotor and the cooling flows that bypass the combustor and the third one consists of the static casing of the engine and the flows that pass through the combustor. At the interfaces of the modules mass and heat flows are conserved.

The following assumptions are used in all modules of the heat transfer model:

1. **The selected engine layout is representative for micro-engines:** The baseline layout of the engine is selected to represent current fabrication capabilities and component geometries. The rotor and casing modules are generic and are not expected to change in the future except for scaling in size. The static structure module may be modified in the future to include more or less cooling channels but such modifications can readily be incorporated into the model and will thus not change the overall modeling approach.

2. **The radiation heat transfer is neglected except between the turbine and compressor disks:** All heat transfer modes (conduction, convection, and radiation) are accounted for. They are indicated in Fig 4.3. The radiation heat transfer that reaches the compressor is about two orders of magnitude smaller than the combined conduction and convection heat transfer and is neglected in the model. The only radiation heat transfer that may be of interest is the one from the turbine disk to the compressor disk and it is included in the model. Estimates for the radiation heat transfer to the compressor are given at the end of Appendix A.

3. **The micro-engine structure is separated into different isothermal blocks (compressor disk blades and shroud, turbine disk and blades, static structure, five casing blocks, etc):** The turbine, compressor and static structure block can be assumed isothermal because of the low representative Biot number (0.01-0.02). The blocks of the casing structure are not nearly isothermal but can be represented as several connected isothermal blocks. Their temperature represents the average temperature of the blocks.

This is acceptable for the purpose of the model because the exact temperature profile of the casing is not needed. The important information is the overall thermal resistance of the casing and the heat passing through the end block, which forms the compressor inlet.

4. **The convective heat transfer coefficients in the turbomachinery remain constant for the investigated range of geometry and operating conditions:** Heat transfer coefficients for the impeller, turbine, diffuser and NGV passages are extracted from 3-D CFD for representative geometry and operating conditions. These values are not expected to change appreciably for changes in geometry and conditions near the reference condition. For channel laminar flows Nusselt number is constant while for turbulent flows Nusselt number depends on Reynolds number (to power 0.8-0.85) and Prandtl number [39]. For air Prandtl number is nearly constant and Reynolds number will change according to the changes in scale of the turbomachinery. Sensitivity of system performance to heat transfer coefficients will determine the acceptable range for geometric scaling and changes in flow conditions so that the uncertainty in the output is held within the desired limits.

5. **The adiabatic wall temperature is the average of flow relative stagnation temperatures at inlet and exit of each component or passage:** Viscous heating becomes important for high-speed flows with a Mach number beyond 3 [39]. Turbomachinery flows are characterized by much lower Mach numbers near unity and it is common to approximate the adiabatic wall temperature with the relative stagnation temperature of the flow. The difference between the two is estimated to be below 5 K.

4.6.1 HEAT TRANSFER MODULE ONE - ROTOR

Module One consists of the engine rotor. This is the main as well as the most important module. Both compressor impeller and turbine rotor are part of this module along with the thermal isolation shaft. This module estimates overall heat to compressor and thus determines turbo-machinery performance and overall system performance. Figure 4.3 indicates all the heat flow paths to compressor flow.

The following assumptions are used in Module One in addition to those stated in Section 4.5:

1. **The turbine and compressor disks are modeled as parallel diffuse gray bodies:** To estimate radiation heat transfer between turbine and compressor disks an expression developed for diffuse gray bodies is used [39].

2. **The journal bearing and shroud seal flows are thermally and aerodynamically fully developed:** These flows are characterized by low Reynolds number (100-300) based on hydraulic diameter. Entrance length is very short compared to channel length and the flows are fully developed for most of the passage. This is confirmed by CFD.

3. **The heat transfer through the shroud cavity (between the engine casing and compressor shroud) and the shaft flows (between the turbine and compressor disks) can be modeled with constant effective thermal conductivity in the gaps extracted from CFD solutions**: The flows in the shaft and shroud gaps may be complicated and detailed characterization is not attempted. Heat transfer is calculated for simple

representative geometry and effective thermal conductivity in the gaps is extracted from the solution. CFD is used to guide the scaling of these effects for the parameter range of interest.

4. **The dissipated power in the shroud cavity and the shaft flows scales with angular velocity to the third power and outer radius to the fifth power as for enclosed rotating disks**: CFD solutions for representative geometry and conditions suggest that this is the case for the shroud gap as is expected because the shroud gap is an enclosed rotating disk. The dissipated power in the shaft gap is modeled in the same way, because conceptually the situation is similar to enclosed rotating disk.

5. **The heat transfer between the turbine disk and the static structure is ignored:** There is a large air gap between the turbine disk sidewall and the static structure (~50 microns) instead of a journal bearing, which is assumed to thermally isolate the static structure from the hot turbine. Even if some heat transfer takes place through the gap the thermal resistance of the heat path through the static structure is higher than the resistance through the shaft to the compressor flow. Therefore less heat would be allowed to the compressor. Consequently, the assumption that the heat transfer from the turbine takes place through the isolation shaft only is a conservative one.

The total heat transfer to the compressor flow can be estimated with the resistance network shown in Fig 4.4. The driving temperatures of the compressor and turbine flows depend on the compressor and turbine inlet flow temperatures (given) and the amount of heat transfer taking place (unknown). Therefore, an initial guess of the total amount of heat transfer is necessary and an iterative procedure is used to solve the problem. Initial guesses are also provided for the compressor and turbine temperatures to estimate the radiation heat transfer which is then provided to the linear system as a known quantity.

To solve the thermal resistance network for the engine rotor it is necessary to first estimate the thermal resistances of all connections (Appendix A). Then using the boundary conditions (turbine and compressor flow inlet temperatures, static structure and casing temperatures) the problem can be solved. There are seven equations linking heat flows to driving temperatures and resistances, and two energy conservation equations stating that the net heat transfer to the compressor and turbine structures is zero (Appendix A). These nine (9) equations are solved for the nine unknowns: compressor and turbine structure temperatures and seven heat transfers. The radiation equation is non-linear in temperatures and is solved iteratively.

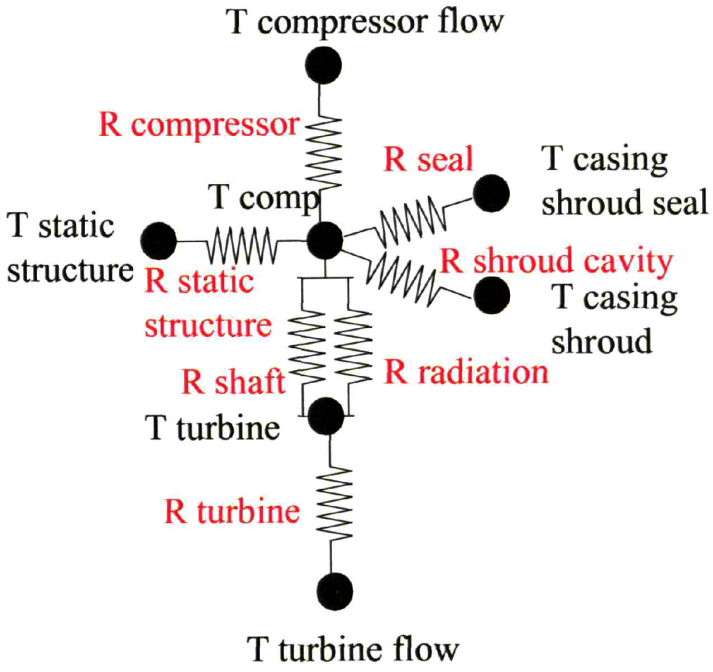

Figure 4.4 Thermal resistance network for engine rotor to find total heat flow to compressor and compressor structure temperature. T denotes temperature and R resistance.

4.6.2 HEAT TRANSFER MODULE TWO – STATIC STRUCTURE

Heat transfer module Two describes the heat flow through the static structure around the rotor.

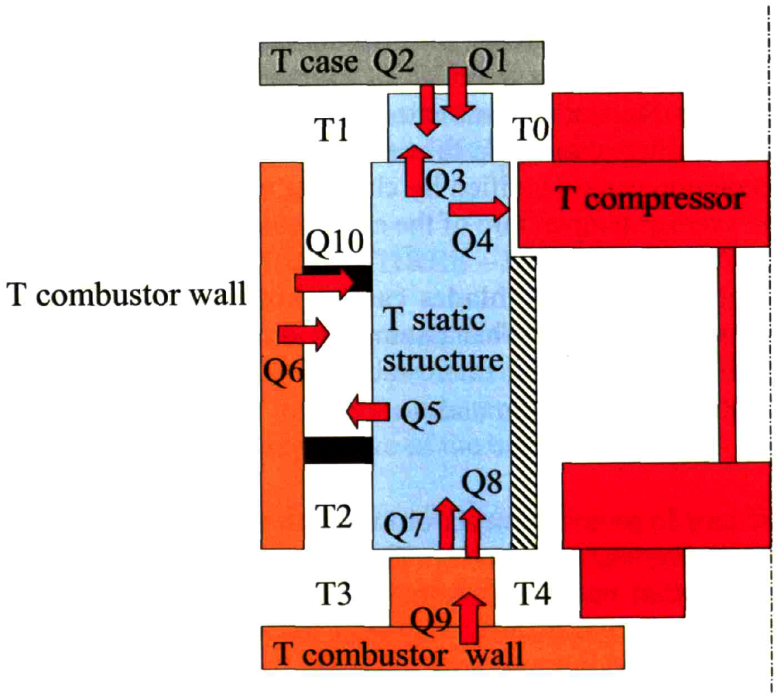

Figure 4.5 Heat flow through static structure.

The assumed heat flow directions are shown on Fig 4.5. The flow at impeller exit has stagnation temperature T_0. As it passes through the diffuser it is heated by both the engine casing (Q_1) and by the static structure (Q_3) and exits with stagnation temperature T_1. Heat also passes from the engine casing to the static structure through the diffuser blade tips and blades (Q_2). All of the compressor mass flow passes through the diffuser and exits with temperature T_1. Then the flow is split into two parts – main flow and combustor bypass flow. The combustor bypass flow passes between the static structure and the combustor sidewall. Both the static structure (Q_5) and the combustor wall (Q_6) heat this bypass flow up to the exit stagnation temperature T_2. The main flow continues all the way around the combustor, enters the combustor where combustion takes place, and exits with the combustor exit temperature. At exit the two flows meet and mix out to the turbine inlet temperature T_3. It is assumed that they mix out instantly so that no film cooling benefit from the cooler bypass flow is realized downstream through the NGVs and the turbine. This is a conservative assumption because the mixing of the two flows will take place over some finite length and some cooling benefit will certainly exist. The turbine NGV's are attached to one of the combustor walls extending from the combustor and therefore the whole structure is assumed to be at the combustor wall temperature. As the mixed out flow with temperature T_3 enters the NGV's it is heated by the combustor wall (Q_9) and cooled by the static structure (Q_7) to reach temperature T_4. Heat also passes directly from the combustor wall to the static structure (Q_8) through the NGV blade tips and blades (see Fig A.7 in Appendix A). Heat also passes from the sidewalls of the combustor to the static structure through structural bridges (Q_{10}).

The following assumptions are used in Module Two in addition to those stated in Section 4.5:

1. **The bearing flows require a small fraction of total mass flow (1-3 %) near the design condition. The air bled from the compressor through the bearings entering the turbine rotor does not have an effect on the average turbine inlet temperature and the work output of the turbine:** The validity of this assumption can be verified by setting the bleed level in the model to 1-3% and determining the overall effect on performance. For the cases of interest the effect is small.

2. **The temperature profile in the combustor bypass cooling flow is not fully developed at the exit of the cooling passage so that the heat from the combustor remains in the flow:** This assumption can be verified by checking whether the flow temperature at exit has assumed the average temperature of the combustor and static structure walls.

3. **The diffuser and turbine NGV blades can be hollowed near the tip to reduce the surface area for heat transfer:** This assumption is related to manufacturing capabilities and is considered feasible by the micro-fabrication group [37]. The thickness of the hollow blade walls is set to 20 μm and the depth of the hollow gap to 100 μm (see Fig A.7 in Appendix A).

4. **The combustor and bypass flows mix out instantly to a uniform temperature before they enter the turbine NGV passages:** This is a conservative assumption ignoring any film cooling benefit that may result from the cooler bypass flow passing on the NGV hubs and turbine disk.

5. **The heat transfer from the turbine NGV passage takes place at the turbine NGV inlet effectively reducing the turbine inlet temperature:** This is a conservative assumption to bound the detrimental effect of NGV cooling on turbine performance.

6. **The pressure loss in the bypass cooling passage is the same as that for the combustor flow:** This is a conservative assumption because the combustor flow passages including the combustor are longer than the bypass flow passages while geometry and flow conditions are similar.

7. **The heat transfer coefficients for the bypass flow can be determined using expressions and correlations for laminar flat plate flow:** It is easy to verify that the bypass flow is laminar by calculating Reynolds number (100-300). Based on assumption 2 the flow is not fully developed and therefore a flat plate flow approximation is appropriate for the flows on the combustor and static structure walls.

8. **The flows remain attached in the diffuser, turbine NGV, and bypass flow passages:** Near design condition it is not expected that large separation regions or recirculation zones will appear in the passages to change heat transfer coefficients appreciably.

To solve for the heat flows and the unknown temperatures a linear system of fifteen (15) equations is solved (Appendix A). For each segment of the flow the conservation of energy equations are written. The change in flow enthalpy (or stagnation temperature) between inlet and exit equals the net heat transfer to the flow. There are a total of 3 conservation equations for the diffuser, combustor bypass, and NGV flows. A fourth conservation equation is that the net heat flow from the static structure is zero. Another equation describes the mixing of the combustor and combustor bypass flows, which are at different temperatures, given the mass flows of both. Ten equations describe each heat transfer interaction and link the heat transfer to the driving temperatures and resistances. The fifteen unknowns are the ten heat transfer interactions, the four fluid temperatures at different stations and the temperature of the static structure. The remaining information needed to solve the system is the resistances linking the driving temperatures to the levels of heat transfer (Appendix A).

4.6.3 HEAT TRANSFER MODULE THREE – ENGINE CASING

Heat transfer module Three describes the heat flow through the static engine casing shown in Fig 4.6. The engine casing structure is separated into several blocks, which are assumed isothermal as indicated in Fig 4.7. The constant temperature of each block in the model can be thought of as the actual average temperature of the block.

The assumed heat flow directions in the model are shown on Figure 4.6. The flow enters the engine with ambient temperature Tc_0. Before it reaches the compressor it is heated by the engine casing (Q_1) to stagnation temperature Tc_1. As the flow passes through the impeller it is heated by the total heat transfer to the impeller flow estimated in module One. This is the heat coming from the turbine through the shaft, the static structure through the compressor journal, and the engine casing through the shroud (Q_2 and Q_3). The flow exits the impeller with stagnation temperature Tc_2 which accounts for the added heat and work in the impeller. Next the flow

passes through the diffuser passages and the heat interaction is estimated in the same way as it is done in module Two. Heat crosses from the engine casing to heat the flow (Q_5) and through the blade tips to heat the static structure (Q_6). The heated flow exits the diffuser with temperature Tc_3 to be separated into bypass cooling flow (the topic of module Two) and combustor flow.

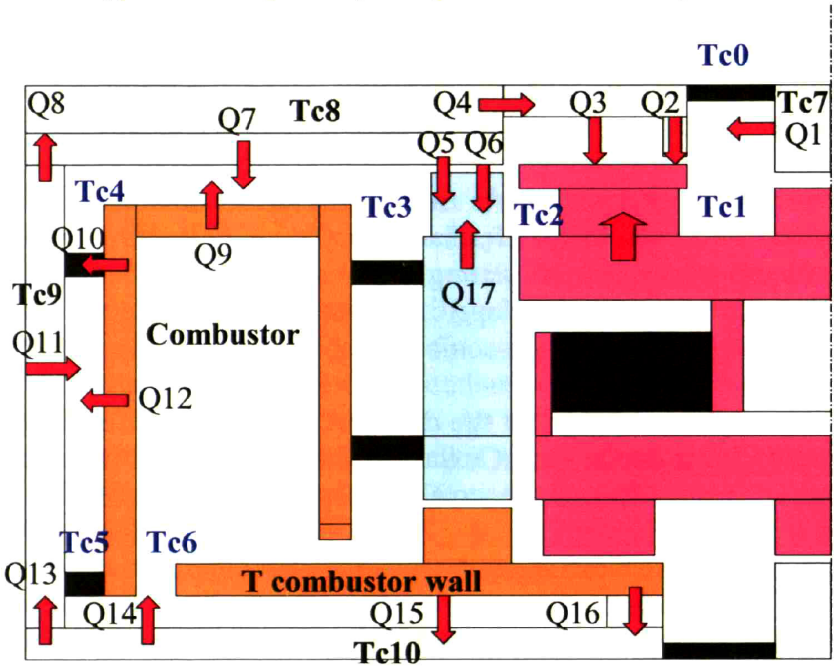

Figure 4.6 Heat flow through Engine Casing.

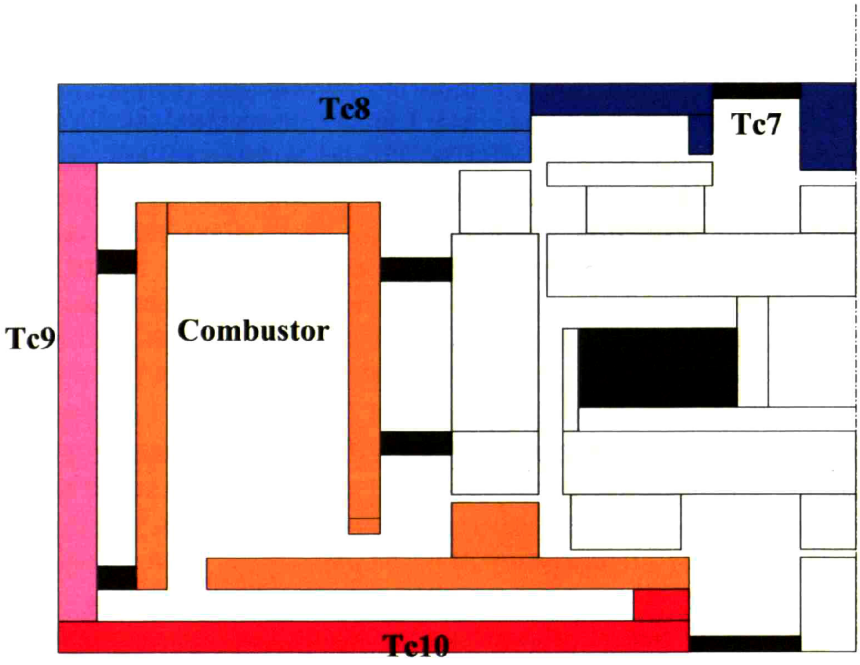

Figure 4.7 Isothermal Blocks of Engine Casing Model

The combustor flow passes between the casing and the combustor to reach the outer edge of the combustor at temperature Tc_4. Tc_4 is higher than Tc_3 because both the engine casing (Q_7) and the

upper combustor wall (Q_9) heat the flow. Then the flow turns ninety degrees to continue its way towards the entrance of the combustion chamber by passing between the engine and combustor outer sidewalls. In this channel the casing wall (Q_{11}) and the combustor wall (Q_{12}) heat the flow to temperature Tc_5. Before the flow enters the combustion chamber it is also heated by part of the bottom casing wall (Q_{14}) to temperature Tc_6. The bottom combustor wall which extends to become the base for the turbine NGVs and the casing for the turbine rotor is assumed to be isothermal as discussed in module Two and at the given combustor wall temperature. The flow between this structure and the engine casing (bottom) is dead flow. Heat passes from the combustor wall and the turbine NGV's through the dead flow by conduction (Q_{15}) to casing structure block 10 which is at temperature Tc_{10}. Heat also flows from the combustor wall (Q_{16}) through the turbine rotor casing to block 10 by conduction. Heat flows from block 10 to block 9 through conduction (Q_{13}), from block 9 to block 8 by conduction (Q_8) and from block 8 to block 7 by conduction (Q_4).

The following assumptions are used in Module Three in addition to those stated in Section 4.5:

1. **The convective heat transfer coefficients in the combustor flow cooling channels can be determined from analytical expressions and correlations for laminar channel flow.**

2. **The casing structure can be modeled as five connected isothermal blocks:** It is the overall resistance of the casing structure that is of interest and not the exact wall temperature profile. The resistance between two blocks is modeled as the material resistance between their centers. The thermal resistance can be estimated from geometry and silicon conductivity.

To find the unknown flow temperatures (Tc_1-Tc_6), structure temperatures (Tc_7-Tc_{10}), and heat flows (Q_1-Q_{17}) a linear system of twenty seven (27) equations is solved (Appendix A). There are 17 equations describing the heat transfers with links to the driving temperatures and resistances. There are also 6 energy conservation equations relating the changes in flow temperature from inlet to exit to the net heat transfer to the flow. Finally there are 4 energy conservation equations for the structural blocks stating that the net flow of heat from each material block is zero.

As in module Two the remaining work is to estimate the resistances linking the heat flows to the temperatures of interest and this is described in Appendix A.

4.6.4 HEAT TRANSFER MODEL EXECUTION

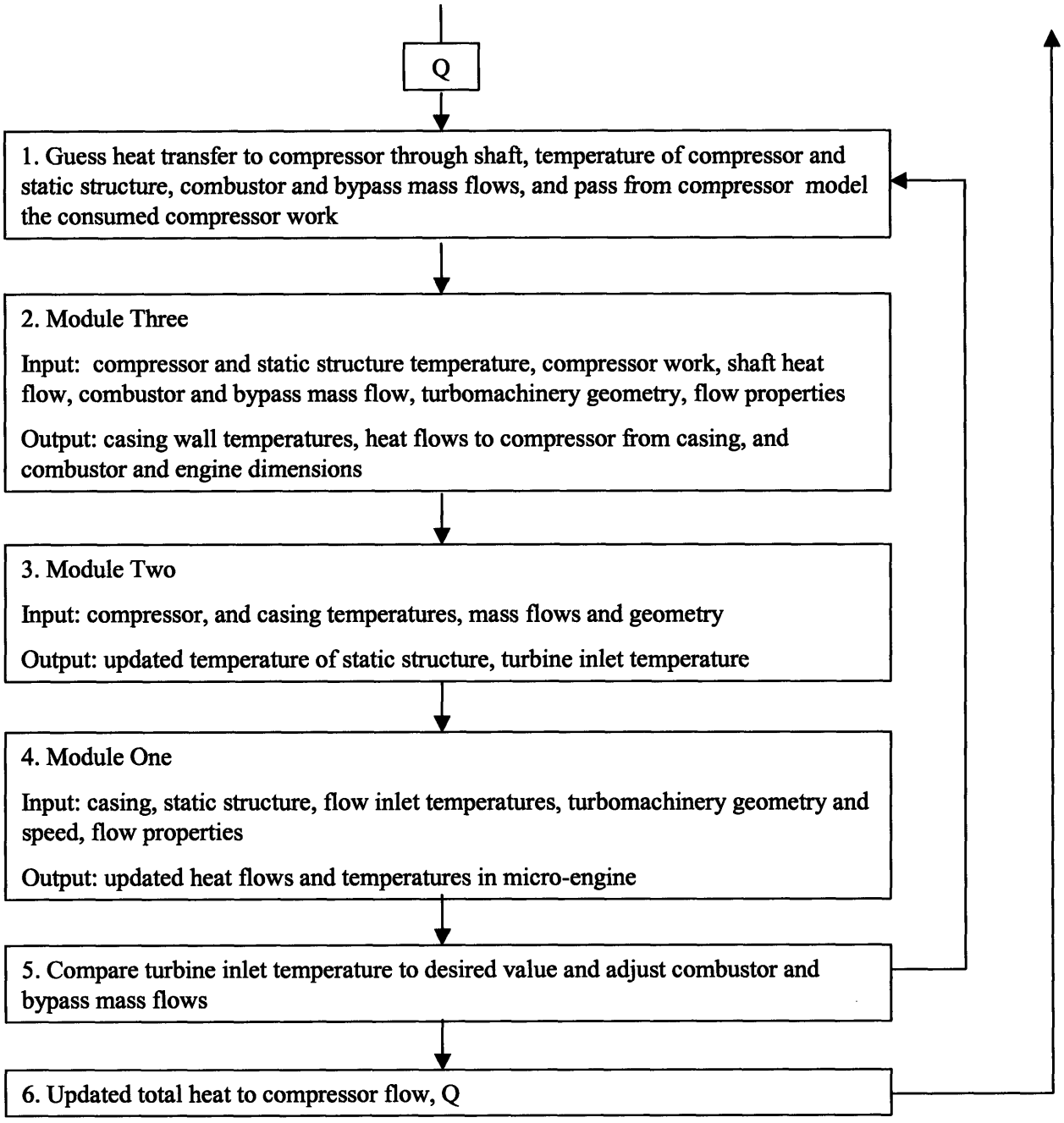

Figure 4.8 Iterative solution method for heat transfer model

To solve for the heat flows and temperatures of interest in the engine the three modules are solved iteratively as part of the main iteration procedure over the total heat transfer to

compressor flow. The procedure is delineated in Fig. 4.8. An initial guess is provided to module Three of the compressor and static structure temperatures, the heat flow through the shaft, flow properties and ratio of combustor and bypass mass flow. The results from module Three and the initial guess are passed to module Two, and the results from module Two and the initial guess are in turn passed to module One as delineated in Fig 4.8. Then, the initial guess in module Three for the combustor mass flow (after the flow splits) is adjusted in a new iteration until the desired turbine inlet temperature is achieved. The main output of the heat model which is the total heat transfer to the compressor flow is then send to update the input in the non-adiabatic compressor performance model to continue the iterations in the cycle shown in Fig 4.1 nesting the other iterative procedure over the mass flow. In this way the information required in module Three as initial guess is also updated for each iteration.

4.7 COMBUSTOR PERFORMANCE AND REQUIREMENTS

To estimate the required combustor volume for each set of system design parameters available experimental data collected by Mehra [40] is used. The tested combustor was a dual zone hydrogen combustor and demonstrated a combustor exit temperature of 1800 K, pressure ratio of 0.98 and efficiency of 0.95. The combustor operated at pressure ratio of 1.15, mass flow of 0.12 g/s, volume of 191 cubic mm, flow residence time of 0.4 ms, height of 1mm, outer radius of 9.2 mm and inner radius of 4.8 mm. The combustor wall temperature was measured to be 1100 K. The combustor volume is directly proportional to the required residence time, and the mass flow, and inversely proportional to the pressure ratio to the power of $1/\gamma$ (related to the density of the flow) [33].

$$Vol = \frac{C \dot{m} \tau_{res}}{\pi^{\frac{1}{\gamma}}} \tag{4.5}$$

From the data from the experimentally tested combustor the constant of proportionality is estimated to be C = 4.4. This value of C is used in equation 4.5 to estimate the required combustor volume for any mass flow, and pressure ratio.

With the baseline engine layout and an estimate for combustor volume using Eq. 4.5 the overall engine dimensions can be determined. To estimate the outer radius of the engine the width of the combustor flow cooling channel and the combustor and casing walls need to be added to the combustor outer radius.

The main assumption used in determining combustor requirements is:

> **If the residence time remains unchanged, the combustor performance will remain the same if geometry is scaled:** This assumption is based on the idea of keeping the Damkohler number in the combustor the same. If the volume is scaled for the given mass flow and pressure ratio so that the residence time remains the same, then the Damkohler number will remain the same because the chemical reaction time is fixed [41].

4.8 TURBINE STRUCTURAL CONSTRAINTS

The centrifugal loads on the turbine blades and disk induce centrifugal stresses and bending moments in the turbine. The maximum allowable stress in the turbine depends on the turbine material and also on the operating temperature. Turbine life is limited by creep in silicon and design guidelines for silicon-silicon carbide hybrid structures are provided by Moon [14] for estimated turbine life of several hours to several days. These design guidelines are presented in Fig 4.9.

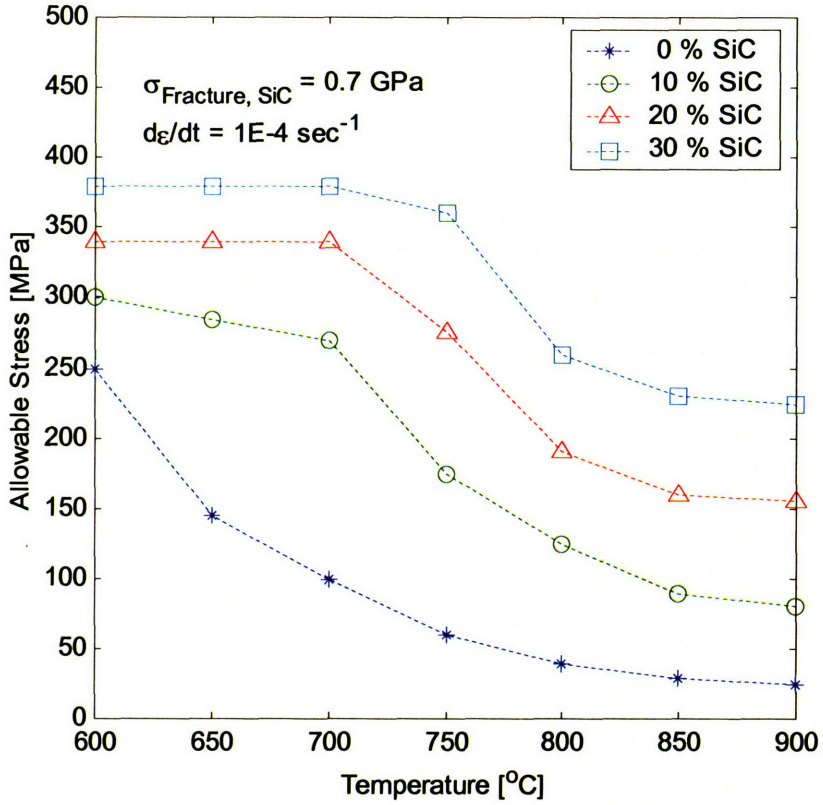

Figure 4.9 Turbine structural design guidelines (Moon)

The design guidelines are used in the form of a look-up table in the model. For given level of silicon-carbide in the turbine structure the code uses linear interpolation between the given data points to estimate the maximum allowable temperature for given stress level.

The centrifugal stress in the center of the disk is estimated as a function of disk rotational speed, radius, and material properties [42] by:

$$\sigma_{max} = \frac{3+\nu}{8}\rho\omega^2 r^2 \tag{4.6}$$

where ν is the Poisson ratio and ρ the density of the material, ω is the angular velocity and r is the radius of the disk.

To estimate the stress in the blade roots the blades are modeled as cantilevered beams acted on by the centrifugal force *Fc* as indicated in Fig. 4.10. The centrifugal force is determined in equation 4.7. The centrifugal force is assumed to act on the center of mass of the blade so that a bending moment is present in the blade. This bending moment can be determined with Eq. 4.8. It causes the maximum stress at the blade root to appear at the leading and trailing edges. For simplicity the blade is assumed radial. Moment of inertia for the blade is estimated from simplified blade geometry as given in Eq. 4.9. The maximum stress at the blade roots can be found from the bending moment, the moment of inertia and geometry [42] as described by Eq. 4.10.

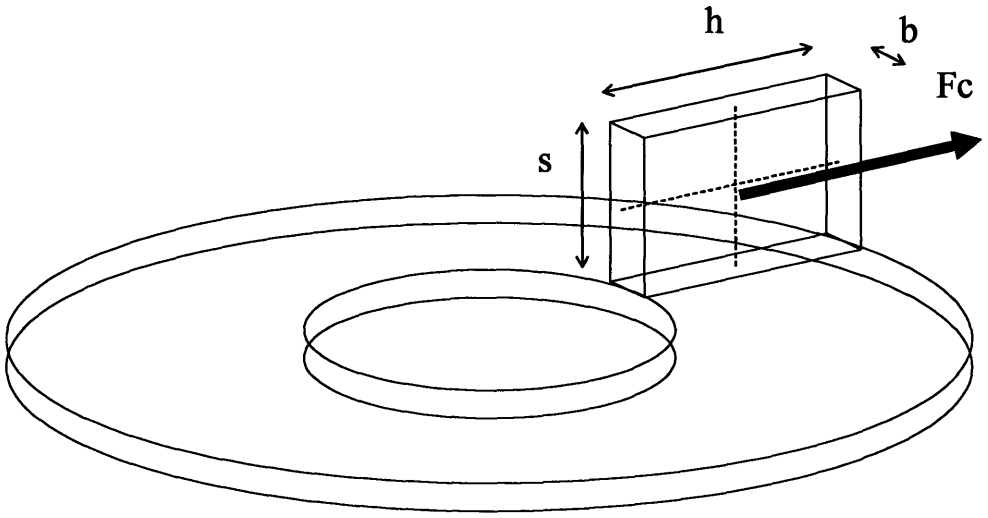

Figure 4.10 Turbine stress estimation

$$F_c = mr\omega^2 \tag{4.7}$$

$$M_b = F_c \frac{s}{2} \tag{4.8}$$

$$I = \frac{bh^3}{12} \tag{4.9}$$

$$\sigma_{\max} = \frac{M_b c}{I} \tag{4.10}$$

$$c = \frac{h}{2} \tag{4.11}$$

In the above equations m is the mass of the blade, M_b the bending moment, s the span of the blade, b the blade thickness, I the moment of inertia, and c the distance from the center to the leading or trailing edges.

The main assumptions used in the model to account for the turbine structural constraints are:

1. **The maximum stress in turbine is the centrifugal stress in the disk center and the blade bending stress due to centrifugal loads:** The turbine model can provide means to estimate the maximum allowable temperature if the stress is known. The stress estimates are valid for situations in which disk bending moment and blade shear stresses do not exceed centrifugal stresses.

2. **The turbine blades are simple parallelepipeds oriented radially:** This is a simplifying assumption for the purpose of estimating bending moments and stresses in the cantilevered blades and providing general guidelines. More accurate results can be obtained with 3-D FEM analysis.

3. **The turbine disk is a sandwich structures reinforced with SiC in the middle:** In reality the SiC is chemically deposited onto the silicon wafer only from one side [15]. This is assumed not to affect the strength of the structure.

4. **The maximum allowable temperature in the turbine for stresses below the values shown on figure 4.9 at temperature of 900C (1200K) can be extended to 1400K.** This is a reasonable assumption because the stress at 1200K is taken up predominantly in the SiC reinforcement in the structure. This assumption is based on recommendation by the materials and structures group [43].

4.9 MODEL FIDELITY

It is important to establish the level of confidence in the output of the integrated system model. To do this the assumptions in the model will be assessed and the sensitivity of the model to different parameters will be quantified. To obtain a reasonable estimate for the thermodynamic cycle performance it is necessary to have reasonable estimates for the turbomachinery performance (pressure ratio and efficiency), turbine inlet temperature, and the parasitic losses. Figure 4.11 is a sensitivity plot for the system power output with respect to the cycle parameters. The sensitivity study is performed for a case using baseline turbomachinery geometry and engine layout that generates about 10 Watts of net power.

The figure suggests that cycle output is most sensitive to turbomachinery efficiency. A 5% detriment in turbomachinery efficiency would lead to nearly 100% change in power output (it would consume the available power margin of the self-sustained engine). Thus an accurate prediction of turbomachinery performance is desirable (i.e. one should use the best available predictive model for turbomachinery performance). Turbomachinery performance is based on 3-D CFD solutions and as such it represents our best estimate. In the system model, reference compressor performance is used directly from CFD and is scaled to the exact operating condition of interest. For the turbine, the design code uses as input 3-D CFD turbine rotor efficiency and also 3-D CFD correlations for the dominant performance limiting mechanism such as turbine NGV loss and turbine exit loss.

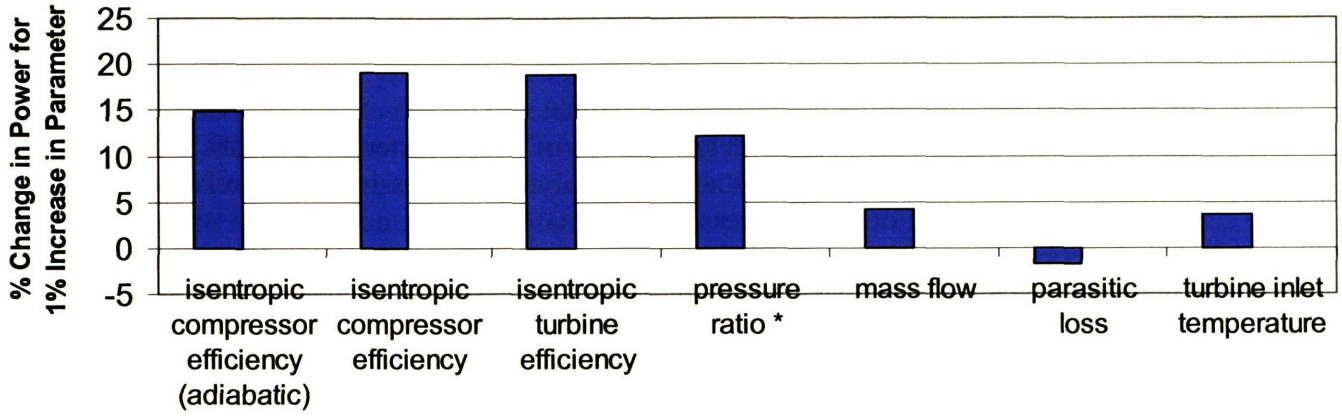

Figure 4.11 Sensitivity of system performance to cycle parameters about a selected operating point. * Pressure ratio is to the power of $\gamma/(\gamma-1)$.

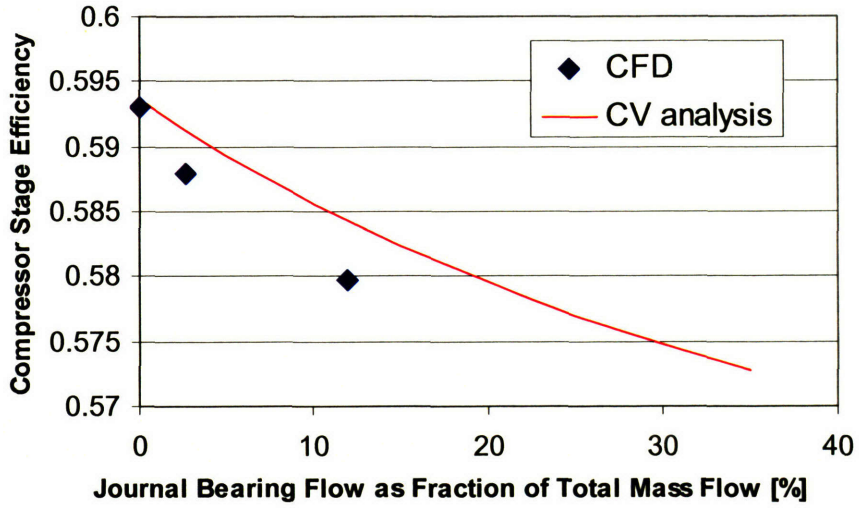

Figure 4.12 Compressor Performance as a Function of Journal Bearing Mass Flow

An issue of concern is the effect on turbomachinery performance from the interaction between journal bearing flows and compressor and turbine flows. This interaction is investigated and quantified with 3-D CFD (Fig 4.12) and the performance change is accounted for in the model. For the low levels of journal bearing flow (1-3% of total mass flow) at design condition the decrement in overall compressor efficiency is less than 0.5%. Figure 4.12 shows comparison between CFD results and a control volume analysis assuming that the journal flow mixes out completely with the main flow before it passes through the compressor diffuser. The reasonable agreement between CFD and model indicates that the effect of the journal flow is mainly to lower the stagnation pressure of the diffuser inlet flow.

Non-adiabatic compressor performance is obtained from the adiabatic performance and the level of heat addition using Gong's model [12]. The comparison to 3-D CFD solutions shows that compressor performance can be determined to within 5% if the exact level of heat addition is provided. To reduce uncertainty in the prediction of non-adiabatic compressor performance, a

non-adiabatic reference CFD solution is used in the system model. Such a compressor CFD solution still needs a good estimate of the total heat to compressor or compressor wall temperature.

The total heat transfer to the compressor is estimated with the engine heat transfer model. The heat transfer model is based on the determination of heat transfer coefficients from CFD for the more complicated situations. Well-established analytical expressions or correlations are used for the stationary channel flows. To assess the uncertainty in the model output associated with the determination of heat transfer coefficients and overall thermal resistance (factors such as surface roughness, aspect ratio of passages, turbulent regions in the flow, geometric approximations and flow averaging) the sensitivity of the output to the estimated thermal resistance is established. Figure 4.13 presents the sensitivity of cycle net power to the thermal resistance values for the heat paths in the engine.

The sensitivity to shaft resistance and journal gap resistance is not surprising since the largest heat flows to the compressor for the investigated case occur there. Since the shaft thermal resistance is the highest it determines the overall resistance between the compressor and turbine flows and this determines the most important heat flow. Figure 4.13 implies that the output power is also sensitive to the prediction of the overall resistance of the turbine NGV passages The sensitivity to NGV convective resistance is peculiar to cases with high turbine inlet temperature (1400-1700K). The combustor wall and NGV passages are assumed at 1100K. Therefore, the driving temperature difference is high and if the convective heat transfer coefficient changes, the heat transfer from the flow to the structure changes, and the effective turbine inlet temperature changes. This has a direct impact on the cycle output. Therefore it would be beneficial for cycles with high turbine inlet temperature to design the NGV passages with low wetted area so as to mitigate the sensitivity level.

It is important, however, to note that the sensitivity of the power output to the thermal resistance of the engine heat paths is not high. It would take an error of more than 60% in the resistance to which the system power output is most sensitive to consume the 10 Watts power margin for this case. Since the heat transfer coefficients for the turbomachinery flows are extracted from 3-D CFD solutions and the ones for stationary channels flows are based on well-established analytical expressions, as mentioned earlier, the error in the prediction is expected to be below that level.

Turbine inlet temperature is one of the inputs to the model and does not introduce any uncertainty. However, the value of turbine inlet temperature is directly related to the turbine structural integrity. It is important to account for the structural constraints for the turbine. As explained in section 4.7, the modeling of the turbine constraints may introduce uncertainty through the assumption that the dominant stress in the turbine is centrifugal stress. To compensate for this, a more accurate model can be developed or the safety factor for the turbine design may be increased accordingly. Currently the safety factor is set to 1.2, which provides 20% safety margin.

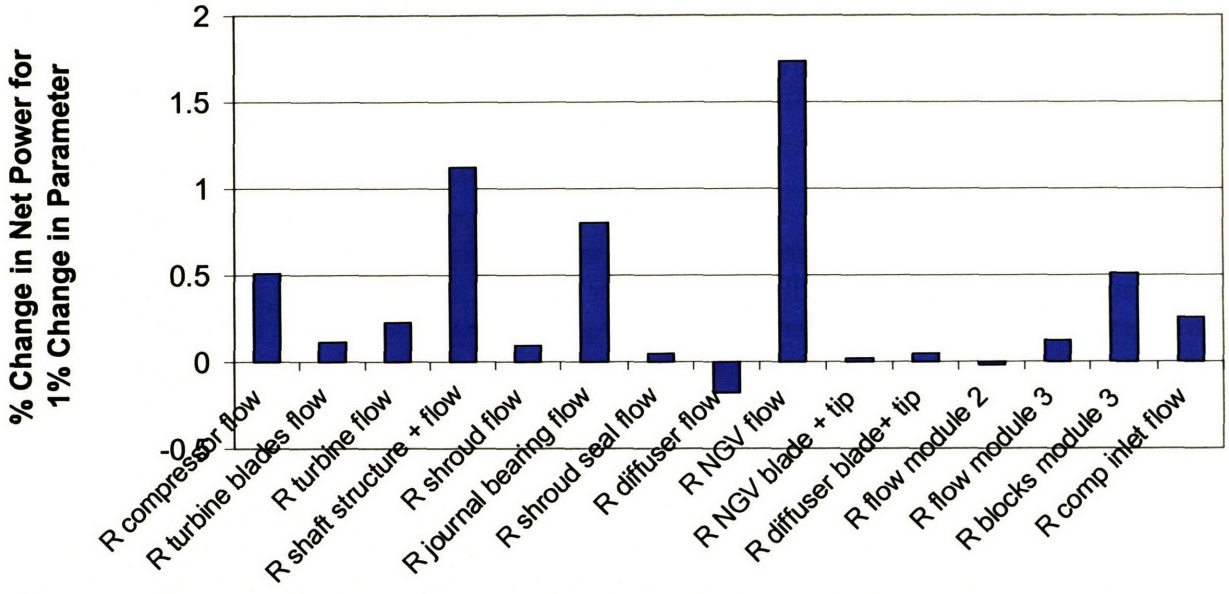

Figure 4.13 Sensitivity of system performance to prediction of thermal resistance in model about a selected operating point

In summary, the heat addition to compressor flow can be determined within the required accuracy (60% error). Turbomachinery performance can then be determined using the best predictive tools available (based on 3-D CFD solutions and correlations). Thus an adequate description of the cycle performance for preliminary design studies can be provided with the integrated system model.

CHAPTER 5

5 MICRO-ENGINE SYSTEM DESIGN STUDY

5.1 INTRODUCTION

This chapter summarizes the results from a micro-engine system design study based on the integrated system model described in Chapter 4. The system behavior is analyzed and key differences between conventional and micro-engine system selection are identified. Maps of the engine design space are generated to elucidate design trade-offs, identify design regions of interest and guide the selection of a self-sustained micro engine. Selected candidate designs for the "break-even" engine are proposed and discussed.

The key differences that are identified between conventional engine and micro-engine cycle selection are the following: Component performance changes for each set of cycle parameters. The additional strong coupling between components and system by heat transfer must be taken into account. The second is that for a conventional engine it is always desirable to increase the turbine inlet temperature [33] but not for a micro-engine. Third is that system performance changes appreciably with turbomachinery size because of the different scaling of heat transfer, parasitic power loss and mass flow with size for micro-engines.

5.2 SYSTEM DESIGN SPACE

The selected design space for investigation is summarized in Table 5.1. Table 5.1 lists the investigated design parameters, their range, and the selected step for each parameter to span the range. Turbine inlet temperature ratio (the ratio of turbine inlet temperature to ambient atmospheric temperature) is a design parameter governing cycle output. It is closely linked to turbine material properties and film cooling parameter as well as to isolation shaft thermal resistance. Compressor tip Mach number is directly related to compressor and system pressure ratio, to stresses in the rotor, and to the level of parasitic power losses. Turbine outer and inner radii (size) are linked to turbine performance for a given tip speed. The thermal resistance of the rotor isolation shaft (represented by the shaft to compressor disk area ratio) determines how much heat passes from the turbine to the compressor. The film cooling parameter also determines the level of heat transfer from turbine to compressor. This parameter controls the convective heat transfer coefficient between the turbine flow and the turbine disk thus mimicking film-cooling effectiveness. The strength of the turbine and its maximum allowable speed and temperature are determined by the fraction of silicone carbide (SiC) reinforcement in the turbine disk. The size of the turbomachinery and the engine determines the mass flow and actual power output of the machine and is directly linked to manufacturing capability. It also affects system performance. The integrated system model is implemented to map the performance of the micro-engine system for the range of parameters described in Table 5.1.

Table 5.1 Investigated micro-engine system design variables and parameters

	DESIGN VARIABLES AND PARAMETERS	MIN	STEP	MAX
1	Turbine Inlet Temperature Ratio (Tt4/Tt0)	3.17 (950 K)	0.33 (100 K)	5.5 (1650 K)
2	Compressor Tip Mach Number (Mtip)	1.15 (400m/s)	0.072 (25 m/s)	1.58 (550 m/s)
3	Turbine Size (Rout/Rout comp)	0.875	0.05	1.125
4	Shaft Thermal Resistance (Ashaft/Acomp)	0.001	varying	1
5	SiC Thickness as Fraction of Turbine Disk	0	0.1	0.3
6	Turbomachinery and Engine Scale	0.5	0.5	2
7	Film-cooling Parameter	0	1	1

5.3 SYSTEM BEHAVIOR

The results obtained with the system model represent 37,632 different micro engine designs and serve the purpose of mapping the system design space. The generated design maps provide a mean to set minimum technology level requirements for the development of a self-sustained engine. Some of the observed trends in the system behavior are as expected and similar to the ones in large engines. Other trends are specific to micro-engines and the focus in this chapter will be on the latter.

5.3.1 SYSTEM BEHAVIOR WITH CHANGES IN TECHNOLOGY LEVELS

Contour maps of engine power output are generated to bring out the effects of turbomachinery size, film cooling effectiveness, levels of SiC in the turbine disk and isolation shaft resistance on engine performance (Fig 5.1 and 5.2). Each point on the contour plots represents the engine design for the indicated technology levels with peak performance for the investigated range in compressor tip speed, turbine size, and turbine inlet temperature. Each combination of these three variables represents a different cycle since they control system pressure ratio and turbine inlet temperature. The contour plots, therefore, indicate how the performance of the best possible cycle changes for each technology level. The material strength of the turbine, the resistance of the thermal isolation shaft between the compressor and turbine and the turbine inlet temperature are closely related. They govern the heat flows through the engine and set the temperature distributions.

Before discussing the observations and trends it is necessary to provide some information about the normalization used on the maps. The reference size used to normalize turbomachinery size is 400 μm blade height for the compressor and 500 μm blade height for the turbine. The outer radius of the reference impeller is 4 mm. Turbine size for peak system efficiency is selected for each set of design parameters. The reference area to normalize the thermal isolation shaft cross sectional area is compressor disk area. The shaft is selected to be of particular fixed length and conductivity so that the thermal resistance is a function of cross sectional area only. The level of SiC reinforcement in the turbine disk is given as fraction of the turbine disk thickness. 30% SiC represents a turbine disk with 30% SiC and 70% Si thickness. Film cooling "ON" means no heat

transfer through the turbine disk (only through the turbine blades) and "OFF" represents no film cooling at all. Reference adiabatic turbomachinery performance is obtained from CFD as described in Chapter 4 and is scaled for the conditions of interest.

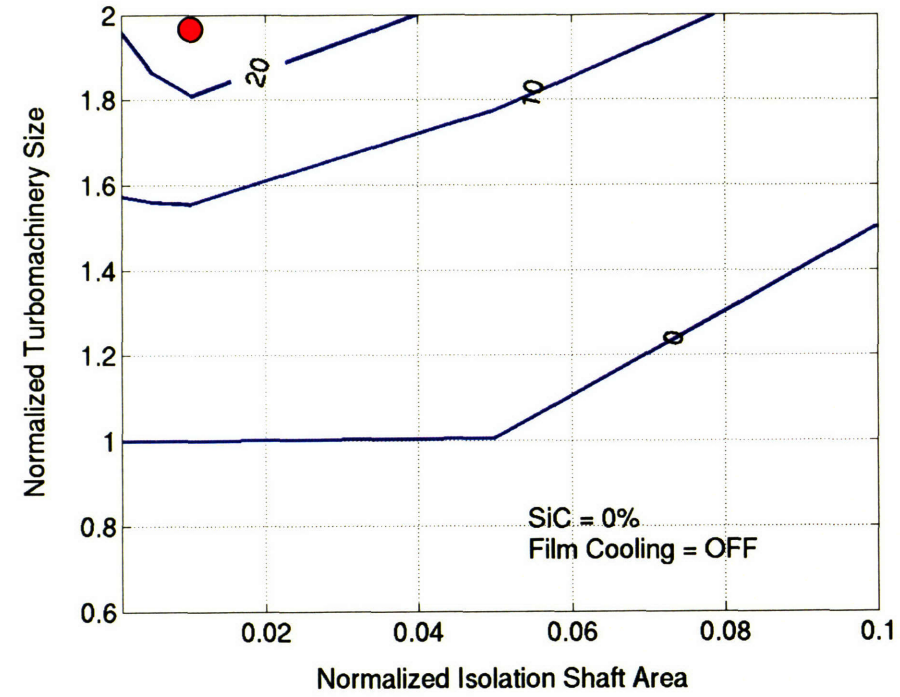

(a)

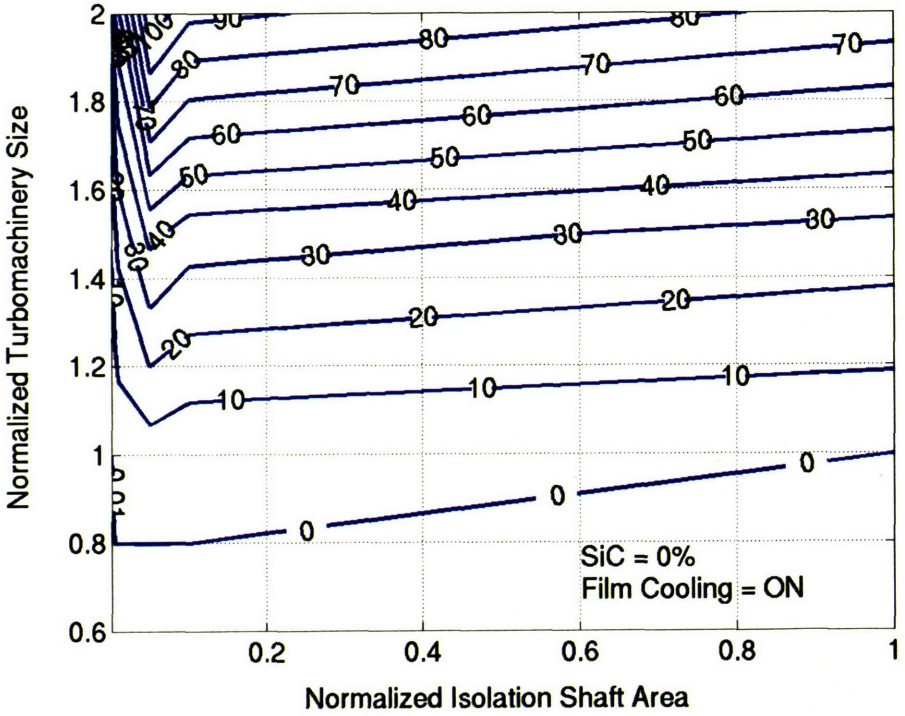

(b)

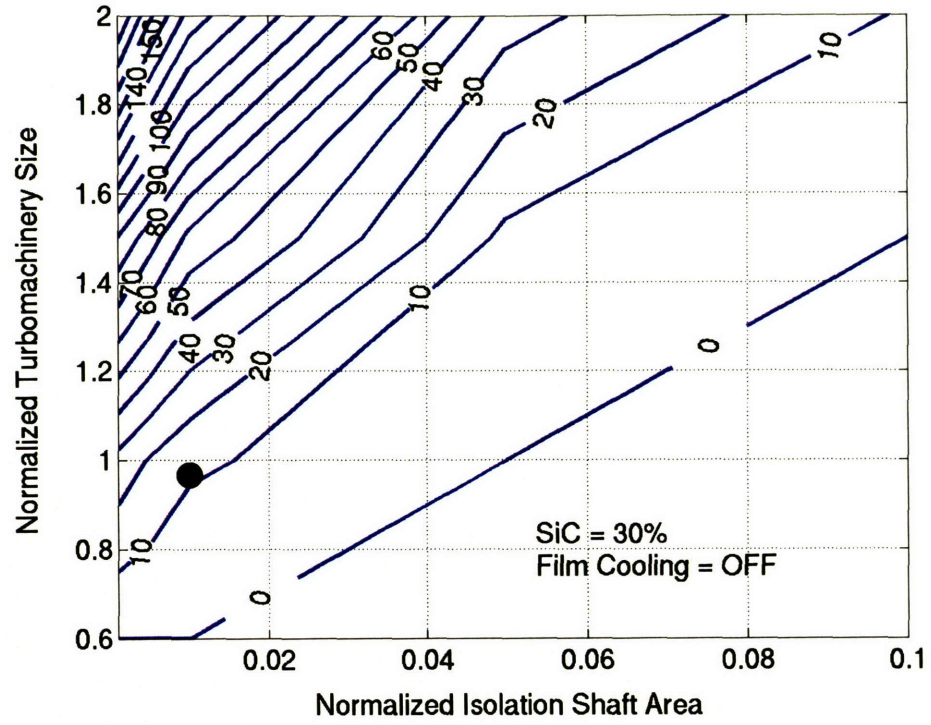

(c)

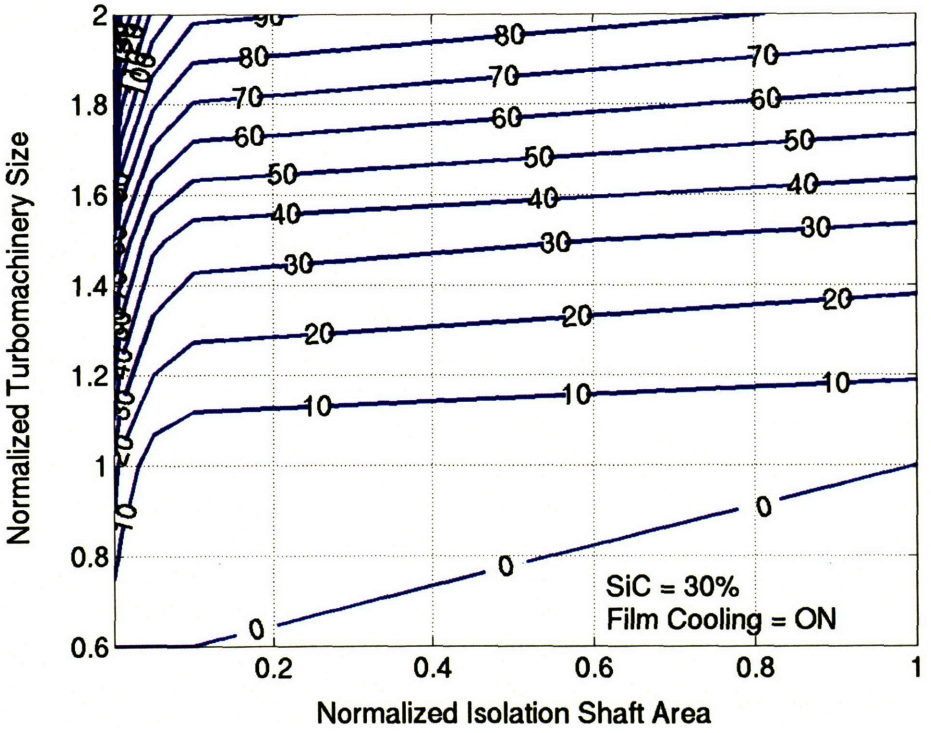

(d)

Figure 5.1 Engine net shaft power contours in watts for different technology levels. NOTE: The map represents cycles optimized for maximum net power over the range of investigated compressor tip mach number, turbine size, and turbine inlet temperature. Each map is presented for a region of interest (axis not the same for all figures). Red and black circles represent designs selected for further investigation.

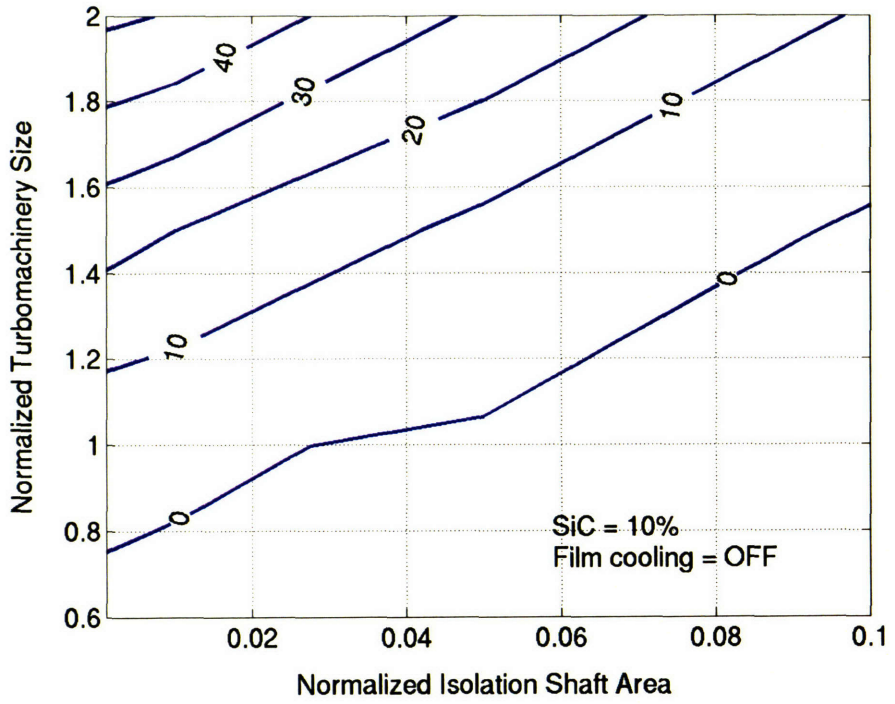

(a)

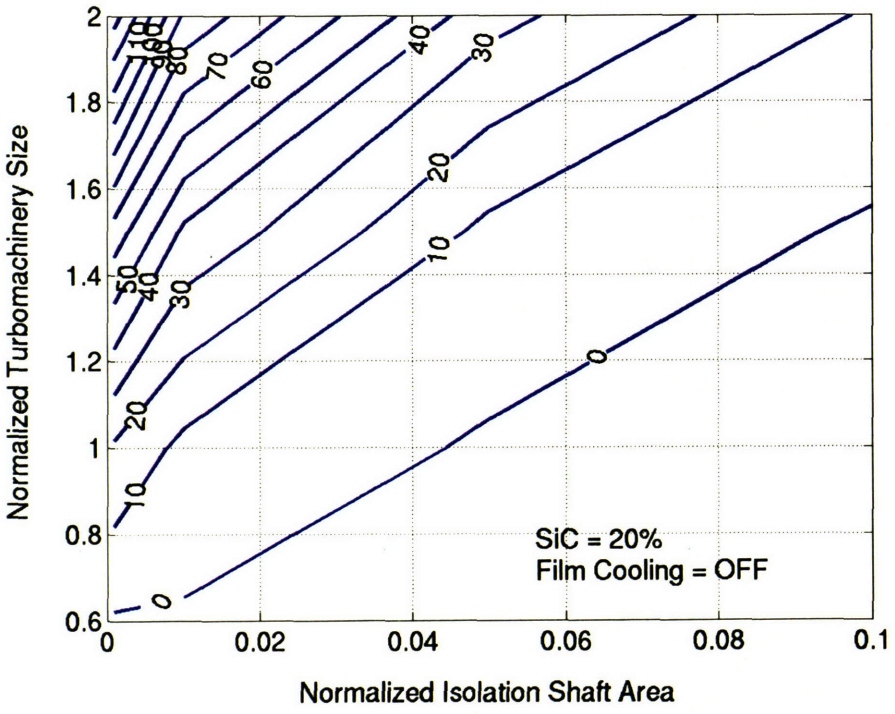

(b)

Figure 5.2 Engine net shaft power contours in watts for different SiC technology levels without turbine disk film cooling. NOTE: The map represents cycles optimized for maximum net power over the range of investigated compressor tip mach number, turbine size, and turbine inlet temperature.

Figures 5.1 and 5.2 present engine net power contours as function of turbomachinery size and rotor shaft cross sectional area, which determines shaft resistance. Cases with varying levels of SiC reinforcement and film cooling are shown. The smoothness of the contours can be improved by increasing the number of investigated designs, however, this does not alter the trends and conclusions.

In Figure 5.1 a black circle indicates engine design A and a red circle indicates engine design B. These are two engine designs selected for further investigation and their choice will be discussed in section 5.4. Designs A and B indicate engine system design options and should not be confused with impeller designs A and B from Chapter 3.

A direct conclusion from Figure 5.1 (a) is that a self-sustained micro-engine CANNOT be designed using the current reference turbomachinery size, performance and geometry without some SiC in the turbine or some film cooling. The minimum required turbomachinery size to produce about 10 Watts net power is 1.5-1.6 times the current size. The minimum level of SiC reinforcement in the turbine is estimated to be 30% of turbine thickness from Figure 5.1 (c). Turbine disk film cooling needs to be such that the turbine disk is nearly adiabatic to achieve the same result based on Figure 5.1 (b). A "break even" engine can also be designed with a combination of the above-mentioned changes so that the requirements on each technology are reduced. These requirements can be determined from the performance maps. For each of these required changes the thermal isolation shaft area is assumed to be 1% of compressor area (due to current structural and micro-fabrication limitations it is not reasonable to assume smaller shaft). These results determine the minimum technology requirements for a self-sustained micro-engine.

It is also useful to determine the best possible engine for the range of investigated design parameters. This best engine represents the performance of a future generation micro-engine with nearly adiabatic turbomachinery (by using 0.1% shaft area or 100% effective film cooling of the turbine disk or a combination), 30% SiC reinforcement in the turbine disk, and double the current turbomachinery size. It can produce on the order of 200 Watts with chemical to shaft mechanical conversion efficiency of about 6%. Such a performance level combined with an efficient micro generator can meet the criteria for a competitive portable power generation device.

The next important observation is related to shaft thermal resistance and turbine inlet temperature. Figures 5.1-5.2 suggest that the behavior of the all silicon engine with changes in shaft thermal resistance is different from the behavior of the engine with some SiC turbine reinforcement. For the all silicon cases there is an optimal thermal resistance for the isolation shaft near normalized shaft area of 0.01. The thermal resistance of the isolation shaft for the all silicon engine is directly related to the temperature in the turbine structure and also to the turbine inlet temperature. An increase in shaft thermal resistance is accompanied by a decrease in turbine inlet temperature to keep the turbine structural temperature fixed below the fracture limit. Therefore, an optimal turbine inlet temperature associated with peak engine power output exists for the silicon engine. In some regions of the design space an increase in turbine inlet temperature would be beneficial for system performance and in other regions a decrease. This is in contrast to conventional engines for which an increase in turbine inlet temperature is always desired but is limited by material properties. A detailed discussion of this observation will be given in the next section (5.3.2). The thermal resistance of the engine with SiC reinforced turbine is not directly linked to the turbine inlet temperature because the turbine does not operate

near its structural limit (turbine temperature is limited by combustor capabilities). Beneficial increase in shaft resistance is therefore possible without reduction in turbine inlet temperature.

Another observation is that system performance improves steadily with increasing turbomachinery size. This improvement with size serves to mitigate the requirements on the other technologies. As discussed before, if the current size of the turbomachinery is increased by 60% the engine would no longer need other advanced technologies like SiC or film cooling to break even. The improving system performance with size is elaborated further in section 5.3.3.

The improvement of system performance with SiC reinforcement of the turbine is related to the possible increase in turbine temperature and/or tip speed and/or reduction in heat transfer to compressor by increasing shaft resistance. These changes are in turn related to the cycle parameters – turbine inlet temperature, overall pressure ratio, compressor and turbine performance. The improvement in system performance with film cooling is similarly related to cycle output and to heat transfer in the engine. Any increase in isolation shaft resistance is accompanied by an increase in turbine temperature and the requirement for stronger materials or lower turbine inlet temperature. If both turbine disk and turbine blades can be protected and isolated from the hot flow by a film cooling layer these requirements are removed or reduced. Therefore, it would be beneficial in the future to develop film-cooling technology for the micro-engine just as it is important for conventional large engines. Currently such technology does not exist for micro-engines.

The following sections elaborate further the observed important trends.

5.3.2 TURBINE INLET TEMPERATURE REGIMES FOR NON-ADIABATIC TURBOMACHINERY ENGINE

For micro-engines, an increase in turbine inlet temperature does not necessarily lead to improved system performance. It was observed in the previous section that for different cases the trends are different. It is not obvious at all what should be the proper change in turbine inlet temperature and isolation shaft resistance for a given design. In some of the previous work on the micro-engine system, recommendations from sensitivity studies to both increase [22,24] and decrease [23] turbine inlet temperature to improve system performance were drawn. This section addresses this apparently confusing issue and provides insight into the micro-engine system behavior with turbine inlet temperature.

The answer to the question above is that there are two possible regimes of operation for micro engines. A regime in which an increase in turbine inlet temperature would result in improved performance and another one in which such an increase would lead to deterioration in system performance. The physical reason for the existence of two regimes is related to two competing effects. One is that, just like in a conventional engine, as turbine inlet temperature is increased, the thermodynamic cycle is modified in such a way as to increase specific power and efficiency. The other competing effect is that as turbine inlet temperature is increased, the heat transfer between turbine and compressor increases, and this leads to deterioration in compressor performance thus reducing system performance. Therefore, the relative importance of these two effects determines the regime of operation for the engine and the desired direction of change for the turbine inlet temperature.

To delineate the two regimes an approximate criterion can be developed to describe the interaction between the two effects. If the specific power output of the system is of interest it is possible to investigate the parameters controlling the turbine inlet temperature regime. Understanding the two regimes and the governing parameters is necessary in order to select not only a proper thermodynamic cycle but also to select a thermal isolation shaft between the turbine and the compressor.

The specific power output of an engine of given technological level and size (adiabatic efficiency and pressure ratio of both the compressor and the turbine), depends only on the selection of turbine inlet temperature, and the value of the heat addition parameter. This information is sufficient to determine the thermodynamic cycle and its output. For the purpose of comparing the two competing effects the changes in engine performance with turbine inlet temperature and heat addition parameter are investigated. Every engine of the given technological level can be represented as a point in the selected parameter space and specific power contour map can be generated to indicate the changes in performance with turbine inlet temperature and heat parameter.

These specific power contours (engine net power divided by engine mass flow) are indicated with blue lines on Fig. 5.3. The contour map delineates the direction (as indicated by the blue arrow) of improving specific power, which is normal to the contours of constant power. An engine operating with low heat parameter and high T_{T4} would be much better (lower right corner) than an engine operating with high heat parameter and low T_{T4} (upper left corner). Turbine inlet temperature is normalized on the plot with engine inlet temperature T_{T0}. A specific engine will move, however, along a given curve on this map if its design turbine inlet temperature is changed. For this engine, a given change in turbine inlet temperature would lead to a corresponding change in the heat parameter. This fixes the specific (q^*, T_{T4}) curve on the map in the selected space for a family of engine designs differing only in T_{T4} (red lines on Fig 5.3). It becomes clear from Figure 5.3 that for some engines it would be beneficial to increase turbine inlet temperature and not for other.

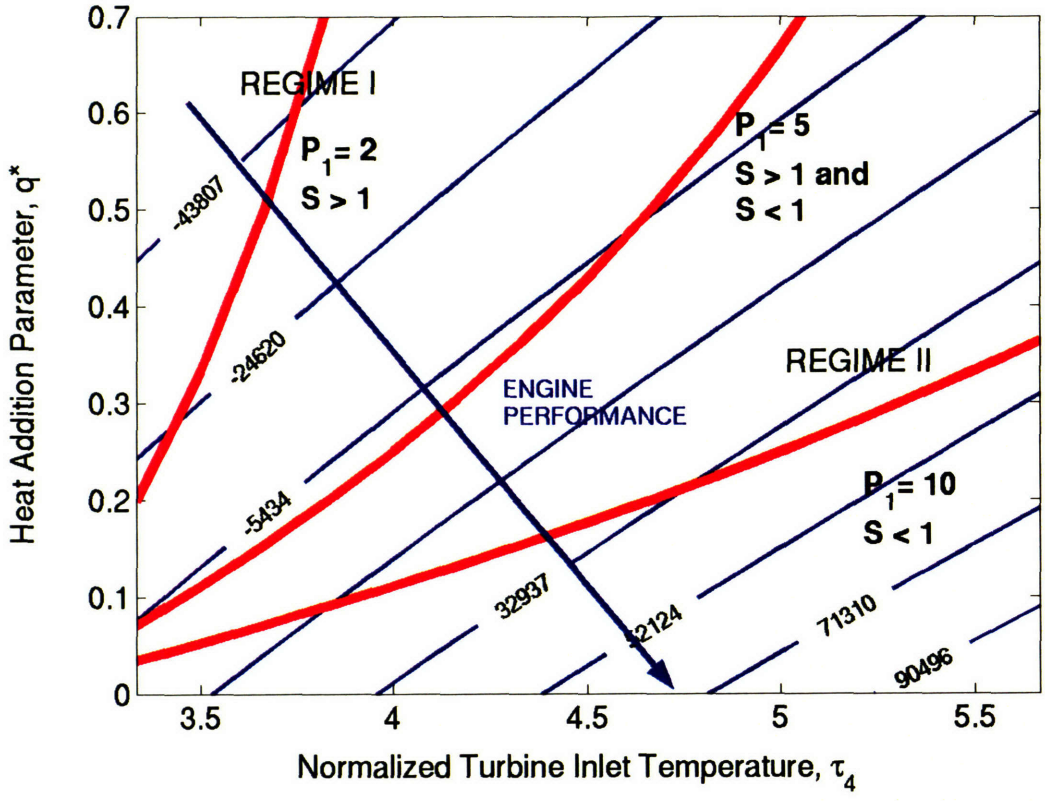

Figure 5.3 Engine specific power (J/kg). Effect of governing parameter P_1 on turbine inlet temperature regime. Red lines represent different values of P_1 – different engine families. Constant specific power contours are in blue. Turbine temperature at material limit.

It can be shown approximately that the position and slope of this engine family curve would be a function of some representative thermal resistance between the flows in the turbine and the compressor, the mass flow of the engine, and the turbine inlet temperature. The first step is the definition of heat addition parameter given in Eq. 5.1-5.3. The heat from the turbine to the compressor is approximated as the most general driving temperature difference (T_{T4}-T_{T0}) divided by some representative rotor thermal resistance as shown in Eq. 5.1. In this form the definition of heat addition parameter q^* provides a link between q^* and two non-dimensional parameters. These parameters are P_1 and τ_4 (governed by T_{T4}) given in Eq. 5.6-5.7. Therefore, the specific (q^*,T_{T4}) engine family curve is defined by the parameter P_1.

A given engine design can be represented by a point on the curve defined by P_1. Changes in τ_4 (and corresponding changes in rotor thermal resistance if turbine temperature is fixed) would move the engine design along the curve defined by P_1 (the red curves on Fig 5.1). The expression for the curve is differentiated to obtain the desired slope as shown in Eq. 5.8.

$$Q_{rotor} = \frac{(T_{T4} - T_{T0})}{R_{rotor}} \tag{5.1}$$

$$H = Cp\dot{m}T_{T0} \tag{5.2}$$

$$q^* = \frac{Q_{rotor}}{H} = \frac{(T_{T4} - T_{T0})}{R_{rotor} Cp \dot{m} T_{T0}} \tag{5.3}$$

$$\dot{m} = \frac{\dot{m}_{ad}}{1+q^*} \tag{5.4}$$

$$q^* = \left(\frac{R_{rotor} Cp \dot{m}_{ad}}{\left(\frac{T_{T4}}{T_{T0}} - 1\right)} - 1 \right)^{-1} = \left(\frac{P_1}{\left(\frac{T_{T4}}{T_{T0}} - 1\right)} - 1 \right)^{-1} = \left(\frac{P_1}{(\tau_4 - 1)} - 1 \right)^{-1} \tag{5.5}$$

$$P_1 = R_{rotor} Cp \dot{m}_{ad} = \frac{\Delta Q_{flow}}{\Delta Q_{rotor}} = \frac{mCp\Delta T_{T4}}{\frac{\Delta T_{T4}}{R_{rotor}}} \tag{5.6}$$

$$\tau_4 = \frac{T_{T4}}{T_{T0}} \tag{5.7}$$

$$\left.\frac{\partial q^*}{\partial \tau_4}\right|_{P1=const} = \frac{P_1}{(P_1 - (\tau_4 - 1))^2} = f(P_1, \tau_4) = slope1 \tag{5.8}$$

$$\left.\frac{\partial q^*}{\partial \tau_4}\right|_{\frac{W}{\dot{m}}=const} = g(\eta_{c\_ad}, \eta_{t\_ad}, \pi_{c\_ad}) = slope2 \tag{5.9}$$

$$S = \frac{slope1}{slope2} \tag{5.10}$$

$S > 1$ Regime I
$S < 1$ Regime II

The answer to the question about increasing or decreasing turbine inlet temperature to improve engine specific power is given by the slope (of the red lines on Fig. 5.3) of the engine heat parameter-turbine inlet temperature curve (defined by P_1, and τ_4 for a family of engines) and the slope of the specific power contours (blue lines) for this engine technology (defined by the adiabatic turbomachinery performance and calculated by cycle analysis) at a given point. The criterion can be formulated in terms of the ratio of the slope of the engine (q^*, T_{T4}) curve at the point of interest to the slope of the specific power contour for the engine technology at this same point as shown in Eq. 5.8-5.10. This ratio is denoted with S.

If S is smaller than one then it is beneficial to increase turbine inlet temperature, as is the case for the engine family represented by the red curve on Fig. 5.3 with P_1=10. If S is greater than one, it

is beneficial to reduce turbine inlet temperature (red curve with P_1=2). S equal to one represents the condition for maximum net power. Such optimal condition can be seen for the engine family represented by the red curve with $P_1 = 5$.

If S is smaller than one (S<1) it means that the effect of increasing the heat parameter on the cycle output is less important than the effect of increasing the turbine inlet temperature of the cycle and the consequence is an improved cycle output (Regime II). For S greater than one (S >1) the opposite is true and it is desirable to decrease turbine inlet temperature (Regime I).

Figure 5.3 describes the behavior of a system of given technology level in terms of P_1 and τ_4. As P_1 increases the slope of the engine family curve decreases and the engine design is moving from Regime I (S>1) to Regime II (S<1). As P_1 increases the mass flow of the engine and the rotor thermal resistance increase and therefore the effect of the heat parameter becomes less important. Hence the improvement in power output with increasing turbine inlet temperature characteristic of Regime II.

At the same time, as τ_4 increases for a given value of P_1, the slope of the engine family curve increases thus moving the design towards Regime I. If changes in T_{T4} did not affect compressor mass flow then the slope of the engine family curve would be invariant with T_{T4} because heat transfer scales linearly with T_{T4}. However, because compressor mass flow decreases with increasing T_{T4}, the increase in q* for the same increase in T_{T4} is larger at higher T_{T4}. This explains the regime change for engines of the same P_1.

The physical interpretation is that for a given change in T_{T4}, P_1 compares the heat required to produce this change in T_{T4} to the additional heat that would pass through the turbine to the compressor. This comparison is delineated in Eq 5.6. If a large amount of heat can be put into the flow (by the combustor) increasing T_{T4} without passing a large amount of heat to the compressor (P_1 large) then it would be beneficial to increase T_{T4} and vice versa. P_1 is similar to the previously defined heat addition parameter but it provides additional information. It was established that P_1, q^* and τ_4 could be linked directly as shown in Eq 5.5. q^* represents the effect of heat transfer to compressor on compressor flow temperature. P_1 represents the effect of increasing turbine inlet temperature on heat transfer to compressor. The established link between the two relates the increase in turbine inlet temperature to the increase in compressor inlet temperature (and thus on compressor performance) as function of shaft resistance and engine mass flow. The controlling parameter P_1 can be linked directly to engine design parameters. Rotor thermal resistance is related to wetted area and shaft design, mass flow is related to operating speed, component geometry, and size.

Often the engine operates with temperature of the turbine structure near the limit (all silicon engine). Then the effect of increasing T_{T4} on compressor performance would be more dramatic because there would necessarily be a reduction in rotor shaft resistance to keep turbine temperature fixed and more heat would pass to the compressor. For this situation the heat transfer to the compressor can be defined in terms of a more relevant temperature difference involving T_{T4} and $T_{turbine\_max}$ (the limiting temperature of the turbine which remains fixed) instead of T_{T0}. The relevant resistance then would be the convective thermal resistance between the turbine flow and the turbine structure. Using this definition for the heat flow the same arguments apply and the same two regimes can be defined. Figures 5.3 and 5.5 (for the all-silicon engine B) represent cases with fixed turbine structural temperature.

The regimes of design selections A and B (defined in sections 5.3.1 and 5.4) are indicated on Figures 5.4 and 5.5. Design A operates away from the turbine temperature limit and an increase in turbine inlet temperature is not associated with significant increase in heat transfer because the shaft resistance can remain fixed. The design operates in Regime II. The beneficial increase in turbine inlet temperature is limited, however, by the maximum investigated combustor exit temperature.

Design B in contrast, demonstrates optimal performance with turbine inlet temperature. As the resistance of the rotor shaft increases and the turbine inlet temperature is reduced to keep the turbine below its limiting temperature (for this design the turbine is not reinforced with SiC) the Regime changes from I to II. At very high shaft resistance and low turbine inlet temperatures the engine behaves like a conventional engine and increase in T_{T4} is desirable. As the shaft resistance is reduced the heat transfer effect increases in importance and gradually takes over. The optimal turbine inlet temperature for the all silicon design B is around 1150 K.

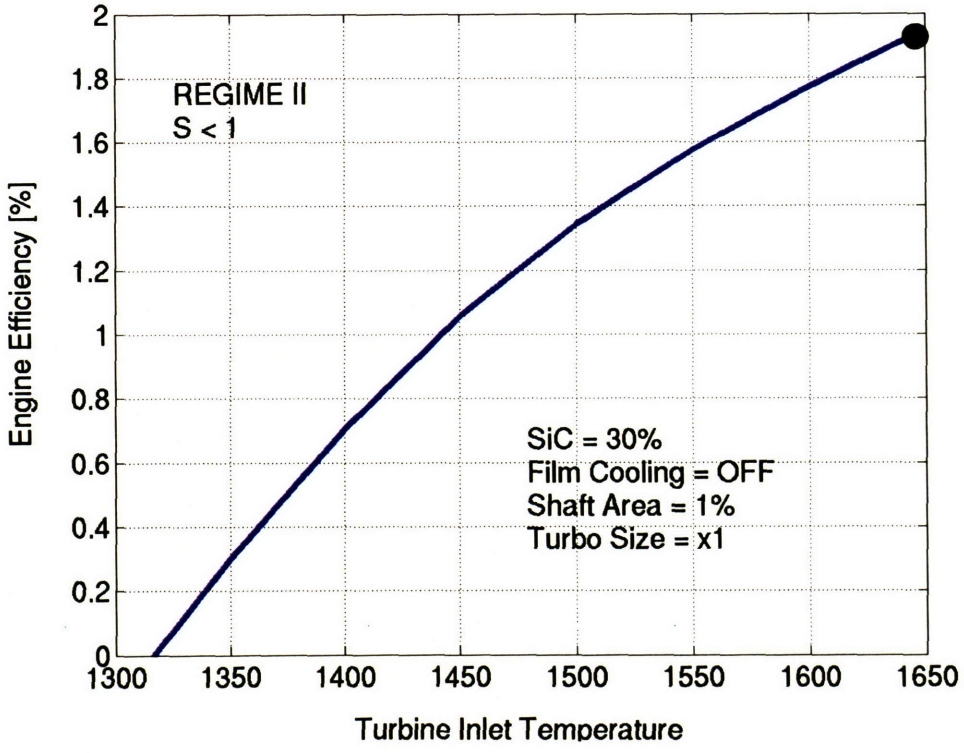

Figure 5.4 Efficiency of engine family A as a function of turbine inlet temperature. Black circle indicates selected engine design A.

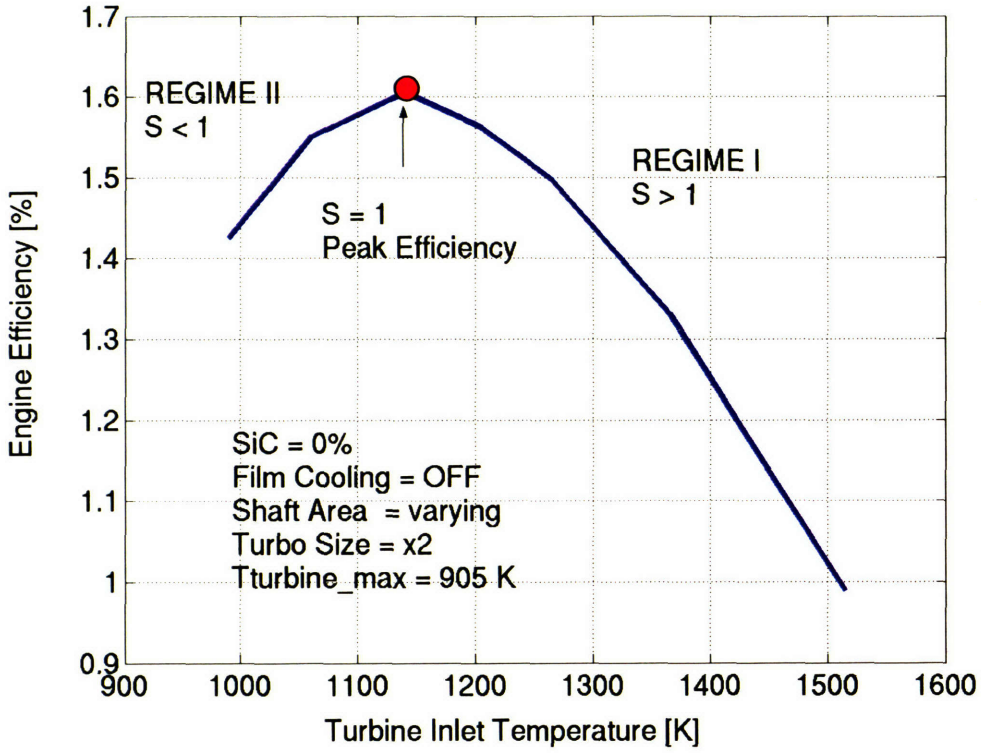

Figure 5.5 Efficiency of engine family B as a function of turbine inlet temperature. Red circle indicates selected engine design B.

5.3.3 EFFECT OF TURBOMACHINERY AND ENGINE SIZE ON SYSTEM PERFORMANCE

In section 5.3.1 it was observed that system performance improves continuously with increasing turbomachinery size. The reasons for this improvement are several and are investigated in a case study by doubling the turbomachinery size of engine A. First, as turbomachinery is scaled up two times in size, mass flow increases approximately four times. The heat through the turbine scales similarly (with area) and also increases about four times (if isolation shaft is scaled in the same way). However, the heat that passes to the compressor through the engine casing and static structure, which is almost half the total heat, scales differently. The heat through the casing remains approximately the same although the whole engine is about two times bigger (it actually decreases by 1.4%). Therefore, the total heat to the compressor increases slower than the mass flow of the engine and the heat addition parameter is correspondingly reduced (30%). This reduction in heat parameter leads to improved performance.

The reason why the heat through the casing remains approximately the same is because the conduction resistance of the casing is predominantly determined by the resistance of the top and bottom wafers, which have ring like shapes. Their thickness remains the same when the turbomachinery is scaled up. From the equation for conduction thermal resistance for cylindrical shell (Eq. 3.30 in Appendix A [39]) it follows that the thermal resistance is a function of the

outer-to-inner radius ratio of the shell (the wafer). As the engine is scaled up this ratio remains the same, as does the thickness of the wafer and its thermal conductivity. Therefore, the resistance of the casing and the total heat flow for given temperature difference through the casing remain approximately the same. The net effect is a design with improved system performance.

The heat transfer through the sidewalls of the compressor and turbine disks also scales with area and for this reason only doubles because the thickness of the turbine and compressor disks is not scaled. Therefore, one of the largest heat transfers, through the compressor journal bearing, also scales favorably with increasing size and leads to system performance improvement.

Another effect is related to the heat transfer in the turbine NGVs. The integrated system model uses a conservative assumption that all heat lost from the flow through the NGV passages is lost near the NGV entrance and effectively reduces the turbine inlet temperature. As the turbomachinery size is scaled up, the NGV flow loses less heat and the effective turbine inlet temperature increases thus increasing the power output (in the case study the change in effective turbine inlet temperature decreases 44% after doubling the size). The reason is that the NGV blade chord can be chosen to remain fixed. This leads to an increase in blade count to keep the same solidity at the larger radial position of the blades. However, the hub and casing areas only increase by an approximate factor of 2 and most of the heat transfer occurs through these two areas. Again the mass flow increases four times when the turbomachinery size is doubled and thus the detrimental effect of heat loss on effective turbine inlet temperature decreases with increasing rotor size.

A reason for improving performance with increasing turbomachinery size is related to the parasitic power losses. These losses depend on the rotor speed, the wetted area, and the gap between the rotating and stationary parts. The tip speed of the rotor remains the same after the scaling. However, the area of the journal bearings only increases with a factor of 2 because the disk thickness remains the same and it is assumed that the required gap remains the same. Therefore the power loss doubles while the net engine work increases four times with mass flow. The area of the shroud seal also only increases two times because the required length of the seal is independent of scale and depends only on the pressure difference across the seal. As the turbomachinery size is increased with a factor of 2 in the case study the parasitic power loss as a fraction of available power (the difference between turbine output power and compressor consumed power) decreases 54%.

Another factor responsible for the improvement in system performance is the improvement in adiabatic turbomachinery performance with increasing size. This is because the Reynolds number for the flow passages increases. This effect is not directly included in the system model. The performance for the selected scaled design is later adjusted by using CFD solutions for the larger turbomachinery. The adiabatic compressor efficiency improves by 2 percentage points.

The combination of all these important effects leads to appreciable improvement in system performance. For example, if the turbomachinery of the investigated engine is scaled up two times, the system efficiency increases 2.5 times and the actual power output increases 10 times. This can be explained with the 30% decrease in heat addition parameter and the 54% decrease in the parasitic power loss as a fraction of available power (the difference between turbine output power and compressor consumed power). This is an indication that the current micro-engine

design is in a region of the design space where bigger engine is better for system performance. A study of the effect of engine size on micro-engine performance is presented in Appendix B.

5.3.4 SYSTEM RESPONSE TO COMPRESSOR TIP SPEED, TURBINE SIZE AND TURBINE INLET TEMPERATURE CHANGE

To investigate the system behavior with changes in the cycle parameters, selected candidate designs are studied. As explained in section 5.3.1 these two designs are optimized for the three parameters of interest, namely compressor tips speed, turbine size and turbine inlet temperature. System efficiency contour maps are generated near the optimum to elucidate the system behavior with changes in the three parameters.

Figure 5.6 presents engine efficiency contours as a function of design parameters for engine A. Figure 5.6 (a) presents efficiency as function of compressor tip mach number (pressure ratio) and turbine size. Figure 5.6 (b) presents efficiency as function of compressor tip mach number and turbine inlet temperature and (c) presents efficiency as function of turbine inlet temperature and turbine size. Figure 5.7 provides the same information for design B.

The red lines, indicating turbine fracture, show for both designs the expected trade-off between rotor speed (pressure ratio), turbine size (turbine efficiency), and turbine inlet temperature (cycle output, compressor efficiency). The trade-off between rotor speed and turbine size can be seen on Figures 5.6 (a) and 5.7 (a). The trade-off between rotor speed and turbine inlet temperature can be seen on Figures 5.6 (b) and 5.7 (b). The trade-off between turbine inlet temperature and turbine size can be seen on Figures 5.6 (c) and 5.7 (c). All of these parameters affect maximum turbine stress as described in Chapter 4, which is constrained by material properties.

Compressor tip speed is directly related to system pressure ratio and parasitic power losses and an optimal speed for peak efficiency can be noted for each case. For a conventional engine the optimal pressure ratio is determined by the component efficiencies for given turbine inlet temperature and increases with improving component performance and with increasing turbine inlet temperature. For the micro-engine the pressure ratio associated with peak system efficiency is also a function of an additional parameter. This parameter is the parasitic power loss from the gas bearings, compressor shroud and seal, and isolation shaft drag. Parasitic power loss is important because it is comparable to the power output of the micro-engine (in fact it is larger). The scaling of the different parasitic power losses with speed is discussed in Appendix A.

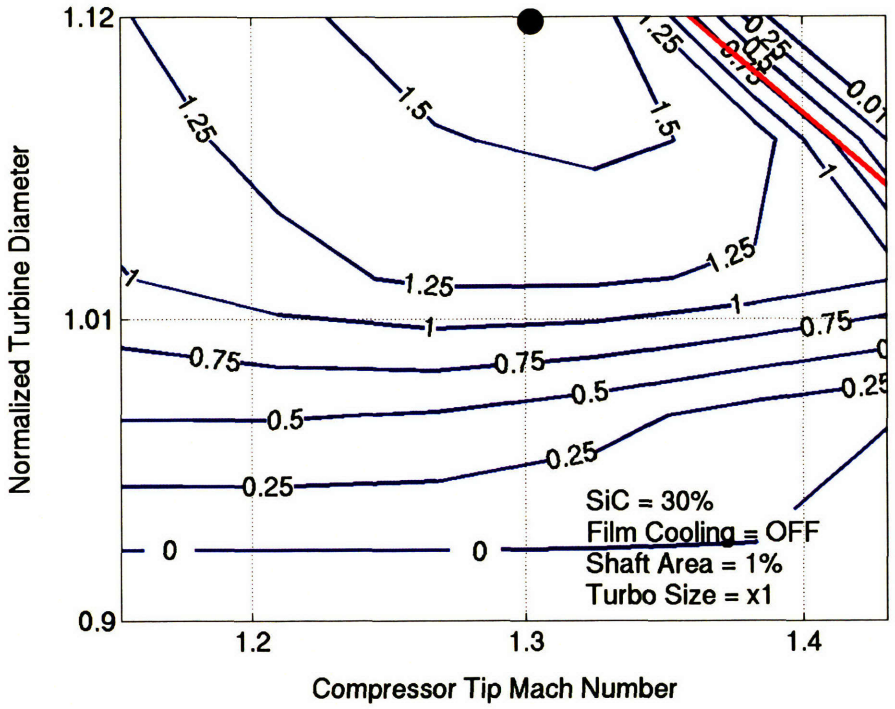
Normalized Turbine Diameter
Compressor Tip Mach Number
1.12
1.01
0.9
1.2
1.3
1.4
SiC = 30%
Film Cooling = OFF
Shaft Area = 1%
Turbo Size = x1

(a)

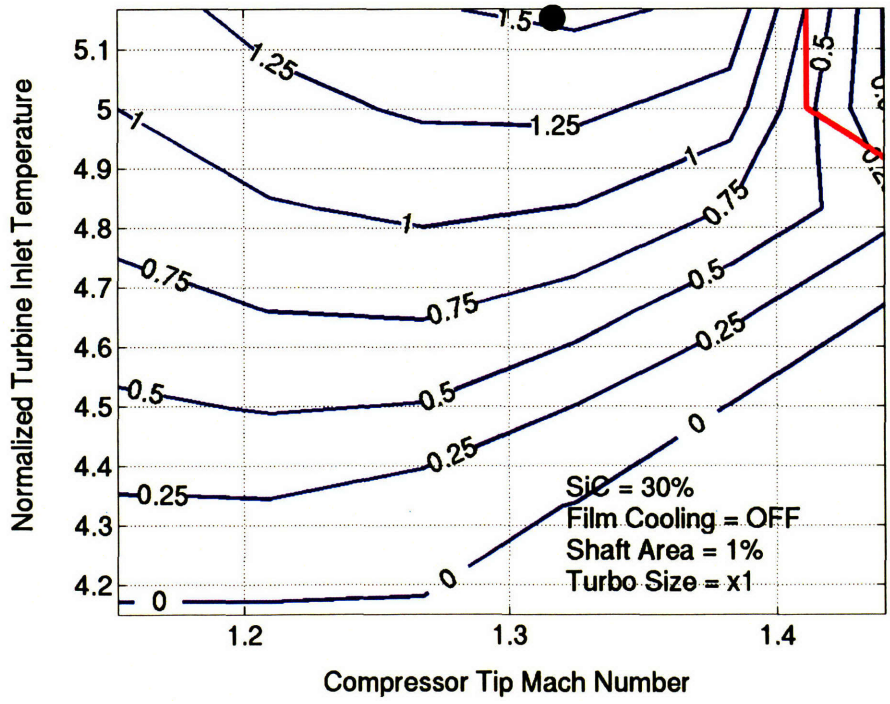
Normalized Turbine Inlet Temperature
Compressor Tip Mach Number
5.1
5
4.9
4.8
4.7
4.6
4.5
4.4
4.3
4.2
1.2
1.3
1.4
SiC = 30%
Film Cooling = OFF
Shaft Area = 1%
Turbo Size = x1

(b)

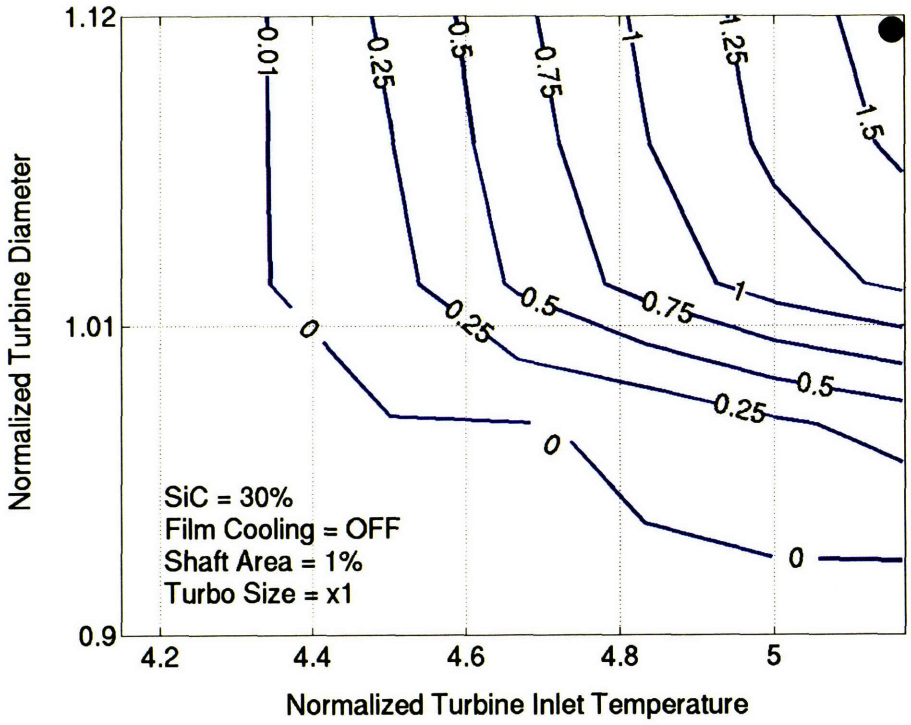

(c)

Figure 5.6 System efficiency contours showing effect of turbine size, compressor tip speed, and turbine inlet temperature on engine A performance (Size = x1, SiC = 30%, Film Cooling = OFF, Shaft = 1%). NOTE: Red line indicates turbine fracture.

The trends in optimal speed (pressure ratio) for the selected engines are similar to the ones for large engines. It can be noted in Figures 5.6 (a) and (b) and 5.7 (a) and (b) that optimal pressure ratio increases with turbine size (turbine efficiency) and with turbine inlet temperature. Turbine efficiency improves with increasing turbine size due to reduction in exit loss [12]. Parasitic power loss associated with turbine disk gap, however, is very low because the gap is large (~50 um) and the increase of power loss with speed is less important. For *ideal* cycles performance increases continuously with pressure ratio until the compressor exit temperature approaches the turbine inlet temperature. Therefore, if optimal turbine inlet temperature is increased the optimal pressure ratio will also increase for given component performance level for non-ideal engines.

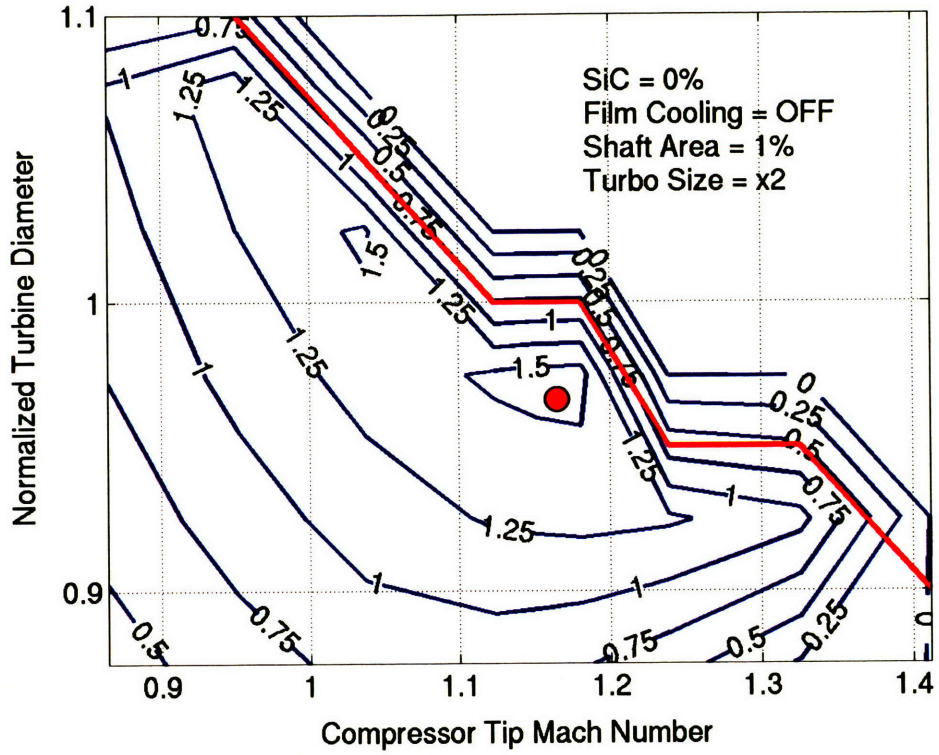
SiC = 0%
Film Cooling = OFF
Shaft Area = 1%
Turbo Size = x2
Normalized Turbine Diameter
Compressor Tip Mach Number
1.1
1
0.9
0.9
1
1.1
1.2
1.3
1.4

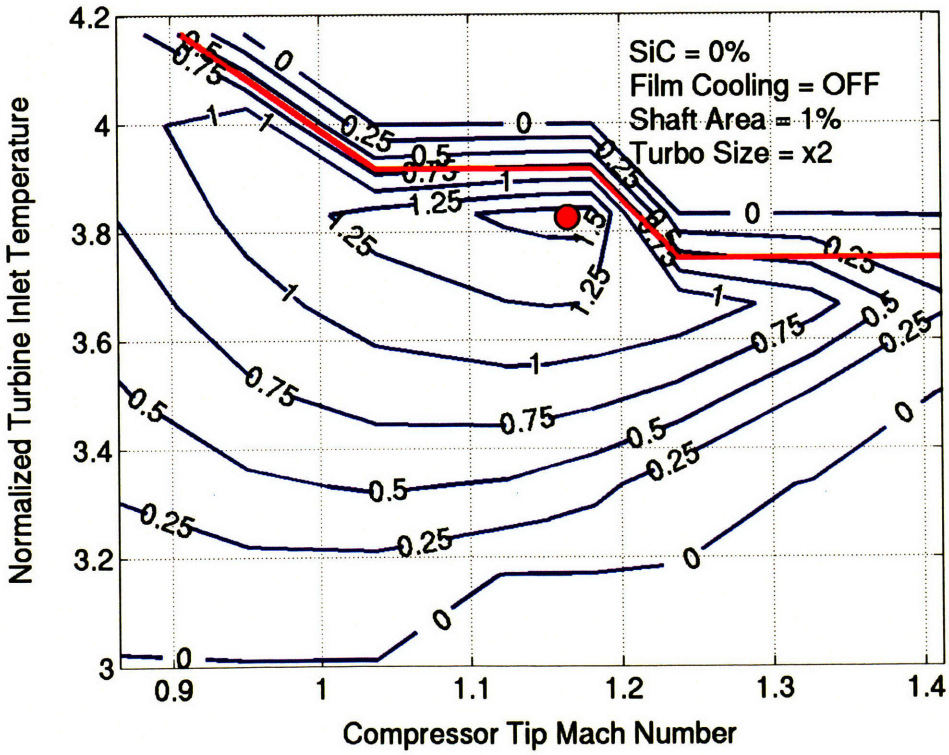
SiC = 0%
Film Cooling = OFF
Shaft Area = 1%
Turbo Size = x2
Normalized Turbine Inlet Temperature
Compressor Tip Mach Number
4.2
4
3.8
3.6
3.4
3.2
3
0.9
1
1.1
1.2
1.3
1.4

(a)

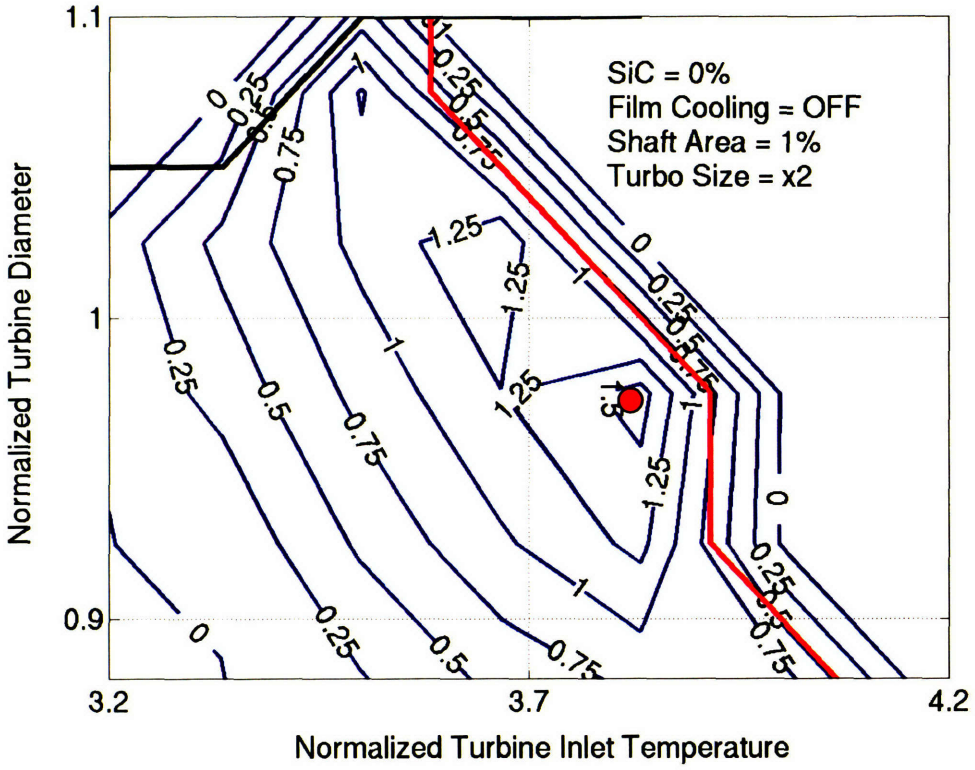

(c)

Figure 5.7 System efficiency contours showing effect of turbine size, compressor tip speed, and turbine inlet temperature on engine B performance (Size = x2, SiC = 0%, Film Cooling = OFF, Shaft = 1%). NOTE: Red line indicates turbine fracture.

In general system efficiency and net power improve with turbine size, and there is optimal turbine inlet temperature and system pressure ratio for a given engine. The optimum in turbine inlet temperature was discussed at length in section 5.3.2. The optimal pressure ratio is governed by the optimal turbine inlet temperature, the level of parasitic loss, the level of component performance and the structural limits of the components. The pressure ratio and turbine size for peak efficiency can be increased with a relaxation in the structural limits of the turbine through SiC reinforcement, as expected. A structurally stronger turbine can be increased in size to improve performance or rotor shaft resistance can be increased to improve compressor performance.

The provided design maps for the selected engines delineate the relevant design trade-offs and limitations to enable the designer to select the proper set of design parameters according to project requirements, priorities, and technology capabilities.

The effect of combustor, casing, and static structure geometry on system performance and size is of secondary importance and is discussed in Appendix B

5.4 CANDIDATE DESIGNS FOR SELF-SUSTAINED ENGINE

5.4.1 DESCRIPTION OF CANDIDATE DESIGNS

Two promising design candidates are selected for the development of a self-sustained micro engine. One design is called A and the other B throughout the chapter and they are indicated with black and red circles respectively on the figures in the chapter (Fig 5.1–5.7). These two designs differ mainly in their technology requirements. Table 5.2 presents detailed information about the two designs. Engine A relies on 30% Silicon Carbide (SiC) thickness in the turbine disk to hold the turbine together but does not require any increase in turbomachinery size (the technology for deeper wafer etching). Engine B relies on technology to etch two times bigger turbomachinery (1mm etch) and does not require any SiC reinforcement in the turbine. The designs are selected to make use of the maximum advances in one particular technology that can be envisioned for the near future. None of the designs requires turbine film cooling. The selection of a single design between the two for further development depends on the assessment of the development risk associated with each technology.

5.4.2 ADVANTAGES OF DESIGN B

There are advantages to design B:

- lower rotating design speed (thus mitigating rotor dynamic difficulties)
- simpler thermal isolation shaft design (no structural or bonding problems)
- no SiC reinforcement required in the turbine

First, the optimal design speed of the rotor is lower than the one for the baseline case and can be lowered further away from the optimum if necessary. This would certainly mitigate the rotor dynamic challenges, which confront the development and demonstration of the micro-engine [29]. Second, the thermal isolation shaft required for design B is the simplest possible. It can be designed with four columns thus eliminating all structural and bonding problems. In contrast, a structurally viable thermal isolation shaft for engine A still does not exist. The attempted designs are being driven to very complex geometry and manufacturing (Fig. B.4 and B.5, Appendix B).

CANDIDATE DESIGNS			
	Design A	**Design B**	**Design C**
PERFORMANCE			
Net Shaft Power	11 Watts	23 Watts	80 Watts
Chemical to Shaft Mechanical Efficiency	1.90%	1.60%	3.10%
Mass Flow	0.52 g/s	2.24 g/s	2.07 g/s
TECHNOLOGY			
SiC	30%	0%	30%
Etch Depth	474 um	992 um	975 um
Film Cooling	No	No	No
Isolation Shaft Thermal Resistance	24	6	4.8
CYCLE			
Pressure Ratio	2.5	1.9	1.85
Compressor Tip Speed	475 m/s	400 m/s	400 m/s
Turbine Inlet Temperature	1650 K	1140 K	1650 K
Effective Turbine Inlet Temperature	1460 K	1090 K	1530 K
Heat Addition Parameter	0.3	0.14	0.23
Compressor Efficiency	50%	59%	54%
Turbine Efficiency	69.00%	69%	65%
Parasitic Power Loss	17 Watts	25 Watts	26 Watts
GEOMETRY			
Engine Radius	14.4 mm	23.1 mm	29.0 mm
Compressor Outer Radius	4 mm	8 mm	8 mm
Compressor Inner Radius	2 mm	4 mm	4 mm
Compressor Blade Span	400 um	800 um	800 um
Turbine Outer Radius	4.4 mm	8.0 mm	8.0 mm
Turbine Inner Radius	3.9 mm	7.5 mm	7.5 mm
Turbine Blade Span	474 um	992 um	975 um
Static Structure Outer Radius	6.5 mm	10.5 mm	10.5 mm
Combustor Outer Radius	13.8 mm	22.3 mm	28.2 mm
HEAT TRANSFER			
Compressor Temperature	577 K	475 K	535 K
Turbine Temperature	1145 K	891 K	1215 K
Engine Casing Temperature Near Compressor	641 K	492 K	540 K
Static Structure Temperature	963 K	688 K	861 K
Total Heat Transfer to Compressor	47 Watts	91 Watts	143 Watts
Combustor Bypass to Mainstream Flow Ratio	0.16	0.55	0.14

Table 5.2 Candidate designs for a self-sustained micro-engine.

5.4.3 ENERGY AND AVAILABILITY ACCOUNTING FOR ENGINE DESIGN B

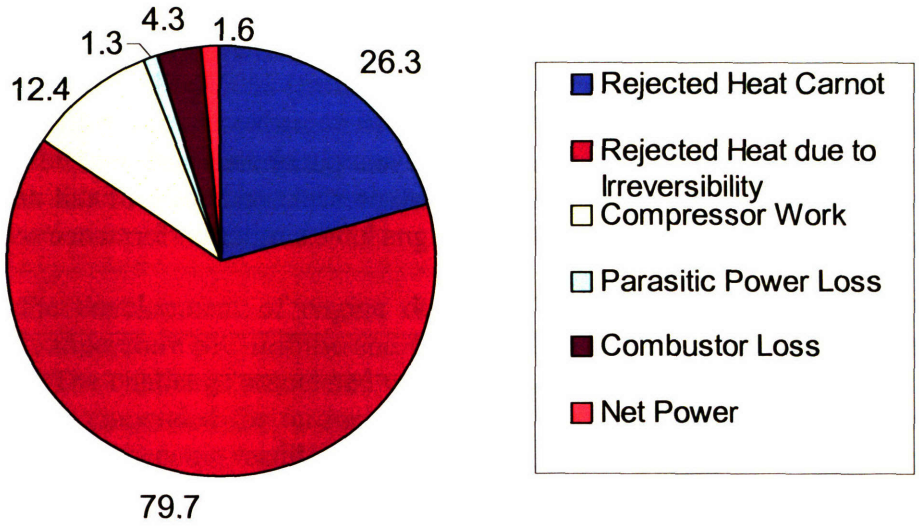

Figure 5.8 Energy diagram for proposed micro-engine in percentage of input energy

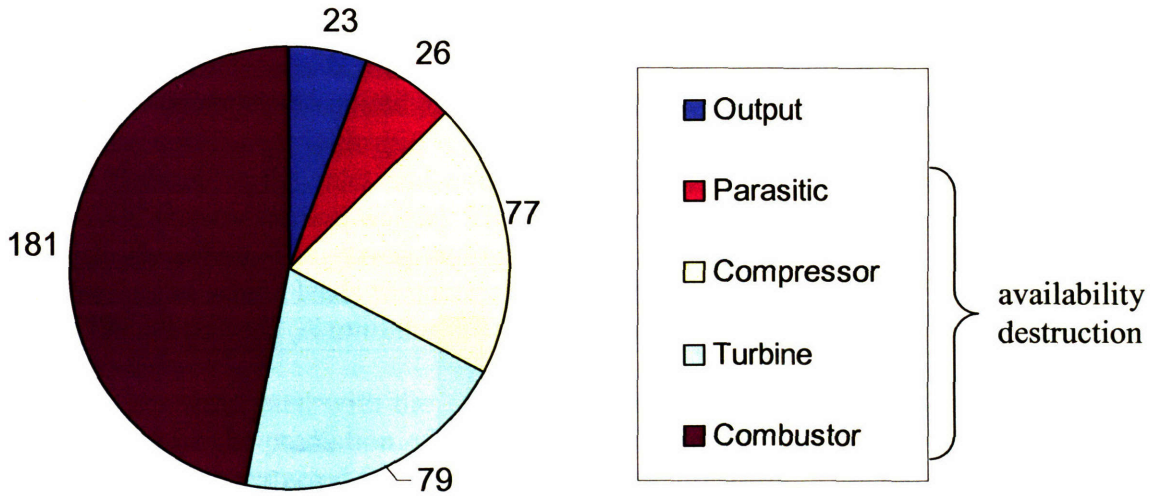

Figure 5.9 Engine power output and destruction of availability (Watts) in engine components.

Figure 5.8 presents the flow of energy in the proposed micro-engine. Part of the fuel energy is not converted into heat in the combustor and this is depicted as combustor loss. The available energy goes to the turbine. A large fraction is not utilized and is rejected as heat to the atmosphere. Part of this heat rejection would take place in an ideal Carnot engine. The rest is due to irreversibility. Some energy is consumed to drive the compressor and to overcome the parasitic losses and is also ultimately rejected. Only 1.6% of the chemical energy is converted to useful mechanical work.

Figure 5.9 describes the destruction of availability in the engine components. The combustor loss is dominant followed by the irreversibility in the turbomachinery. Therefore, an improvement in combustor and turbomachinery efficiency would be most advantageous to

engine performance. The destruction of available work associated with the rejection of heat to the atmosphere is not shown for clarity.

5.4.4 PERFORMANCE SENSITIVITY TO CYCLE AND COMPONENT PARAMETERS

The sensitivity of the system performance to the cycle parameters and component performance levels is also investigated. Figures 5.10 and 5.11 present sensitivity of the net power of the engine designs to the cycle parameters. Both designs have similar performance sensitivity.

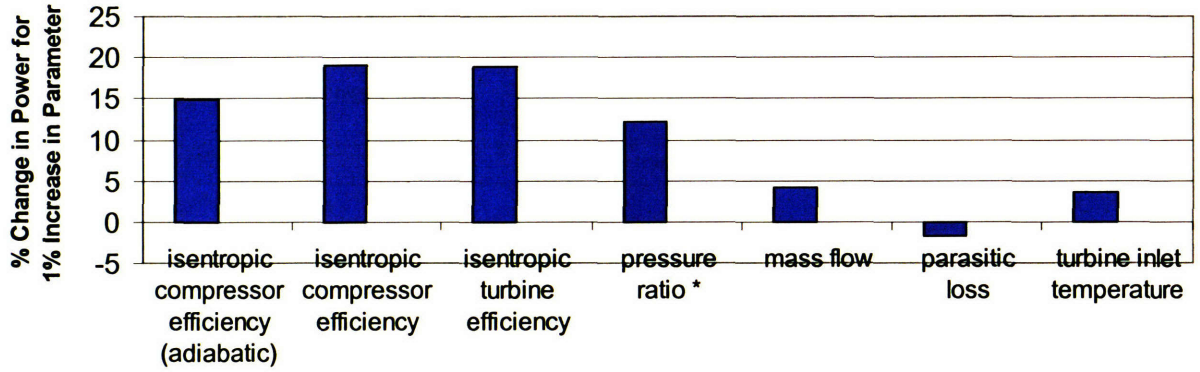

Figure 5.10 Sensitivity of design A performance to prediction of system parameters. * Pressure ratio is to power of $(\gamma-1)/\gamma$

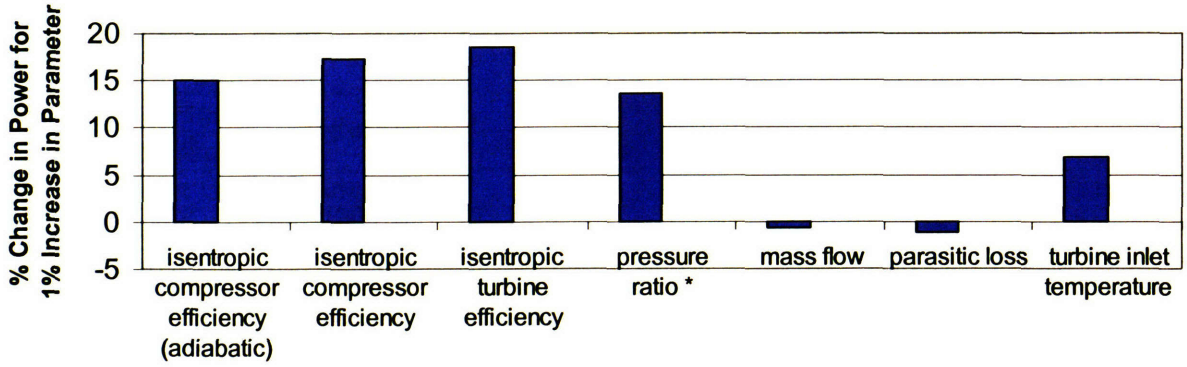

Figure 5.11 Sensitivity of design B performance to prediction of system parameters. * Pressure ratio is to power of $(\gamma-1)/\gamma$

System performance is most sensitive to turbomachinery performance. The margin in terms of turbomachinery efficiency is about 5 efficiency percentage points total allowable error for each design. This is not a large margin and this is why the highest fidelity tools (3-D CFD) are used for turbomachinery performance prediction. The margin associated with turbine inlet temperature prediction is considerably higher for design A because the turbine does not operate near its structural limit. For engine B the cycle can operate with an approximately 160 K lower

turbine inlet temperature and still break even (net power equal zero). Engine A can operate with 400 K lower turbine inlet temperature.

To consume the available power margin the parasitic power loss has to increase by 92% (from 25 Watts) for engine B and by 60% (from 17 Watts) for engine A. Engine A is more sensitive to changes in mass flow as expected since its mass flow is about 4 times lower. Overall, the margin for success of the two candidate designs is controlled by turbomachinery performance. It can be concluded that there is a reasonable chance for both designs to demonstrate self-sustained operation.

In summary the development of engine design B involves overall lower technical risk by avoiding high temperature SiC turbine and complicated shaft designs and by operating at lower rotating speed. The challenge associated with design B is the requirement to etch 1 mm blades. This design is recommended for further development unless Si-SiC technology and innovative isolation shaft design become readily available in the near future, or rotor dynamic requirements suggest otherwise.

The proposed engine design B can produce 23 Watts of net shaft power at chemical-to-mechanical conversion efficiency of 1.6%. The following paragraphs provide a general idea about the uncertainty associated with the quoted performance level. As described in the previous paragraphs the engine net power is most sensitive to turbomachinery performance. Turbomachinery performance is based on CFD solutions and correlations for the condition of interest (geometry, rotating speed, heat transfer). The CFD computational grid is such that the figures of merit do not change with grid refinement. The convergence of the CFD solutions is such that the difference in the inlet and exit mass flux is at most 3% for cases with locally unsteady flow-field (separation and wakes). The inability to achieve higher accuracy is due to the selection of a steady solver. The corresponding uncertainty in turbomachinery efficiency is less than 1 efficiency point, which leads to uncertainty in the net power of the engine of less than 4 Watts (17% of the net power). A minimum of 10 Watts power margin is desired for any design.

Higher uncertainty is associated with the determination of heat transfer coefficients in the heat transfer model and with the prediction of parasitic losses. The heat transfer coefficients for the turbomachinery flows are extracted from CFD and assumed constant. This assumption may lead to uncertainty in the coefficients of up to 15% for the investigated range. This is estimated from the scaling of Nusselt number with characteristic length for turbulent flow. However, the assumed heat transfer coefficients are selected to be at the higher end to provide conservative estimates. It was also shown that engine power is less sensitive to heat transfer coefficients than to turbomachinery performance. The corresponding uncertainty in engine net power is less than 18% (4.3 Watts).

Some parasitic power losses such as those caused by the isolation shaft flows or the flows in the shroud gap are not characterized in details. Their scaling is assumed based on CFD solutions for simple geometry and thus introduces additional uncertainty. However, the assumed scaling is investigated with CFD for the range of interest and it is confirmed that the assumptions are conservative. It is found that the consumed power is over-estimated by as much as 1 Watt. Uncertainty associated with the power loss in rotor bearings and seals is expected to be small. Uncertainty associated with heat transfer coefficients for stationary channel flow is also expected to be small due to the use of well established analytical expressions and correlations.

If it is assumed that the uncertainty in the net engine power is additive it follows that the net engine power can be expected to be within 40% of the quoted 23 Watts for the proposed engine design B. In the worst case, therefore, the engine is expected to produce about 14 Watts.

Table 5.2 also includes the estimated performance of design C that consists of incorporating SiC into the turbine of design B. This is to provide a general idea about the best possible performance of the proposed engine for the situation when both deep etching and SiC advanced technologies are available. Design C, however is optimized for operation without SiC and only a fraction of the potential benefit due to SiC addition can be realized. The requirements for the geometry of Engine C are shown in Table 5.2. To make the engine design robust and to make sure that the engine can operate with (C) and without SiC (B) the selected engine should accommodate the requirements of both designs. For example, the combustor in design C needs to be larger than the one required in design B. Therefore, it is recommended that the engine for development is designed with the larger combustor.

5.5 SUMMARY

The results from the integrated system model were interrogated in this chapter to establish minimum requirements for the self-sustained micro engine and to gain insight into micro-engine system behavior. It was found that a self-sustained engine would require either 30% of SiC reinforcement in the turbine, or an increase in turbomachinery size of 60%, or very effective turbine film cooling or a combination of these technologies. It was also found that non-adiabatic turbomachinery operation has an important implication on turbine inlet temperature choice and cycle selection. A turbine inlet temperature for peak engine efficiency exists in contrast to cycles for large-scale engines. An increase in system performance with turbomachinery size was reported which is also characteristic of micro-engines only and is related to parasitic power loss and heat transfer. Two candidate designs of similar performance were proposed. Each requires a different set of advanced technologies. The technical risk in the all-silicon design B is judged to be lower and this engine is recommended for further development with the possibility of including SiC in the turbine, when available.

CHAPTER 6

6 CONCLUSIONS

6.1 SUMMARY OF THE RESEARCH

1. General design guidelines for non-adiabatic micro-impellers are formulated for rational impeller design. The guidelines are based on impeller performance characterization. A compressor analysis tool is developed to guide the selection of impeller geometry. The analysis tool consists of a set of simplified models for the various performance limiting physical processes extracted from computed flow by CFD.

2. An integrated system model is proposed and developed to describe micro engine system behavior and account for engine heat transfer. The heat addition parameter characterizes the coupling of components to system through heat transfer. This coupling renders conventional preliminary cycle analysis and design methodology ineffective because the performance of the components cannot be taken as invariant. For instance compressor performance changes significantly for each set of system design parameters. To account for this effect and for the relevant fluid and thermodynamic, structural and fabrication constraints the integrated system model is developed.

3. A design study is performed with the integrated system model to assess system behavior with changes in the cycle parameters and to generate maps of the system design space. These maps are used to establish minimum requirements on advanced technologies for a self-sustained engine. They also guide the selection of parameters for a self-sustained engine system.

4. Based on the design maps generated with the integrated system model two candidate designs are selected and discussed. They rely on different technology for successful operation. One design uses 30% of SiC in the turbine disk and a complicated shaft design (in progress) while the other engine design relies on improvements in etch depth capability. The latter design uses two times larger turbomachinery and does not require any SiC or turbine cooling.

6.2 CONCLUSIONS

The work in this thesis leads to the following conclusions:

1. Differences between the design of micro and conventional impellers are delineated. Geometry for peak isentropic efficiency for non-adiabatic impellers changes with wall temperature. Impeller inlet angle, back-sweep angle, solidity, and radial size for peak efficiency decrease with increasing wall temperature. It is shown that an impeller optimized for adiabatic conditions and operated at high wall temperature (950K) may

incur an additional performance penalty as high as 11 efficiency points for the proposed designs. This behavior is unique to micro-turbomachinery and is a result of the non-adiabatic regime of operation.

2. Micro-compressor performance is determined by the aerodynamic quality of the impeller (characterized by polytropic efficiency) and by the level of heat addition to the compressor flow (characterized by the heat addition parameter). At high levels of heat addition to the impeller flow and high impeller wall temperatures it is beneficial to reduce the aerodynamic quality of the impeller by changing geometry in order to reduce the heat addition parameter. This leads to improved overall compressor performance.

3. Impeller wall temperature is needed for an optimal design of micro-impellers. However, the impeller temperature can only be determined by considering the operation of the impeller within the entire engine system (impeller, diffuser, turbine, bearings, supporting static structure and casing, isolation shaft) because the heat transfer between components essentially couples the components and the engine system. This called for the need for an integrated engine system model.

4. Based on results from the integrated system model it is found that the thermodynamic cycle selection for micro-engine systems differs from that for large conventional engines:

   - Turbine inlet temperature for peak efficiency exists for micro-engines in contrast to large engines. This is a result of two competing effects. As turbine inlet temperature increases cycle performance improves, but heat transfer to compressor flow also increases leading to deteriorating compressor and cycle performance. The net effect depends on the relative importance of the two mechanisms.

   - System efficiency improves appreciably with increasing turbomachinery size. This is related to the scaling of system mass flow, heat transfer, and parasitic power losses in micro-engines with size. The optimal size for a gas turbine engine in terms of power density is larger than the reference micro-engine size.

5. The minimum requirements on advanced technologies for a self-sustained engine are established as follows:

   - 30% of SiC reinforcement for the micro-turbine or
   - 60% increase in turbomachinery size or
   - film cooling effectiveness leading to nearly adiabatic turbine disk operation and
   - 1% thermal isolation shaft area as fraction of compressor disk area

6. A self-sustained engine producing 20 Watts of shaft mechanical power at chemical-to-shaft mechanical conversion efficiency of 1.6% can be designed and built.

6.3 RECOMMENDATIONS FOR FUTURE WORK

1. It has been shown that system performance is sensitive to turbomachinery performance. One way to further improve turbomachinery performance is to use variable blade span technology [26,27] along with the non-adiabatic design guidelines. For a given impeller wall temperature it is possible to further improve impeller performance by increasing blade span only instead of scaling the whole turbomachine and by employing variable span technology to control passage diffusion. The variable blade span technology is currently being developed at the University of Maryland and is expected to become available in the near future [26,27]. Research investigating the possible system improvement is recommended.

2. Another step in the improvement of micro-engine system performance would be the development of turbine film cooling technology as discussed in Chapter 4. It was shown by Phillipon [17] that such technology is feasible on micro scale. Evans [24] did some initial assessment of cooling schemes and their impact on system performance. What remains to be done is a detailed characterization of cooling effectiveness in micro turbines in terms of non-dimensional design parameters. The interactions between cooling flows and main flow and the effects on component performance need to be examined and quantified.

3. To improve the fidelity of the integrated system model it is recommended that the stress estimation model for the micro-turbine should be revisited and further developed. It would be useful to include models to predict the bending moments and shear stresses in the turbine disk and blades. Currently the model quantifies only the centrifugal stresses in the turbine disk and the stresses in the blade roots due to bending by the centrifugal force.

4. More work is needed to quantify the behavior of Si-SiC hybrid structures at elevated temperatures. The available results and predictions are limited to 1200 K [14]. It may become important to operate the micro-turbine at higher temperatures in the future to achieve the desired performance levels.

REFERENCES

[1] Epstein, A. H., 2003, "Millimeter-scale, MEMS gas turbine engines", ASME paper No. GT2003-38866.

[2] Epstein, A. H., et al., 1997, "Micro-Heat Engines, GasTurbines, and Rocket Engines - The MIT Microengine Project", 28th AIAA Fluid Dynamics Conference, 4th AIAA Shear Flow Control Conference, AIAA97-1773.

[3] Epstein, A. H., et al., 2000, "Shirtbutton-sized gas turbines: The Engineering Challenges of Micro High Speed Rotating Machinery", Proc. The 8th International Symposium on Transport Phenomena and Dynamics of Rotating Machinery, Honolulu, Hawaii.

[4] C. Groshenry, "Preliminary Design Study of a Micro-Gas Turbine Engine." MS Thesis, MIT, Department of Aeronautics and Astronautics, 1995.

[5] L. Frechette, Development of a Silicon Microfabricated Motor-Driven Compressor, PhD Thesis, MIT, Department of Aeronautics and Astronautics, 2000.

[6] A.P. London, Development and Test of a Microfabricated Bi-Propellant Rocket Engine, PhD Thesis, MIT, Department of Aeronautics and Astronautics, 2000.

[7] R.L. Bayt, Analysis, Fabrication, and Testing of a MEMS-Based Micropropulsion System, PhD Thesis, MIT, Department of Aeronautics and Astronautics, 1999.

[8] C. Protz, Experimental Investigation of Microfabricated Bipropellant Rocket Engines, PhD Thesis, MIT, Department of Aeronautics and Astronautics, 2004.

[9] A.A. Ayon, J. Protz, R. Khanna, X. Zhang, and A. Epstein, "Application of Deep Silicon Etching and Wafer Bonding in the MicroManufacturing of Turbochargers and Micro-Air-Vehicles, " 47th International Symposium of the American Vacuum Society, Boston, MA, October, 2000.

[10] A. A. Ayon, Ishihara, K., Braff, R., Sawin, H.H., and Schmidt, M., "Deep Reactive Ion Etching of Silicon," Invited Presentation at Materials Research Society Fall Meeting, Boston, MA, November 30-December 4, 1998.

[11] Mirza, A.R., and Ayon, A.A., "Silicon Wafer Bonding: Key to MEMS High-Volume Manufacturing," SENSORS, Vol. 15, No. 12, December 1998, pp. 24-33.

[12] Gong, Y., Sirakov, B.T., Epstein, A.H., Tan, C.S., "Aerothermodynamics of Micro-turbomachinery," ASME paper No. GT2004-53877.

[13] Krain, H. 1987, "Swirling impeller flow." 32nd ASME Gas Turbine Conference and Exhibit, Anaheim, Callifornia. Paper 87-GT-19.

[14] H.S. Moon, Design of Si/SiC Hybrid Structures for Elevated Temperature Micro-Turbomachinery, PhD Thesis, MIT, Department of Aeronautics and Astronautics, 2002.

[15] D.W. Choi, Silicon Carbide Process Development for Microengine Applications: Residual Stress Control and Microfabrication, PhD Thesis, MIT, Department of Aeronautics and Astronautics, 2004.

[16] Casey, M.V., 1985, "The Effects of Reynolds Number on the Efficiency of Centrifugal Compressor Stages," ASME Journal of Engineering for Gas Turbines and Power, 107: pp.541-548.

[17] Philippon, B., Design of a film cooled MEMS micro turbine", MS Thesis, MIT, Department of Aeronautics and Astronautics, 2001.

[18] Kang, S, Johnston, J.P., Arima,T., Matsunaga, M.,Tsuru, H. and Prinz, F.B., "Micro-scale Radial- flow Compressor Impeller made of Silicone Nitride – Manufacturing and Performance.", ASME paper No. GT2003-38933.

[19] Shirley, G., An experimental Investigation of a Low Reynolds Number, High Mach Number Centrifugal Compressor, MS Thesis, Department of Aeronautics and Astronautics,

2004.

[20] Isomura, K., Murayama, M., and Kawakubo, "Feasibility Study of a Gas Turbine at Micro Scale", ASME paper No. 2001-GT-101.

[21] Tanaka, S., et al., 2002, "Design and Fabrication Challenges for Micromachined Gas Turbine Generators", Proc. The 9th International Symposium on Transport Phenomena and Dynamics of Rotating Machinery, Honolulu, Hawaii.

[22] Protz, J. M., An Assessment of the Aerodynamic, Thermodynamic, and Manufacturing Issues for the Design, Development, and Microfabrication of a Demonstration Micro Engine, PhD Thesis, MIT, Department of Aeronautics and Astronautics, 2000.

[23] Kerrebrock, J. L., Micro-engine cycle analysis, Internal Memo, GTL, MIT, 2000.

[24] Evans, S. W., Thermal Design of a Cooled Micro Gas Turbine, MS Thesis, MIT, Department of Aeronautics and Astronautics, 2001.

[25] FLUENT CFD code by FLUENT Inc., www.fluent.com

[26] Waits, C.M., Morgan, B., Kastantin, M., and Ghodssi, R., 2003, personal communication, also "Microfabrication of 3D Silicon MEMS Structures using Gray-scale Lithography and Deep Reactive Ion Etching," manuscript submitted to Sensors and Actuators A: Physical.

[27] Morgan, B., Waits, C.M., Krizmanic, J., Ghodssi, R., 2003, personal communication, also "Development of a Deep Silicon Phase Fresnel Lens using Gray-Scale Technology and Deep Reactive Ion Etching," manuscript submitted to Journal of Microelectromechanical Systems.

[28] GAMBIT model building and meshing software by FLUENT Inc., www.fluent.com

[29] Savoulides, N., Development of a MEMS Turbocharger and Gas Turbine Engine, PhD Thesis, MIT, Department of Aeronautics and Astronautics, 2004.

[30] Sirakov, B.T., Gong, Y., Epstein, A. H., Tan, C.S.," Design and Characterization of Micro-Compressor Impellers," ASME paper No. GT2004-53332.

[31] Owen, J.M., Rogers, R.H., Flow and Heat Transfer in Rotating-Disc Systems, Research Studies Press Ltd, 1989, pp 162-165.

[32] Cumpsty, N.A., Compressor Aerodynamics, Longman, 1989, pp. 269-276.

[33] Kerrebrock, J.L., Aircraft Engines and Gas Turbines, MIT Press, 1996.

[34] Fay, J.A., Introduction to Fluid Dynamics, MIT Press,1994, pp. 292-293.

[35] Greitzer, E. M., Tan, C.S., Graf, M.B., Internal Flow : Concepts and Applications, Cambridge University Press, 2004.

[36] Gong, Y., Personal Communication, 2001-2004.

[37] Li, H., Personal Communication, 2003-2004.

[38] Hamrock,B.J., Fundamentals of Fluid Film Lubrication, Marcel Dekker, 2004.

[39] Mills, A. F., Heat Transfer, Prentice Hall, 1998.

[40] Mehra, A., Development of a High Power Density Combustion System for a Silicon Micro Gas Turbine Engine, PhD Thesis, MIT, Department of Aeronautics and Astronautics, 2000.

[41] Spaddacini, C., Combustion Systems for Power MEMS Applications, PhD Thesis, MIT, Department of Aeronautics and Astronautics, 2004.

[42] Archer, R.R., An Introduction to Mechanics of Solids, McGraw-Hill, Inc., 1999.

[43] Chandrasekaran, V., Personal Communication, 2003-2004.

[44] Spakovszky, Z.S., Liu, L. X., "Scaling Laws for Ultra-Short Hydrostatic Gas Journal Bearings", ASME paper No. DETC2003/VIB-48468.

[45] Matlab software by The MathWorks, www.mathworks.com

[46] Mattingly, J.D, Elements of Gas Turbine Propulsion, McGraw-Hill, Inc.,1996.

APPENDIX A

EQUATIONS FOR HEAT TRANSFER MODEL

MODULE ONE

For the heat flows in module one the assumed flow directions are as follows (Fig 4.3). Heat flows to the compressor from all directions (shaft, shroud, journal bearing ...) and from the compressor structure to the compressor flow. Heat flows from turbine flow to turbine structure.

$$Q_{shaft} + Q_{shroud} + Q_{shroud\_seal} + Q_{journal\_bearing} + Q_{static\_structure} + Q_{radiation} = Q_{compressor} \tag{1.1}$$

$$Q_{shaft} + Q_{radiation} = Q_{turbine\_flow} \tag{1.2}$$

$$Q_{compressor\_flow} = \frac{(T_{compressor} - T_{compressor\_flow})}{R_{compressor}} = h_c A_c (T_{compressor} - T_{compressor\_flow}) \tag{1.3}$$

$$T_{compressor\_flow} = \frac{1}{2}(T_{Tc\_rel\_inlet} + T_{Tc\_rel\_exit}) \tag{1.4}$$

$$Q_{turbine\_flow} = \frac{(T_{turbine\_flow} - T_{turbine})}{R_{turbine}} = h_t A_t (T_{turbine\_flow} - T_{turbine}) \tag{1.5}$$

$$T_{turbine\_flow} = \frac{1}{2}(T_{Tt\_rel\_inlet} + T_{Tt\_rel\_exit}) \tag{1.6}$$

$$Q_{shaft} = \frac{(T_{turbine} - T_{compressor})}{R_{shaft}} = \frac{L_s (T_{turbine} - T_{compressor})}{k_s A_s} \tag{1.7}$$

$$R_{shaft} = \left(\frac{1}{R_{shaft\_convection}} + \frac{1}{R_{shaft\_conduction}} \right)^{-1} \tag{1.8}$$

$$Q_{shroud} = \frac{(T_{casing} - T_{compressor})}{R_{shroud}} = \frac{L_{shr} (T_{casing} - T_{compressor})}{k_{shr} A_{shr}} \tag{1.9}$$

$$Q_{shroud\_seal} = \frac{(T_{casing} - T_{compressor})}{R_{shroud\_seal}} + \frac{Q_{viscous\_seal}}{2} = \frac{L_{seal} (T_{casing} - T_{compressor})}{k_{seal} A_{seal}} + \frac{Q_{viscous\_seal}}{2} \tag{1.10}$$

$$Q_{journal\_bearing} = \frac{(T_{static\_structure} - T_{compressor})}{R_{jb}} + \frac{Q_{viscous\_jb}}{2} = \frac{L_{jb} (T_{shroud} - T_{compressor})}{k_{jb} A_{jb}} + \frac{Q_{viscous\_jb}}{2} \tag{1.11}$$

$$Q_{radiation} = A_{compressor} F \sigma (T_{turbine}^4 - T_{compressor}^4) \tag{1.12}$$

$$F = \frac{1}{\frac{1}{\varepsilon_{compressor}} + \frac{1}{\varepsilon_{turbine}} - 1} \tag{1.13}$$

Equation 1 describes the energy conservation in the compressor structure. The heat coming in is equal to the heat going out. **Equation 2** is energy conservation in the turbine structure. **Equation 3** describes the convective heat transfer between compressor structure and compressor flow. The temperature of the compressor flow is assumed to be the average temperature of the inlet and exit relative flow stagnation temperatures **(Eq. 4).** These temperatures are extracted from the compressor code or CFD, or estimated by rothalpy and added heat as described in Chapter 5. **Equation 5** describes the convective heat transfer between the turbine flow and the turbine structure. The same assumption about the turbine flow temperature is made **(Eq. 6). Equation 7** describes the heat transfer between the turbine and compressor structure through the isolation shaft. It can be described with an effective resistance **(Eq. 8)** which is the conductive resistance for the heat flow through the shaft structure in parallel with the convective resistance for the heat flow through the air flows in the space outside the shaft structure between the compressor and turbine disks. **Equation 9** describes the heat flow through the shroud cavity between the casing and the compressor shroud. It can be described with an effective thermal conductivity or overall resistance extracted from CFD. The heat flow between the casing and the compressor shroud through the shroud seal is described in **equation 10.** This is a result from the solution of the Poisson equation where the forcing is the heat generated in the seal. The heat flow through the journal bearing gap between the static structure and the compressor disk can be described in the same way **(Eq. 11). Equation 12** describes the heat transfer from the turbine disk to the compressor disk by radiation. This equation is non-linear in the unknowns and is solved separately in an iterative procedure to be passed as a known quantity to the remaining linear system. The estimation of flow and material thermal resistance for each equation is described in details in the next section. For each conduction equation, A is the cross-sectional area of the heat path, k the thermal conductivity, and L the length of the heat path. For each convection equation, A is the flow wetted area, and h is the convective heat transfer coefficient. Equations 4, 6, 8, and 13 are provided for clarity. The remaining 9 equations form the linear system to be solved.

THERMAL RESISTANCE ESTIMATION FOR MODULE ONE

Compressor and turbine flows: Convective heat transfer coefficients for the compressor and turbine are extracted from 3-D CFD solutions for representative conditions and geometry (Table A.1). Wetted area of the compressor and turbine can be calculated from turbomachinery geometry. The thermal resistance between the compressor flow adiabatic wall temperature and the compressor disk is simply the inverse of the product of wetted area and heat transfer coefficient [39].

$$Q = hA\Delta T = \frac{\Delta T}{R} \tag{1.14}$$

$$R = \frac{1}{hA} \tag{1.15}$$

where Q is the heat transfer, h is the convective heat transfer coefficient, A is the wetted area, R is the thermal resistance ($R_{compressor}$ in M1[2]), and ΔT is the driving temperature difference.

[2] M1, M2, and M3 are Modules One, Two and Three of the Heat Transfer Model in Appendix A

The convective thermal resistance between turbine flow and disk can be estimated analogously ($R_{turbine}$ in M1). The bulk flow adiabatic wall temperature is assumed to be the average of the inlet and exit relative stagnation temperatures for each component. The driving temperature difference is defined as the difference between the average relative stagnation temperature of the flow (between inlet and exit) and the material temperature of the component. At the moderate Mach numbers (M<<3) typical for turbomachinery flows it is appropriate to approximate the adiabatic wall temperature with the flow relative stagnation temperature [33]. For the compressor, inlet relative stagnation temperature can be easily estimated from velocity triangles at inlet and inlet absolute stagnation temperature. The exit relative stagnation temperature can be estimated either from rothalpy and the added heat [35] or can be extracted from the compressor one dimensional analysis code or CFD. The rothalpy at exit of the compressor will be equal to the rothalpy at inlet plus the added heat to the compressor flow (rothalpy is not conserved in the impeller due to the non-adiabatic conditions). Turbine inlet and exit relative stagnation temperatures are extracted from the turbine one-dimensional design code.

Thermal Isolation Shaft: The resistance of the thermal isolation shaft (R_{shaft} in M1) is selected as a design variable and is given as input. When, however, an actual shaft is chosen, its resistance will be the combination of two resistances in parallel. One will describe the conduction heat transfer taking place within the shaft and the other the convection heat transfer taking place between the compressor and turbine disks outside the shaft. The conduction resistance can be easily estimated from shaft geometry and thermal conductivity of silicon.

$$Q = \frac{kA}{L}\Delta T = \frac{\Delta T}{R} \tag{1.16}$$

$$R = \frac{L}{kA} \tag{1.17}$$

where Q is the heat transfer, A is the cross sectional area, L is the length, k is the thermal conductivity, and ΔT is the driving temperature difference.

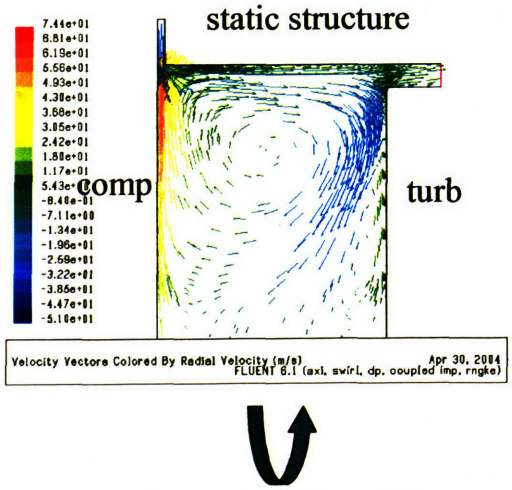

Figure A.1 Recirculation zones near the outer radius of the rotor causing increased convective heat transfer between turbine and compressor disks outside the thermal isolation shaft.

The convective resistance is not so trivial to find. Due to the centrifugal forces on the gas outside the shaft and the temperature difference between compressor and turbine the heavier cold gas on the compressor disk is thrown radially outwards and recirculation zones enhancing the heat transfer occur at the outer radius of the rotor (Fig A.1). These shaft flows are modeled with 3-D CFD (Fluent) and representative effective thermal conductivity is established for the shaft gap between the turbine and compressor disks as well as the dissipated power. Since shaft flows are driven by the rotor and their energy is dissipated by the stationary structure around the rotor, the dissipated power is directly debited to the power output of the engine. The exact shape of the shaft is not known at the design study stage and the shaft flows can be complicated depending on the shape so detailed characterization of shaft flows is not attempted. A representative performance and scaling based on simple shaft geometry and CFD solutions is used in the model. By using an effective thermal conductivity value (Table A.1) for the convective heat transfer between compressor and turbine it is assumed that the heat transfer would be proportional to the temperature difference and inversely proportional to the separating length between compressor and turbine which is supported by CFD analysis (Fig A.2). Dissipated power by the shaft flows is assumed to scale with compressor peripheral speed to the third power (making a parallel to dissipated power scaling for enclosed rotating disks [31]), which slightly over-predicts the loss as can be seen from comparison to CFD data (Fig A.3). The dissipated power by the shaft is assumed to remain invariant with driving temperature difference for the range of interest as suggested by CFD data (Fig A.4).

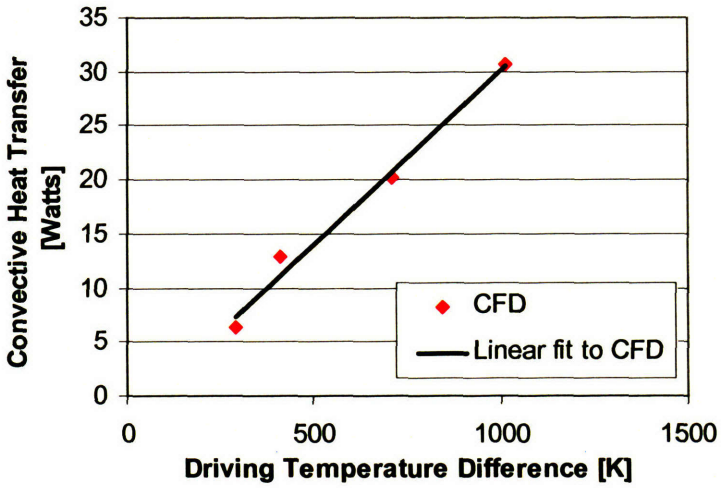

Figure A.2 Convective Heat Transfer Through Shaft Flows Between Compressor and Turbine.

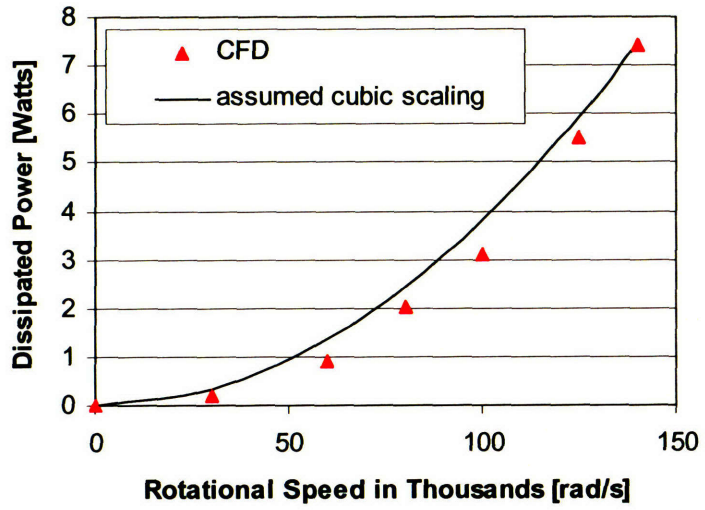

Figure A.3 Dissipated Power by Shaft Flows (compressor radius = 4 mm, T comp = 600, Ttur = 1200, shaft L = 500 um)

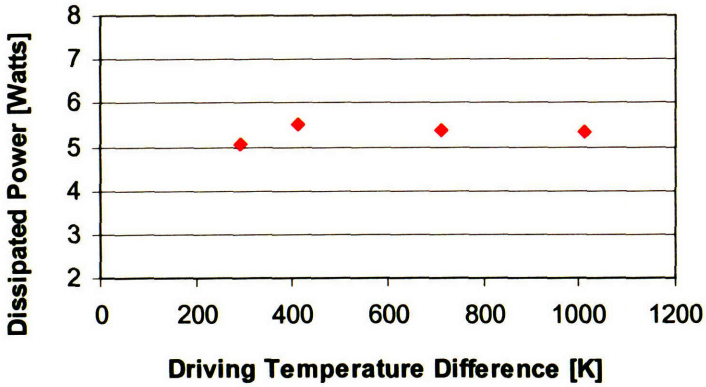

Figure A.4 Dissipated Power by Shaft Flows (comp radius = 4 mm, shaft L = 500 um, Omega = 125000 rad/s)

Compressor shroud: The convective resistance (R_{shroud} in M1 and R3 in M3) between the Casing Structure and the compressor shroud is estimated with axi-symmetric 2-D CFD (Fluent) for representative geometry and conditions. The radial extent of the shroud cavity is the radial extent of the shroud minus the length of the shroud seal. For the baseline geometry the radial length of the shroud cavity is 1.8 mm and the shroud is separated from the casing by a 50 micron gap. In the shroud cavity, the rotating shroud is pumping cold gas radially outwards setting recirculation zones and enhancing heat transfer and power dissipation but the effect is stronger than for the shaft because only the shroud is rotating and the casing is stationary. For the shaft flows both compressor and turbine are rotating. In the shroud cavity, however, the temperature difference between shroud and casing is typically smaller. An effective thermal conductivity for the gap between the shroud and the casing is also extracted from the CFD solution (Table A.1) and used in the model along with an estimate for the dissipated power. The dissipated power is

assumed to scale with compressor peripheral speed to the third power and with compressor radius to the fifth power as is the case for any enclosed rotating disk [31].

Compressor Journal Bearing and Shroud Seal: The gap of the compressor journal bearing is about 15-17 microns [44] and the gap of the shroud seal can be anywhere between 3 and 10 microns. The length of the journal is about 300 microns and the length of the seal is about 150-200 microns. The seal geometry is selected in such a way as to allow only 1-2% leakage of the total mass flow. Since the mass flow passing through both gaps at design condition is very small (1-3% of total mass flow) and the aspect ratios of the passages large (AR~15-100) the temperature profile in these flows very quickly acquires a constant shape (i.e the flow becomes fully developed both thermally and aerodynamically, Fig A.5a). However, there are heat sources in these types of flows because of the viscous dissipation in the gaps that should be accounted for. To find the temperature profiles in the gaps knowing the wall temperatures, the level of power dissipation, and the fact that the flow is fully developed the one-dimensional Poisson equation can be solved for the temperature profile from wall to wall (Fig A.5b). From the analytical temperature profiles, heat transfer coefficients can be estimated and the total heat transfer can be found. Since the solution procedure for the one-dimensional Poisson equation is well known it will not be discussed [39]. The thermal resistance for the shroud seal is R_{shroud_seal} in M1 and R2 in M3, and for the journal bearing is R_{jb} in M1 and R4 in M2.

	flow h (W/m^2K)	structure k (W/mK)
Compressor		
passages	2070	
inlet	1400	
Turbine		
blade	2000	
disk	1800	
Shaft		
conduction		60
convection		0.26
Shroud		
cavity		0.079
Diffuser	1600	
Turbine NGV	1255	

Table A.1. Heat transfer coefficients and effective conductivity.

It is important that the heat transfer through the compressor journal bearing is accurately predicted because it is the second largest after the one through the thermal shaft and both account for most of the heat going to the compressor. The results from the model are validated against CFD for different wall temperatures and levels of viscous dissipation, Q_{VISC} (Fig A.6)

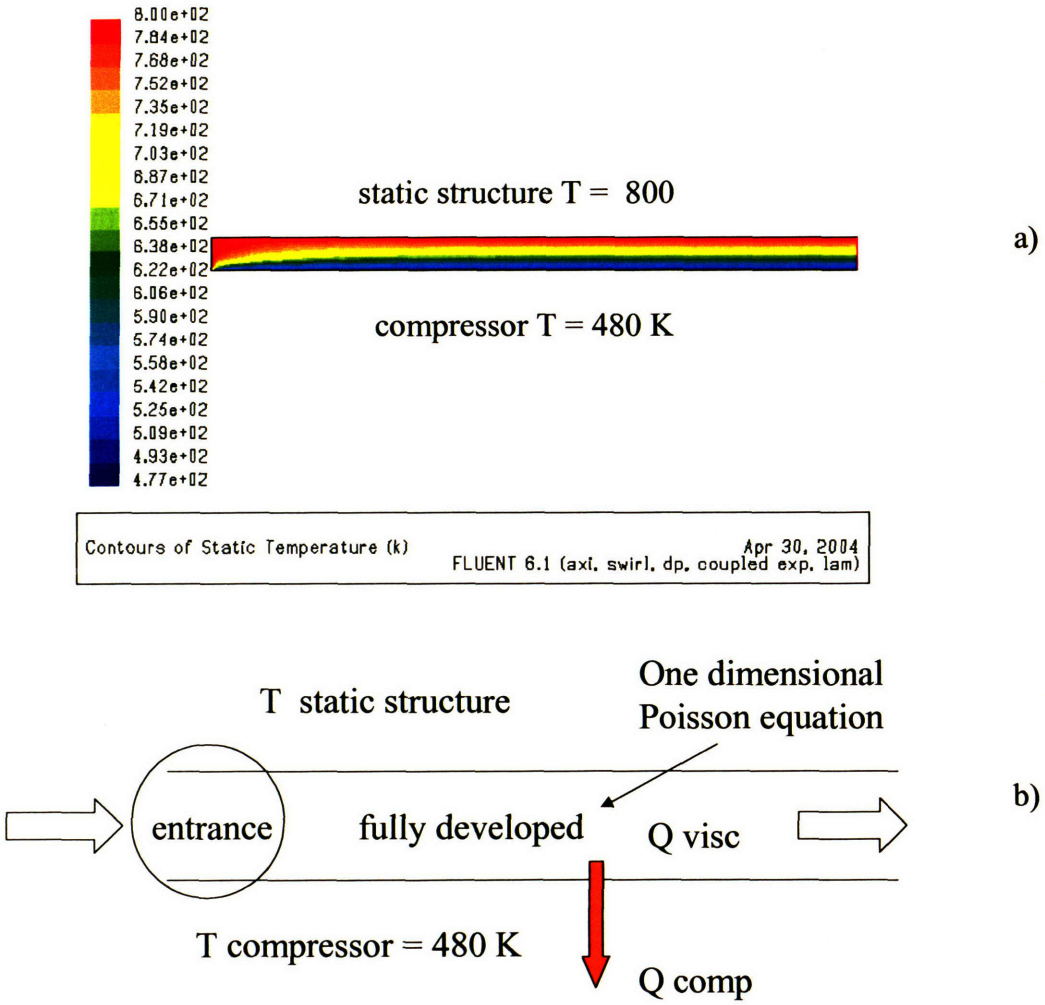

Figure A.5 Model for temperature distribution and heat transfer in journal and seal gaps. Contours of static temperature from CFD. b) Conceptual model

Turbine-to Compressor Radiation: Some heat transfer may take place between the hot turbine and the cold compressor by radiation if the turbine temperature is above about a 1000K (otherwise it can be neglected). To get an estimate the following expression can be used [39]:

$$Q_{rad} = A_{com} F_{12} \sigma (T_{tur}^4 - T_{com}^4) \tag{1.18}$$

$$F_{12} = \frac{1}{1/\varepsilon_{com} + 1/\varepsilon_{tur} - 1} \tag{1.19}$$

where, A is the compressor disk area, F_{12} is a transfer factor, σ is the Stefan-Boltzman constant, and ε is the emissivity of silicone at the given compressor or turbine temperature.

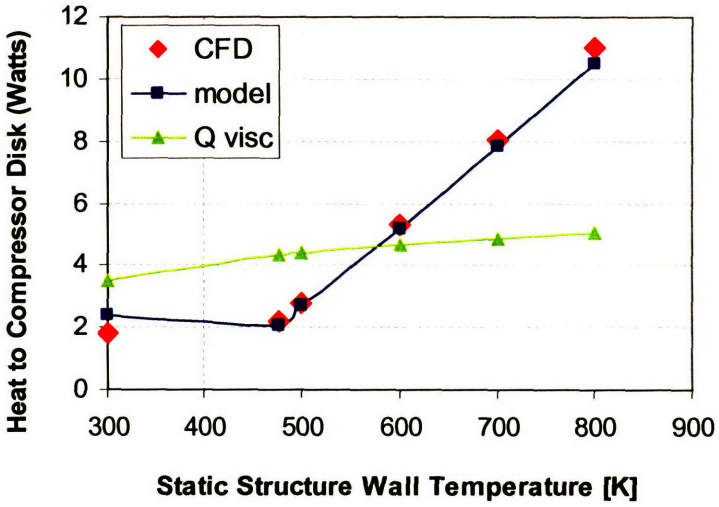

Figure A.6 Heat transfer to compressor through journal bearing gap

MODULE TWO

Module Two describes the static structure surrounding the rotor and the direction of the heat flows assumed in the equations is shown on Fig. 5.5. The nomenclature and numbering is also shown on figure 5.5. **Equation 1** is a statement of the heat balance in the static structure. The heat the goes into the structure equals the heat coming out of the structure. **Equation 2** describes the convective heat transfer from the engine casing to the diffuser flow. **Equation 3** describes the conduction heat transfer from the casing to the static structure through the diffuser blade tips and blades. **Equation 4** describes the convective heat transfer from the static structure to the diffuser flow. **Equation 5** describes the increase in stagnation enthalpy of the flow through the diffuser from the heat coming from the static structure and the casing. **Equation 6** describes the heat transfer taking place from the static structure to the compressor structure through the compressor journal bearing. The expression is the solution of the Poisson equation as described in Chapter 4. **Equation 7** describes the convective heat transfer from the static structure to the bypass flow. **Equation 8** describes the convective heat transfer from the hot combustor wall to the bypass flow. **Equation 9** describes the mixing of the bypass and combustor flows to the average turbine inlet temperature. **Equation 10** describes the convective heat transfer from the hot turbine NGV flow to the static structure. **Equation 11** describes the conduction heat transfer from the hot bottom combustor wall which extends to the NGV and turbine rotor to the static structure through the NGV blade tips and blades. **Equation 12** describes the convective heat transfer from the bottom combustor wall extension to the turbine NGV flow. **Equation 13** describes the conduction heat transfer from the combustor side wall to the static structure through connecting structural bridges. **Equation 14** describes the change in stagnation enthalpy in the bypass flow due to the heat transfer from the static structure and the combustor side wall. **Equation 15** describes the change in stagnation enthalpy of the turbine NGV flows due to the heat transfer from the combustor extended bottom wall and the static structure. **Equation 16** is not part of the linear system. It simply describes the relation between the mass flows in the engine. All mass flows are known quantities in module Two and then iteratively the ratio of combustor and bypass flow is varied so that the turbine inlet temperature is the desired one. The estimation of all resistances needed to solve the system is described next.

$$Q8 + Q7 + Q2 - Q5 - Q4 - Q3 = 0 \tag{2.1}$$

$$Q1 = A_1 h_1 (T_{case} - \frac{1}{2}(T0 + T1)) = \frac{(T_{case} - \frac{1}{2}(T0 + T1))}{R1} \tag{2.2}$$

$$Q2 = \frac{L_2 (T_{case} - T_{static})}{k_2 A_2} = \frac{(T_{case} - T_{static})}{R_2} \tag{2.3}$$

$$Q3 = A_3 h_3 (T_{static} - \frac{1}{2}(T0 + T1)) = \frac{(T_{static} - \frac{1}{2}(T0 + T1))}{R_3} \tag{2.4}$$

$$Q1 + Q3 = \dot{m}_{total}\, Cp_{01} (T1 - T0) \tag{2.5}$$

$$Q4 = \frac{L_4 (T_{static} - T_{compressor})}{k_4 A_4} - \frac{Q_{viscous\_jb}}{2} = \frac{(T_{static} - T_{compressor})}{R_4} - \frac{Q_{viscous\_jb}}{2} \tag{2.6}$$

$$Q5 = A_5 h_5 (T_{static} - \frac{1}{2}(T2 + T1)) = \frac{(T_{static} - \frac{1}{2}(T2 + T1))}{R_5} \tag{2.7}$$

$$Q6 = A_6 h_6 (T_{combustor\_wall} - \frac{1}{2}(T2 + T1)) = \frac{(T_{combustor\_wall} - \frac{1}{2}(T2 + T1))}{R_6} \tag{2.8}$$

$$T3 = \frac{\dot{m}_{bypass}\, Cp_2 T2 + \dot{m}_{combustor}\, Cp_{combustor} T_{combustor\_exit}}{\dot{m}_{total}\, Cp_{2-combustor}} \tag{2.9}$$

$$Q7 = A_7 h_7 (\frac{1}{2}(T4 + T3) - T_{static}) = \frac{(\frac{1}{2}(T4 + T3) - T_{static})}{R_7} \tag{2.10}$$

$$Q8 = \frac{L_8 (T_{combustor\_wall} - T_{static})}{k_8 A_8} = \frac{(T_{combustor\_wall} - T_{static})}{R_8} \tag{2.11}$$

$$Q9 = A_9 h_9 (T_{combustor\_wall} - \frac{1}{2}(T3 + T4)) = \frac{(T_{combustor\_wall} - \frac{1}{2}(T3 + T4))}{R_9} \tag{2.12}$$

$$Q10 = \frac{L_{10} (T_{combustor\_wall} - T_{static})}{k_{10} A_{10}} = \frac{(T_{combustor\_wall} - T_{static})}{R_{10}} \tag{2.13}$$

$$Q6 + Q5 = \dot{m}_{combustor}\, Cp_{12} (T2 - T1) \tag{2.14}$$

$$Q9 + Q7 = \dot{m}_{total}\, Cp_{34} (T4 - T3) \tag{2.15}$$

$$\dot{m}_{total} = \dot{m}_{bypass} + \dot{m}_{combustor} \tag{2.16}$$

THERMAL RESISTANCE ESTIMATION FOR MODULE TWO

Diffuser and NGV passages: The heat transfer coefficients for the diffuser and NGV passages are extracted from 3-D CFD (FLUENT) solutions for representative geometry and conditions (Table A.1) and are used in the model. Thermal resistance for diffuser flow is R2 and R3 in M2 and R5 and R17 in M3. Thermal resistance for NGV flow is R7 and R9 in M2.

Bypass Cooling Flow Passage: The heat transfer coefficient for the cooling bypass flow is estimated analytically. Once the dimensions of the passage are specified, the flow Reynolds number can be calculated from mass flow, geometry, and flow properties. Then an analytical expression for Nusselt number for flat plate boundary layer is used [39].

$$Nu = 0.664\,\mathrm{Re}^{\frac{1}{2}}\,\mathrm{Pr}^{\frac{1}{3}} \qquad (2.17)$$

It is assumed that due to the relatively large mass flow in the cooling passage and the short length of the passage the flow never develops fully within the passage. This assumption is turned into a requirement for the cooling passage design. Therefore, the heat from the hot combustor wall remains in the boundary layer and is carried away with the flow without being able to pass to the static structure. This assumption/requirement is justified/checked by estimating flow entrance length. An estimate for flow entrance length normalized with flow hydraulic diameter as a function of Reynolds and Prandtl numbers for laminar flow is used [39].

$$\frac{L_{entrance}}{D_h} = 0.017\,\mathrm{Re}_D\,\mathrm{Pr} \qquad (2.18)$$

Another, more obvious way to check if the flow is thermally fully developed is to check the estimated bulk temperature of the flow at the exit of the passage. If the flow has already assumed the average temperature of the two walls then the assumption for separate thermal boundary layers breaks down and the flow is fully developed. Thermal resistance for the bypass flows is R5 and R6 in M2.

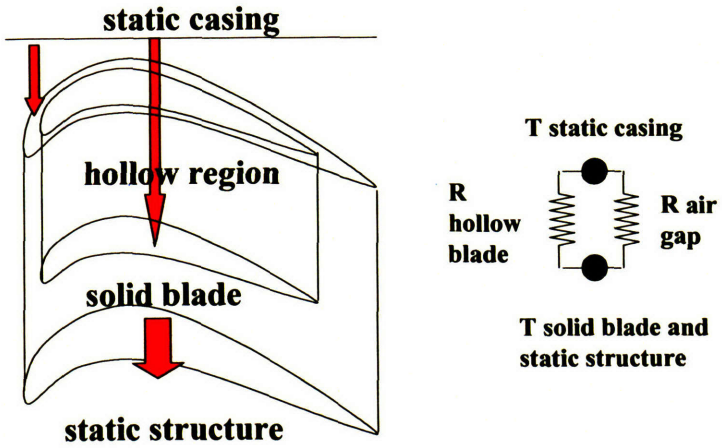

Figure A.7 Heat Flow in Diffuser and Turbine NGV blades.

Diffuser and NGV Blades: Heat from the casing and from the lower combustor wall passes directly to the static structure through the diffuser blade tips and the NGV blade tips respectively (Fig. A.7). The diffuser blades are designed not to touch the casing to avoid large heat flow by conduction through silicon. There is a baseline gap of 5 microns so that in this gap it is assumed that the heat transfer takes place by conduction through the gas in the gap. The diffuser blades are hollowed so that the surface area near the casing is minimized. The wall thickness of the blades is assumed to be 20 microns. The blades are hollowed for 100 um from the tip towards the hub. Therefore, the thermal resistance of these blades is the conductive resistance of the air gap in parallel with the conductive resistance of the hollow air gap (Fig A.7). The two resistances can be easily estimated from geometry and gas conductivity. The resistance of the solid silicon blade is ignored, as it is much lower. The NGV blades will be manufactured in the same way. Thermal resistance for diffuser blades is R2 in M2 and R6 in M3 and for NGV blades is R8 in M2.

Structure Connecting Bridges: To hold the structure together, solid connecting bridges are used between the combustor and the static structure. Heat transfer takes place by conduction through these bridges from the hot combustor wall to the cooler static structure. The thermal resistance (R10 in M2 and M3) of these connecting bridges can be easily estimated from geometry and the thermal conductivity of silicon. The bridges for the baseline layout have cross section of 100x100 microns and are 200 microns long. There are eight (8) bridges connecting the combustor to the static structure. The resistance of each is simply the length divided by the product of the cross sectional area and the material conductivity. For all cases the material conductivity used in the model is the material conductivity at the average temperature of the hot and cold driving temperatures. Silicon and air thermal conductivity is a function of temperature.

MODULE THREE

Module Three describes the heat flows in the engine casing. The assumed heat flow directions used in the equations and the nomenclature and numbering is shown on figure 5.6 in Chapter 5. The engine casing is separated into four isothermal blocks with temperatures Tc7, Tc8, Tc9, and Tc10.

Equation 1 describes the convection heat flow from the casing (Tc7) into the compressor inlet flow. **Equation 2** describes the conduction heat transfer from the casing (Tc7) to the compressor shroud through the shroud seal. This is a solution of the one dimensional Poisson equation. **Equation 3** describes the heat transfer from the casing (Tc7) to the compressor shroud through the shroud cavity. An effective thermal conductivity is used in the equation from 3D-CFD. **Equation 4** describes the conduction heat transfer from the casing block (Tc8) to block (Tc7). **Equation 5** describes the conservation of energy for block Tc7. It states that the heat coming into the block is equal to the heat leaving the block. **Equation 6** describes the convective heat transfer from the casing block (Tc8) to the diffuser flow. **Equation 7** describes the conduction heat transfer from the casing block (Tc8) to the static structure through the diffuser blade tips and blades. **Equation 8** describes the convection heat transfer from the casing block (Tc8) to the bypass flow. **Equation 9** describes the conduction heat transfer from casing block (Tc9) to casing block (Tc8). **Equation 10** describes the heat balance for casing block (Tc8). **Equation 11** describes the convective heat transfer from the combustor upper wall to the bypass flow.

$$Q1 = A_1 h_1 (Tc7 - \frac{1}{2}(T_{inlet} + Tc1)) = \frac{(Tc7 - \frac{1}{2}(T_{inlet} + Tc1))}{R_1} \tag{3.1}$$

$$Q2 = \frac{L_2 (Tc7 - T_{compressor})}{k_2 A_2} - \frac{Q_{viscous\_seal}}{2} = \frac{(Tc7 - T_{compressor})}{R_2} - \frac{Q_{viscous\_seal}}{2} \tag{3.2}$$

$$Q3 = \frac{L_3 (Tc7 - T_{compressor})}{k_3 A_3} = \frac{(Tc7 - T_{compressor})}{R_3} \tag{3.3}$$

$$Q4 = \frac{L_4 (Tc8 - Tc7)}{k_4 A_4} = \frac{(Tc8 - Tc7)}{R_4} \tag{3.4}$$

$$Q4 = Q3 + Q2 + Q1 \tag{3.5}$$

$$Q5 = A_5 h_5 (Tc8 - \frac{1}{2}(Tc2 + Tc3)) = \frac{(Tc8 - \frac{1}{2}(Tc2 + Tc3))}{R_5} \tag{3.6}$$

$$Q6 = \frac{L_6 (Tc8 - T_{static\_structure})}{k_6 A_6} = \frac{(Tc8 - T_{static\_structure})}{R_6} \tag{3.7}$$

$$Q7 = A_7 h_7 (Tc8 - \frac{1}{2}(Tc3 + Tc4)) = \frac{(Tc8 - \frac{1}{2}(Tc3 + Tc4))}{R_7} \tag{3.8}$$

$$Q8 = \frac{L_8 (Tc9 - Tc8)}{k_8 A_8} = \frac{(Tc9 - Tc8)}{R_8} \tag{3.9}$$

$$Q8 = Q7 + Q6 + Q5 + Q4 \tag{3.10}$$

$$Q9 = A_9 h_9 (T_{combustor\_wall} - \frac{1}{2}(Tc3 + Tc4)) = \frac{(T_{combustor\_wall} - \frac{1}{2}(Tc3 + Tc4))}{R_9} \tag{3.11}$$

$$Q10 = \frac{L_{10} (T_{combustor\_wall} - Tc9)}{k_{10} A_{10}} = \frac{(T_{combustor\_wall} - Tc9)}{R_{10}} \tag{3.12}$$

$$Q11 = A_{11} h_{11} (Tc9 - \frac{1}{2}(Tc4 + Tc5)) = \frac{(Tc9 - \frac{1}{2}(Tc4 + Tc5))}{R_{11}} \tag{3.13}$$

$$Q12 = A_{12} h_{12} (T_{combustor\_wall} - \frac{1}{2}(Tc4 + Tc5)) = \frac{(T_{combustor\_wall} - \frac{1}{2}(Tc4 + Tc5))}{R_{12}} \tag{3.14}$$

$$Q13 = \frac{L_{13} (Tc10 - Tc9)}{k_{13} A_{13}} = \frac{(Tc10 - Tc9)}{R_{13}} \tag{3.15}$$

$$Q13 + Q10 = Q11 + Q8 \tag{3.16}$$

$$Q14 = A_{14}h_{14}(Tc10 - \frac{1}{2}(Tc5 + Tc6)) = \frac{(Tc10 - \frac{1}{2}(Tc5 + Tc6))}{R_{14}} \tag{3.17}$$

$$Q15 = \frac{L_{15}(T_{combustor\_wall} - Tc10)}{k_{15}A_{15}} = \frac{(T_{combustor\_wall} - Tc10)}{R_{15}} \tag{3.18}$$

$$Q16 = \frac{L_{16}(T_{combustor\_wall} - Tc10)}{k_{16}A_{16}} = \frac{(T_{combustor\_wall} - Tc10)}{R_{16}} \tag{3.19}$$

$$Q17 = A_{17}h_{17}(T_{static} - \frac{1}{2}(Tc2 + Tc3)) = \frac{(T_{static} - \frac{1}{2}(Tc2 + Tc3))}{R_{17}} \tag{3.20}$$

$$Q16 + Q15 = Q14 + Q13 \tag{3.21}$$

$$Q1 = \dot{m}_{total}\, Cp_{in1}(Tc1 - T_{inlet}) \tag{3.22}$$

$$Q_{shaft} + Q_{journal\_bearing} + Q3 + Q2 + W_{compressor} = \dot{m}_{total}\, Cp_{12}(Tc2 - Tc1) \tag{3.23}$$

$$Q17 + Q5 = \dot{m}_{total}\, Cp_{23}(Tc3 - Tc2) \tag{3.24}$$

$$Q9 + Q7 = \dot{m}_{combustor}\, Cp_{34}(Tc4 - Tc3) \tag{3.25}$$

$$Q11 + Q12 = \dot{m}_{combustor}\, Cp_{45}(Tc5 - Tc4) \tag{3.26}$$

$$Q14 = \dot{m}_{combustor}\, Cp_{56}(Tc6 - Tc5) \tag{3.27}$$

Equation 12 describes the conduction heat transfer from the combustor side wall to casing block (Tc9) through the structure connecting bridges. **Equation 13** describes the convection heat flow from block (Tc9) to the bypass flow. **Equation 14** describes the convection heat transfer from the combustor side wall to the bypass flow. **Equation 15** describes the conduction heat transfer from casing block (Tc10) to casing block (Tc9). **Equation 16** describes the heat balance for casing block (Tc9). **Equation 17** describes the convection heat transfer from casing block (Tc10) to the bypass flow until the flow enters the combustor. **Equation 18** describes the conduction heat transfer between the bottom combustor wall extension and casing block (Tc10) through the dead flow in between. **Equation 19** describes the conduction heat transfer between the combustor bottom wall extension and casing block (Tc10) through the structure. **Equation 20** describes the convection heat transfer from the casing structure to the diffuser flow. **Equation 21** describes the heat balance for casing block (Tc10). **Equation 22** describes the change in enthalpy for the compressor inlet flow from the heat transfer from casing block (Tc7). **Equation 23** describes the change in stagnation enthalpy for the compressor flow due to the heat transfer and the work input. **Equation 24** describes the change in stagnation enthalpy of the diffuser flow due to the heat transfer from casing block (Tc8) and the static structure. **Equation 25** describes the change in stagnation enthalpy for the bypass flow on top of the combustor due to the heat transfer from casing block (Tc8) and combustor wall. **Equation 26** describes the change in stagnation enthalpy of the bypass flow to the side of the combustor due to the heat transfer from casing block (Tc9) and the combustor wall. **Equation 27** describes the change in

stagnation enthalpy of the bypass flow around the bottom combustor wall before entering the combustor due to the heat transfer from casing block (Tc10).

THERMAL RESISTANCE ESTIMATION FOR MODULE THREE

Compressor inlet: Heat transfer coefficient (Table A.1) for compressor inlet is extracted from representative CFD solution. Inlet area can be calculated from inlet geometry and inlet thermal resistance (R1 in M3) is simply the inverse of the product of area and heat transfer.

Shroud and Shroud Seal: described in module One
Diffuser Passages: described in module Two

Combustor cooling passages: As the flow splits into combustor bypass and combustor flows after the compressor diffuser passage the combustor flow enters the channel around the upper wall of the combustor. The flow in these passages around the combustor remains laminar and is therefore relatively easy to model with well-established analytical expressions or correlations for laminar channel flow. Initially two boundary layers develop on both walls and until the flow develops fully the heat transfer coefficient is modeled with expression for flat plate laminar flow. The Nusselt number depends on Reynolds and Prandtl numbers as expected from Reynolds analogy. Reynolds number is based on entrance length. The entrance length, however, is shorter than the radial length of the combustor and for the rest of the upper flow passage the heat transfer coefficient is modeled with expression for fully developed laminar channel flow. For this case Reynolds number is based on channel hydraulic diameter and Nusselt number is assumed constant = 3.66 [39]. This assumption is also made for the rest of the flow passages wrapping around the combustor because the flow is expected to be fully developed and laminar there. The characteristic length of these passages is the hydraulic diameter or simply the width of the passages. The thermal conductivity of air is a function of temperature and it is estimated at an average temperature for each passage. Heat transfer coefficients can be found from Nusselt number, characteristic length, and conductivity. Thermal resistance (R7, R9, R11, R12, and R14 in M3) can be estimated as the inverse of the product of passage wetted area and heat transfer coefficient [39].

$$h = \frac{Nu * k}{L} \tag{3.28}$$

$$R = \frac{1}{hA} \tag{3.29}$$

Casing blocks: The thermal resistance (R4, R8, R13 and R16 in M3) of the casing blocks is easy to estimate. The heat transfer through the casing structure is by conduction and all that is needed to find the thermal resistance between the blocks is geometry and conductivity of silicon. The resistance is assumed to be the length between the centers of two blocks divided by the product of cross sectional area and conductivity for blocks with constant cross sectional area like the side walls of the combustor. For blocks with disk shape like the upper and bottom casing walls the resistance is the logarithm of the outer to inner radius ratio divided by the product of conductivity, disk thickness and two π [39].

$$R = \frac{\ln\left(\frac{r_{out}}{r_{in}}\right)}{2\pi kH} \tag{3.30}$$

where r is radius, k is thermal conductivity, and H is disk thickness.

Each thermal resistance can be estimated as a combination of these two equations. If additional geometric features are added to the casing design of the engine to introduce more resistance for example in the block right next to the compressor shroud, the resistance of this block should be modified in the code. In the current version of the model each block is assumed isothermal with a temperature at its center representing the average actual temperature of the block.

Combustor wall: The temperature of the combustor wall is assumed known (1100 K), as is the temperature of the combustor gasses (1800 K). This information is based on experimental measurements in a dual zone hydrogen combustor [40].

Connecting bridges: analogous to the ones described in module Two (R10 in M3)

Dead flow region: The space between the extension of the bottom combustor wall and the bottom casing wall (Tc10) is occupied by dead flow. Heat transfer takes place by conduction through the dead flow and the thermal resistance (R15 in M3) between the two walls can be estimated from air conductivity and geometry.

RADIATION HEAT TRANSFER

When high temperatures are present as in the micro-engine combustor the possibility for some radiation heat transfer to occur exists and must be quantified. The first thing to estimate to get an overall idea for the importance of radiation is the total power that the combustor wall can possibly emit towards the compressor. The hot gasses in the combustor (1600-1800 K) or in the turbine (1200-1500 K) are not an issue since silicon is opaque at the high temperatures of the combustor wall or the turbine disk. This means that no radiation will be transmitted through the combustor wall or the turbine disk towards the compressor from outside. The radiation heat transfer will originate from the combustor walls or static structure wall or turbine disk themselves. The temperature of the combustor wall is about 1100 K and the total area of the inner combustor wall is about A = 4.4e-5. Emissivity of silicon at that temperature is 0.7. Therefore the total emitted power is:

$$P = A\varepsilon\sigma T \tag{4.1}$$

where, A is the area of the inner combustor wall, e the emissivity, and T the temperature of the wall [39]. The maximum total power estimated in this manner is 2.5 Watts. Of course, silicone does not behave as a black body and the static structure will reflect a large fraction of this power back towards the combustor absorb some of it, and transmit a fraction towards the compressor. In any case the radiation that would eventually reach the compressor will be some small fraction of the 2.5 Watts which is already a small number compared to the expected total heat transfer to the compressor.

A better estimate can be obtained if the combustor inner wall and the static structure around the compressor are treated as diffuse gray bodies [39]. In this case the total heat transfer taking place by radiation can be estimated in the following manner:

$$Q = \frac{\sigma A_1 (T_1^4 - T_2^4)}{\frac{1}{\varepsilon_1} + \frac{1-\varepsilon_2}{\varepsilon_2}\left(\frac{R_1}{R_2}\right)} \tag{4.2}$$

where, Q is the total heat transfer, T1 (1100K) is the temperature of the combustor wall and T2 (800K) is the temperature of the static structure, ε_1 is the emissivity of combustor wall (0.7) and ε_2 the emissivity of the static structure (0.5), R1 (7mm) and R2 (6.8 mm) are the radii of the combustor wall and the static structure respectively. The total heat transfer to the static structure is estimated to be 1 Watt. Only a small fraction of this 1 Watt, however, will be transmitted towards the compressor because the trasmittance of silicone at that temperature is only around 0.1 for a 1mm thick wall. Therefore, it is reasonable to expect that the heat that eventually reaches the compressor directly from the combustor is much less than 1 Watt which would be two orders of magnitude smaller than the expected combined convective and conductive heat transfer (~ 30–80 Watts).

If the radiation heat transfer that would take place directly between the static structure (let assume 900 K) and the compressor itself (600K) through the journal bearing is estimated in the same manner it turns out to be only 0.06 Watts, three orders of magnitude smaller than the expected total heat to the compressor. The radiation heat transfer between the compressor (600K) and the turbine (1200K) calculated in the same manner is however, about 1.5 Watts. This is not expected to have any major impact on the system performance but is included in the model for completeness. Therefore, all radiation heat transfer except the one from the turbine disk is about two orders of magnitude smaller than the expected combined conduction and convection heat transfer and can be ignored in the model.

APPENDIX B

EFFECT OF COMBUSTOR, CASING, AND STATIC STRUCTURE GEOMETRY ON SYSTEM PERFORMANCE AND SIZE

A concern in the design of the micro-engine is the overall size of the engine determined by the size of the combustor. If the engine becomes too large it may lead to micro-fabrication difficulties and also some of the performance benefit due to the miniature scale may be lost. It was shown that heat addition affects compressor performance. Combustor volume is sensitive to compressor performance. The required changes in compressor volume with changes in heat-transfer to compressor flow can be seen in Figure B.1 (combustor design charts). Since the required combustor volume is proportional to the mass flow and inversely proportional to the pressure ratio it remains approximately invariant with the level of heat transfer to the compressor flow. The effect of the heat transfer is to reduce both mass flow and pressure ratio and for the combustor volume the two effects are balanced for a wide range of heat transfer levels. The required volume increases with increasing turbomachinery size as expected because mass flow increases. If combustor height remains the same and turbomachinery size doubles then combustor outer radius also doubles.

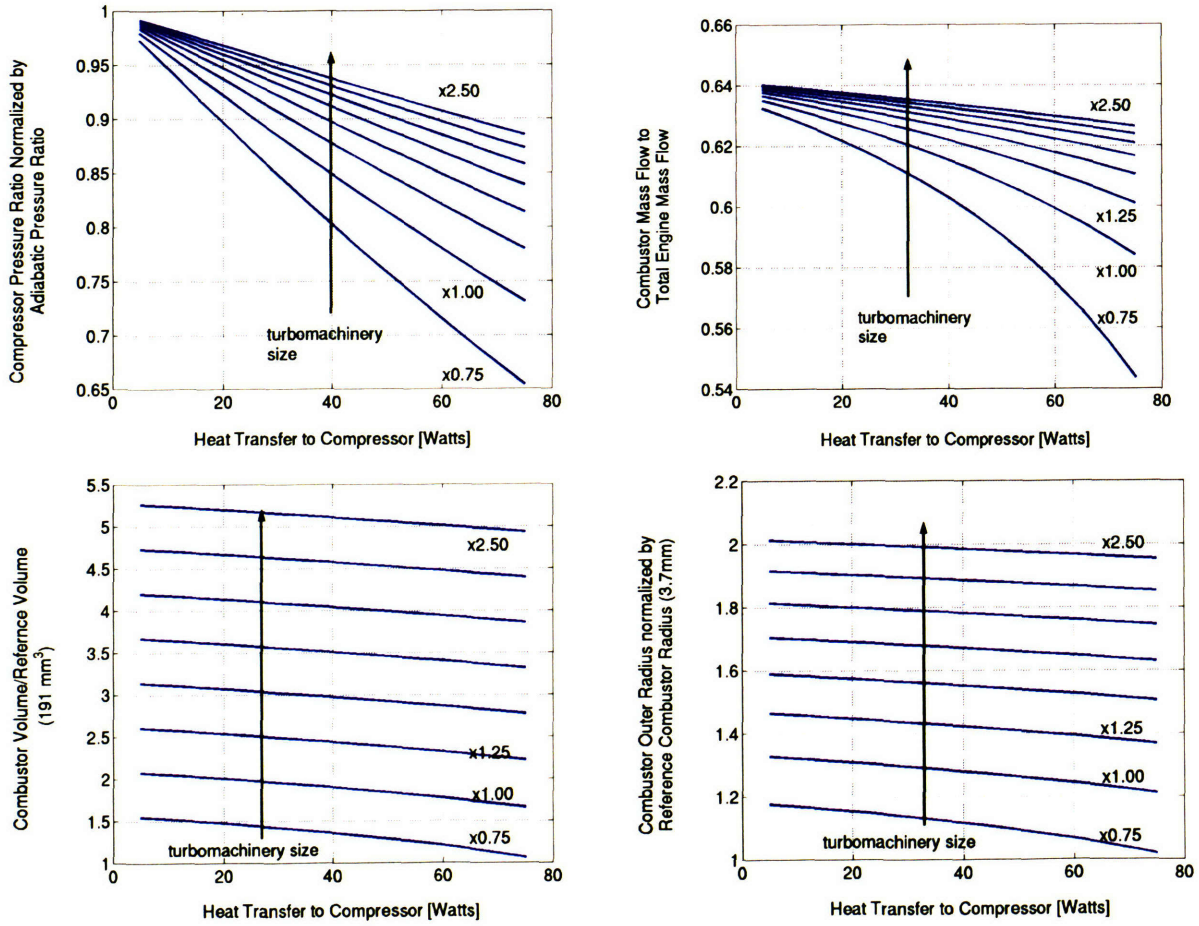

Figure B.1 Effect of heat addition on combustor size (Combustor design charts).

Another effect of interest is related to the heat transfer between the casing, combustor and the cooling flows around the combustor. It is desired to investigate if changing combustor and casing geometry can improve system performance. For example, if combustor height is increased then the combustor radial extent can be reduced to keep the same volume. In this manner the wetted area between the combustor and the cooling flow and between the casing and the cooling flow can be changed. It is possible that some particular geometry may lead to lower casing temperature and to lower overall heat transfer to the compressor flow thus improving system performance. The answer is given in Figure B.2. System performance is insensitive to combustor geometry and also to cooling channels geometry (Fig B.3). The only effect is that by increasing the wetted area the combustor loses more heat (its efficiency is reduced) but the cooling flow picks that heat up and brings it back to the combustor thus keeping the performance the same. There is a perfect balance between combustor efficiency and regeneration effectiveness because for the investigated range of parameters the cooling flows never become thermally fully developed due to the high mass flows. Heat passes both from the combustor and the casing structures into the cooling flow and it is flushed back to the combustor. The cooling channels can simply be viewed as part of the combustor.

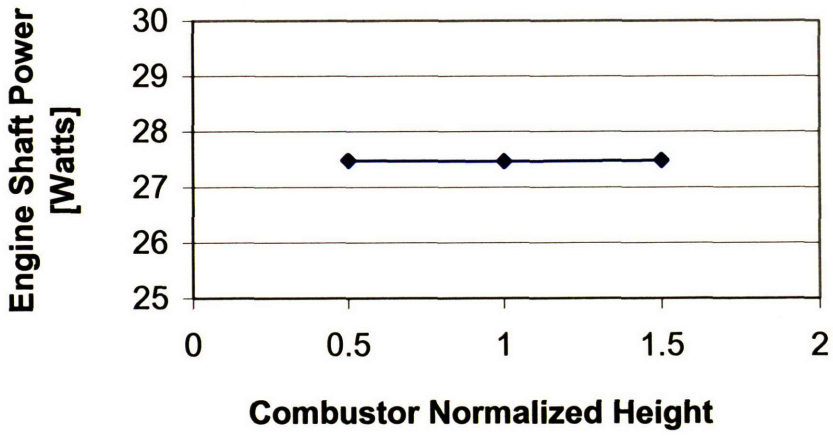

Figure B.2. Effect of combustor geometry on engine net power.

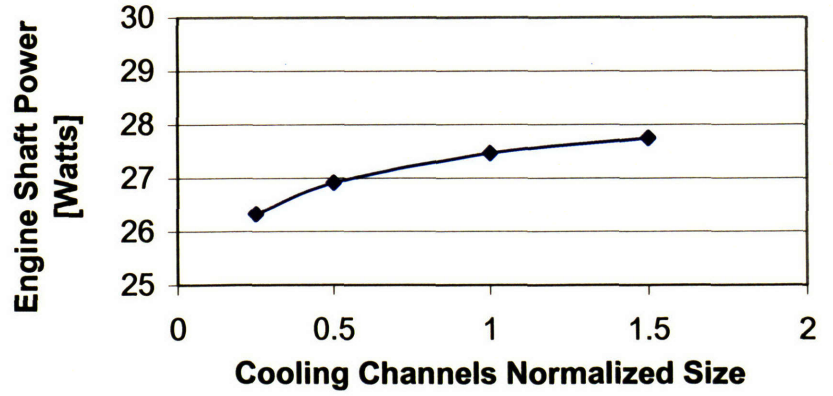

Figure B.3 Effect of cooling channels geometry on engine net power.

THERMAL ISOLATION SHAFT CONCEPT FOR BASELINE DESIGN

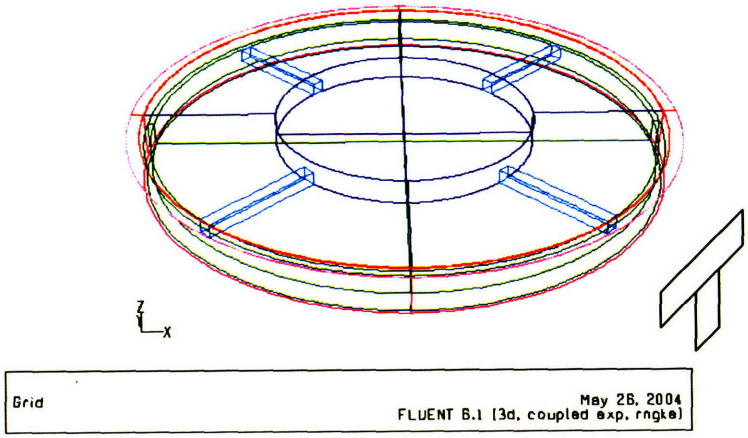

Figure B.4 Thermal isolation shaft for baseline design using connecting T bridges [34].

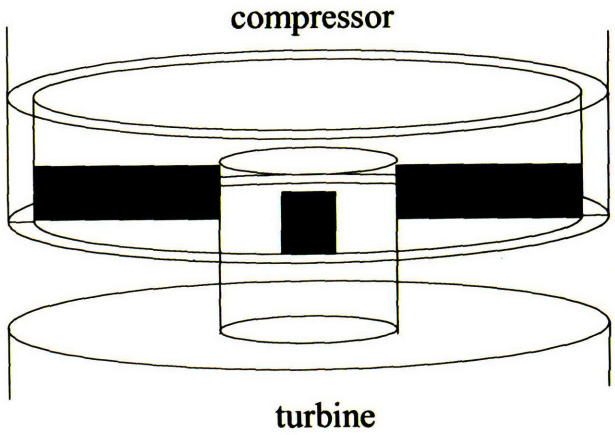

Figure B.5 Thermal isolation shaft for baseline design using simple connecting bridges [34].

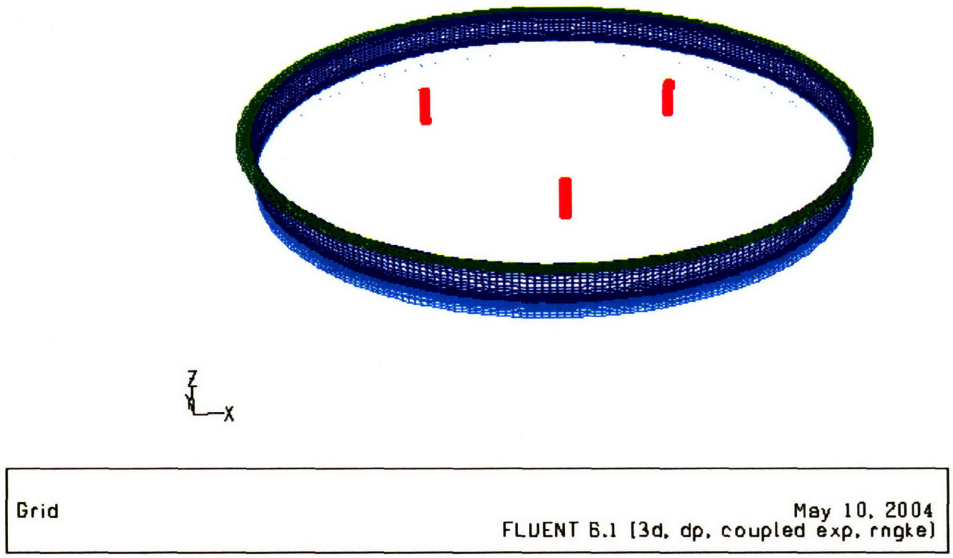

Figure B.6 Thermal isolation shaft for alternative design using simple columns

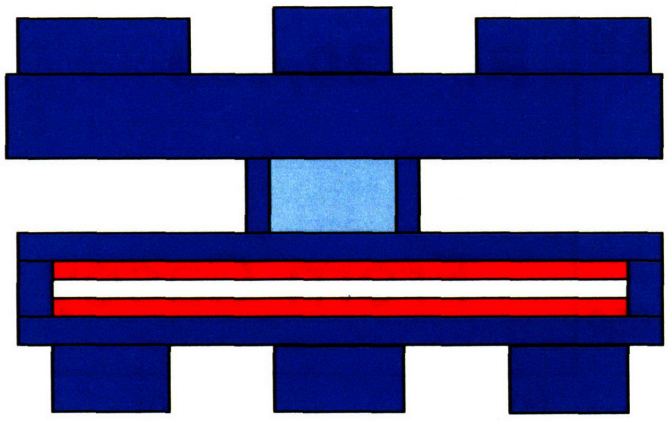

Figure B.7 Two wafer turbine disk concept to allow bonding of isolation shaft to turbine disk [39].

PREVIOUS WORK ON TURBOMACHINERY

This section provides details about experimental and computational results from available previous work.

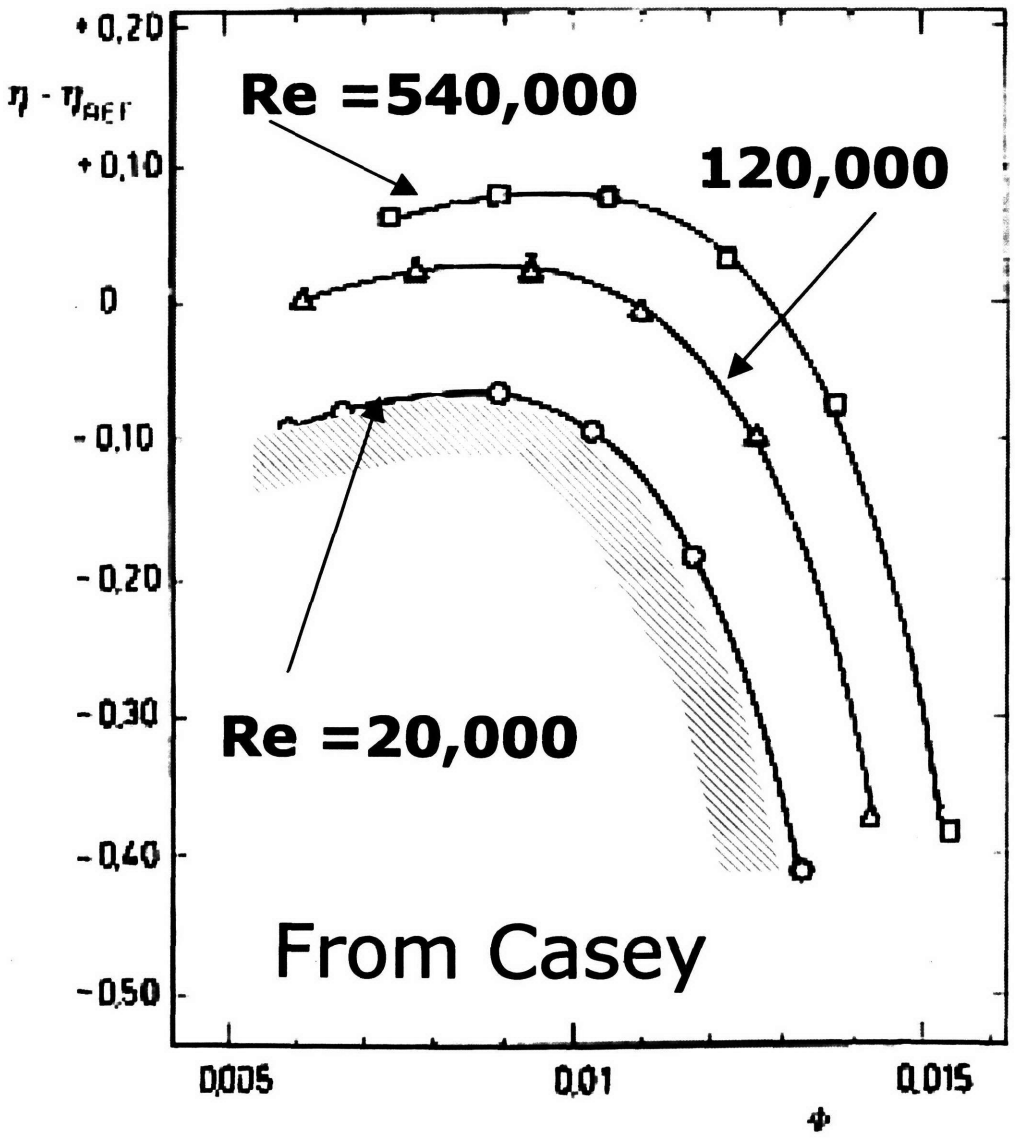

Figure B.8 Effect of Reynolds number on a centrifugal stage performance [15].

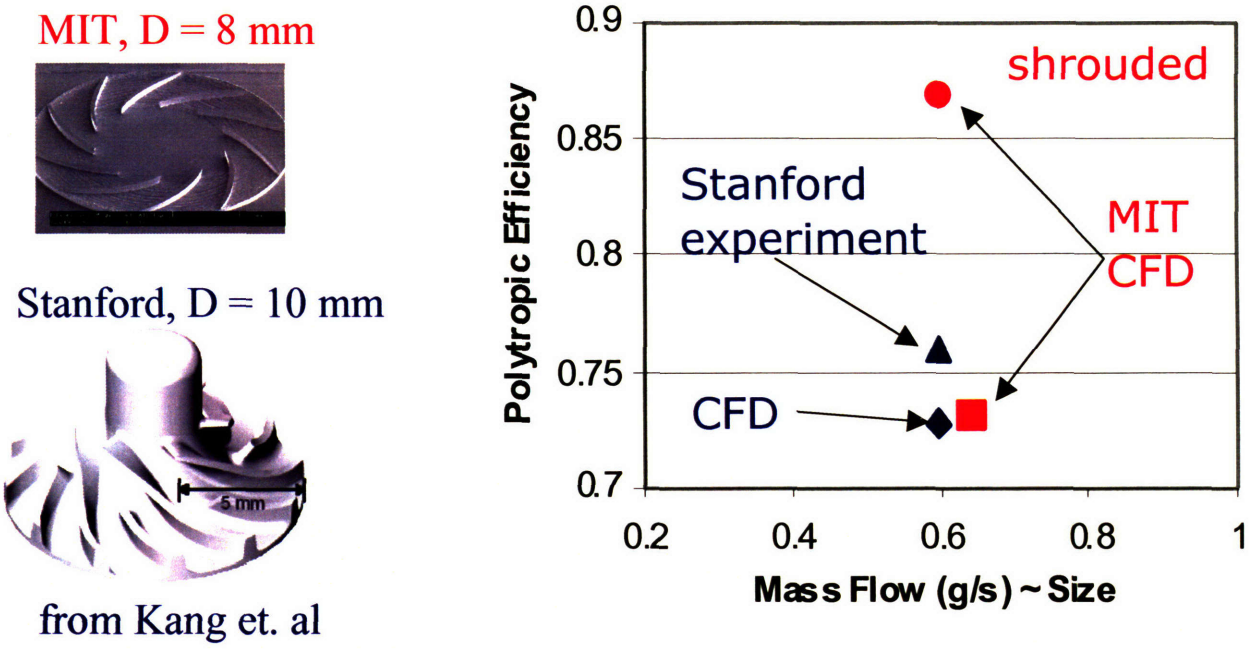

Figure B.9 Effect of casing drag and boundary layer dissipation on micro-impeller performance [18]

EXAMPLE OUTPUT FROM SYSTEM MODEL

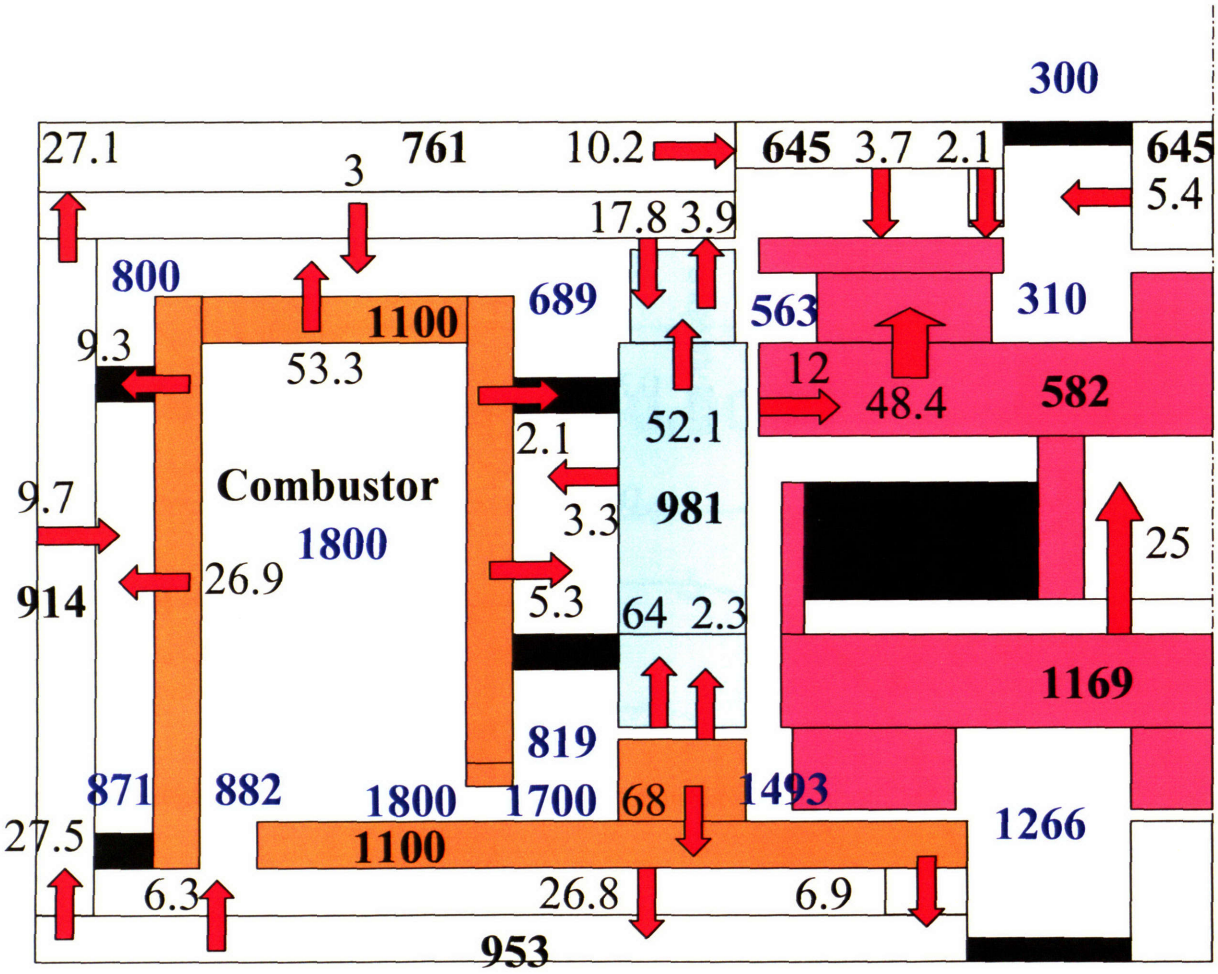

Figure B.10 Heat transfer model output.

An example solution from the heat transfer model is provided in Fig B10 for an engine with typical geometry, effective turbine inlet temperature of 1490 K, and 30% of SiC reinforcement in the turbine disk. This engine can produce 9 Watts of power at system efficiency of 1.7 %. In Figure B.10 the heat flows are in Watts represented by the red arrows, the structure temperatures are in degrees Kelvin (in bold black numbers), and the flow temperatures are in Kelvin (in blue numbers). The convergence criteria can be modified. Currently it is selected to be 0.5 Watts for heat transfer, 1 degree K for temperatures, and 1 degree angle for geometry. More strict criteria do not change the results appreciably and are not used because the solution time increases.

IMPELLER FLOW-FIELD FROM 3-D CFD (FLUENT)

IMPELLER GEOMETRY		
blade span (constant)	800	um
blade leading edge	4	mm
blade trailing edge	8	mm
tip speed	450	m/s
wall temperature	500	K
shroud	yes	
blade inlet angle	55	degrees
blade exit angle	45	degrees
blade number	20	
inlet	smooth	
PERFORMANCE		
mass flow	2.6	g/s
isentropic efficiency	60%	
pressure ratio	2.3	

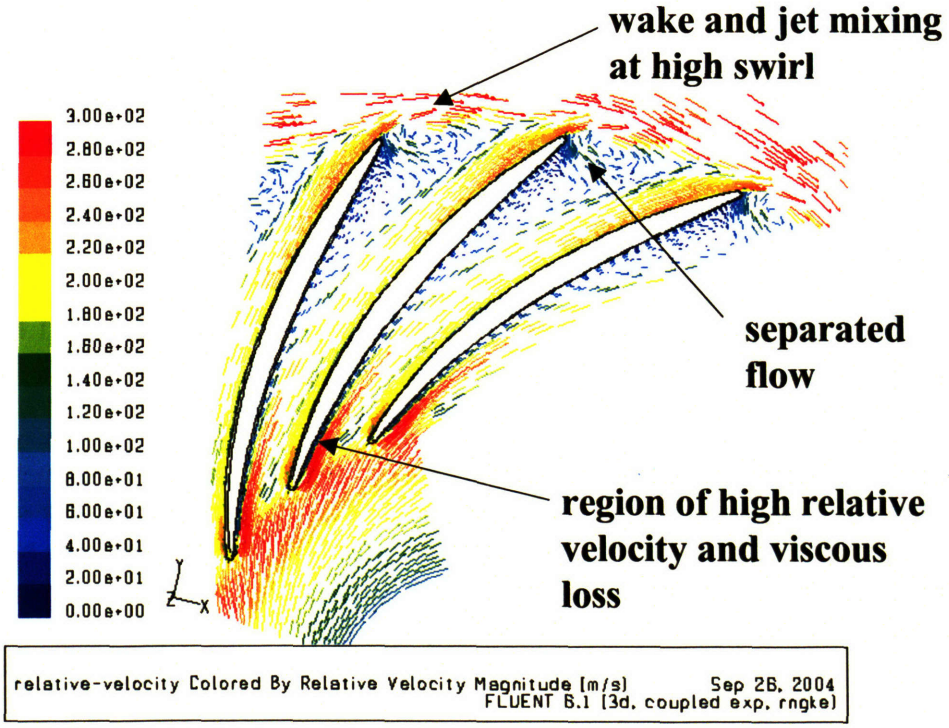

B.11. Impeller relative velocity at mid-span

Figure B.11 presents a plot of impeller relative velocity at mid-span. Several important flow-features are indicated. The flow separates from the suction blade surface towards the exit of the impeller passage and a recirculation zone can be seen. This separation, however, does not lead to appreciable mixing losses due to the mixing at high exit swirl. The mixing region is also indicated on the figure. The highest relative velocity in the passage is near the leading edge of the blades. These regions are associated with high viscous boundary layer losses.

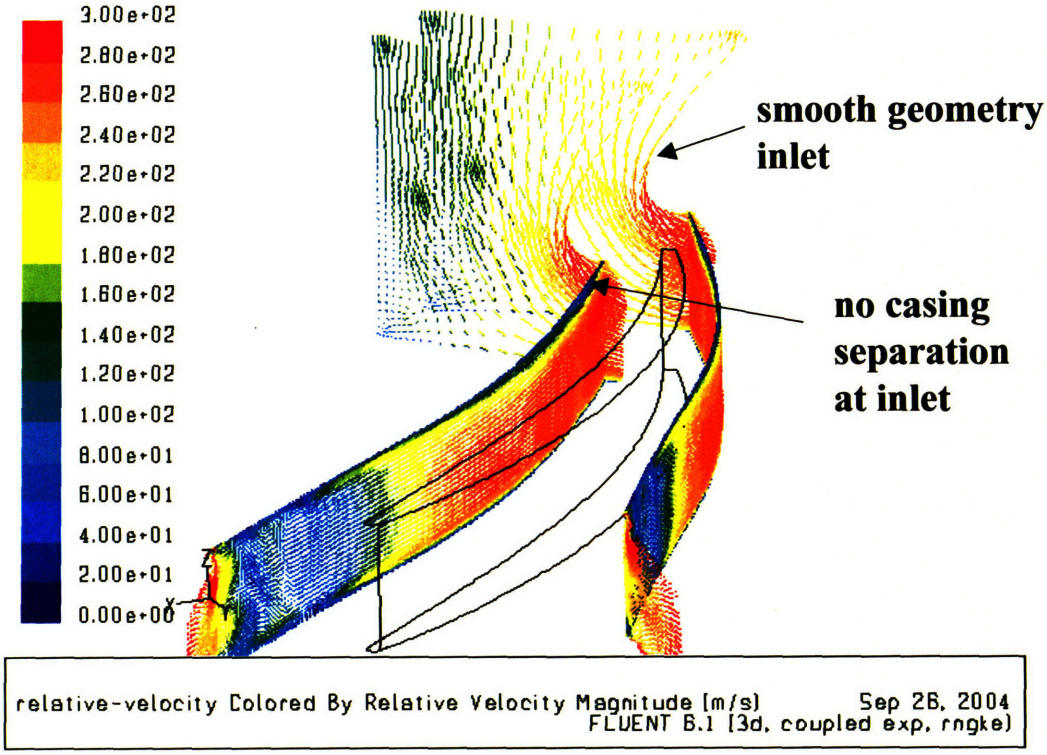

B.12. Impeller relative velocity at mid-pitch

The incorporation of a smooth geometry inlet is shown on figure B.12. The consequence of this modification is that the casing separation region at impeller passage inlet is almost completely eliminated. This eliminates the mismatch between blade angle and flow direction and reduces the loss associated with the inlet by 3-4 efficiency points.

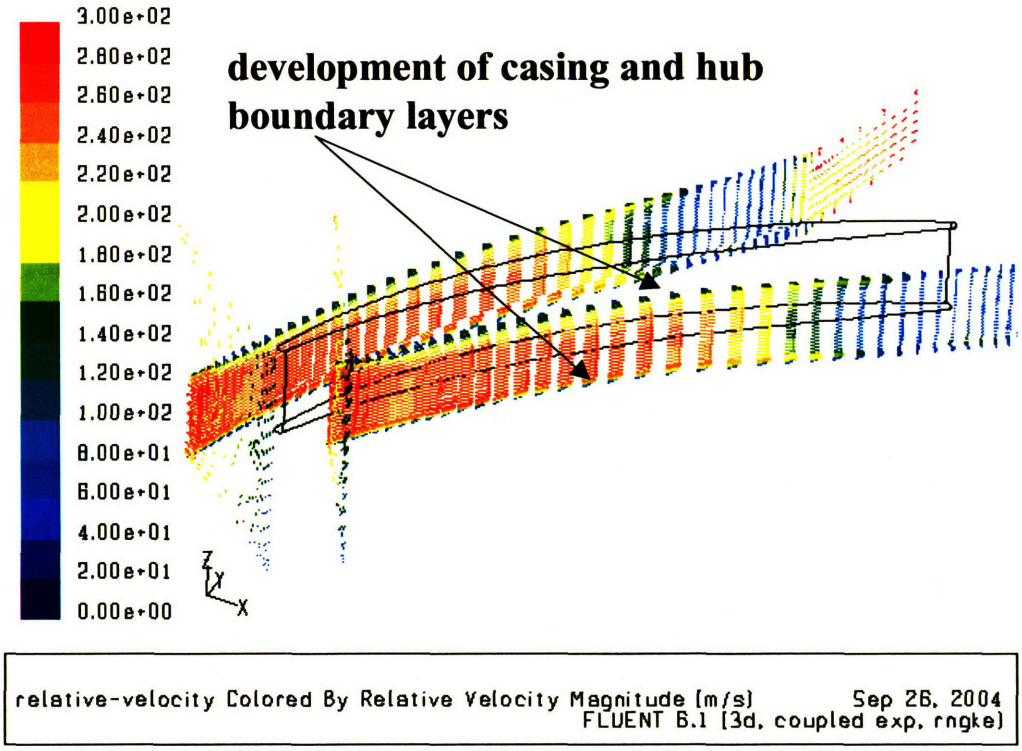

B.13. Impeller relative velocity at mid-pitch

Figure B.13 presents the development of the hub and casing boundary layers in the impeller passage. Again it can be noted that casing separation at inlet is absent. There are no major hub or casing separation regions within the whole passage. The velocity profile (turbulent flow) assumes a similar shape near the middle of the passage, which indicates a fully developed flow. The shape of the velocity profile changes at the end of the passage due to the large separated region on the blade suction surface.

Figure B.14 presents the increase in entropy in the blade passage from inlet to exit. It can be observed that towards the exit of the passage the inviscid flow region has disappeared. Viscous effects have diffused to fill the whole flow. This is related to the characteristic low Reynolds number (~4000).

In Figure B.15 the addition of heat to the impeller flow is shown. The enthalpy of the flow is high near all passage walls because of the heat transfer that is taking place. It can be observed that intense increase in enthalpy from the walls takes place near the impeller inlet. The heating of the impeller flow makes it harder to compress the air and this thermodynamic effect results in appreciable reduction in isentropic efficiency.

Figures B15-B19 present static pressure and temperature contours in the impeller. It can be noted that the pressure rise in the radial direction is relatively uniform which indicates that most of the pressure rise is due to the centrifugal effect and a small fraction is because of diffusion.

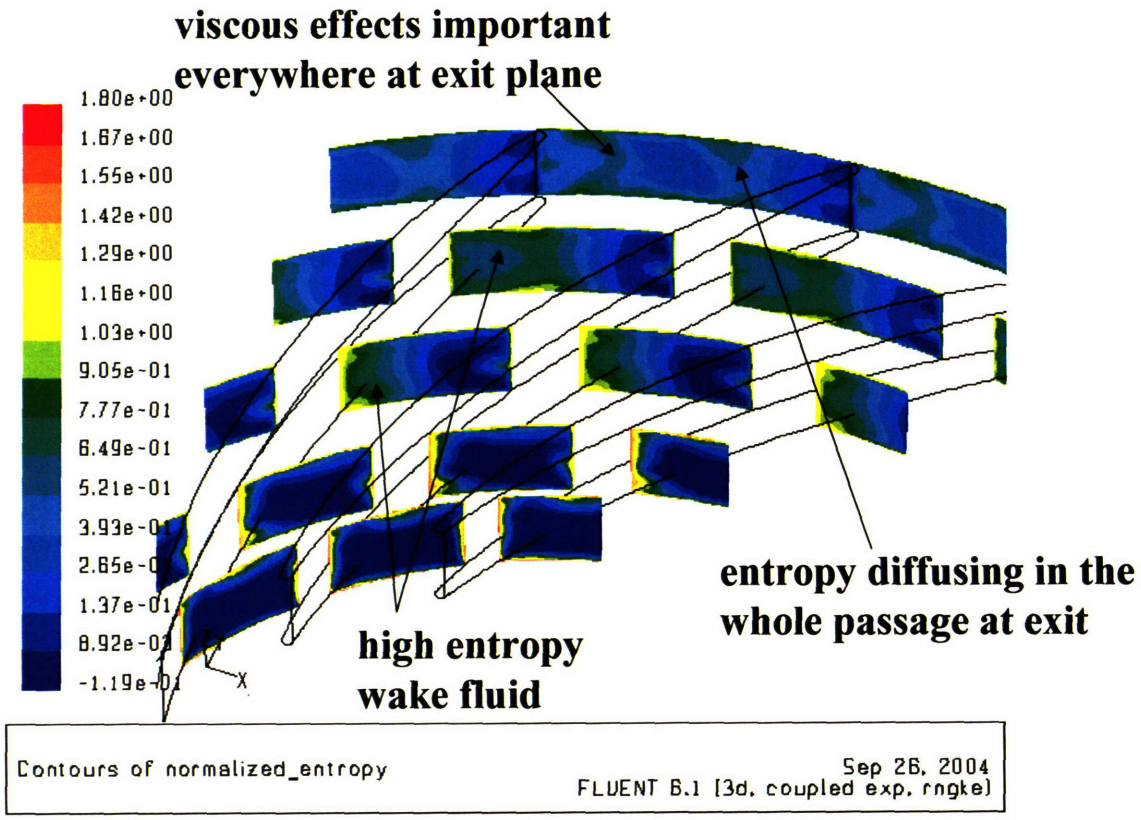

B.14. Impeller entropy increase for different radial planes.

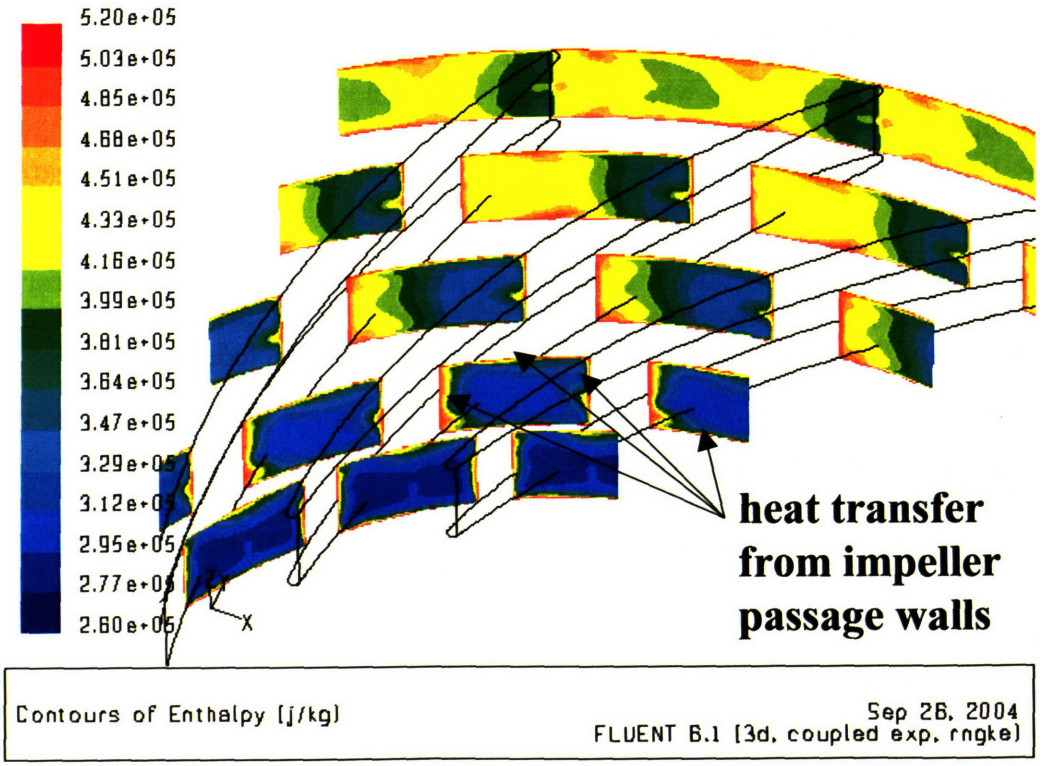

B.15. Impeller enthalpy for different radial planes.

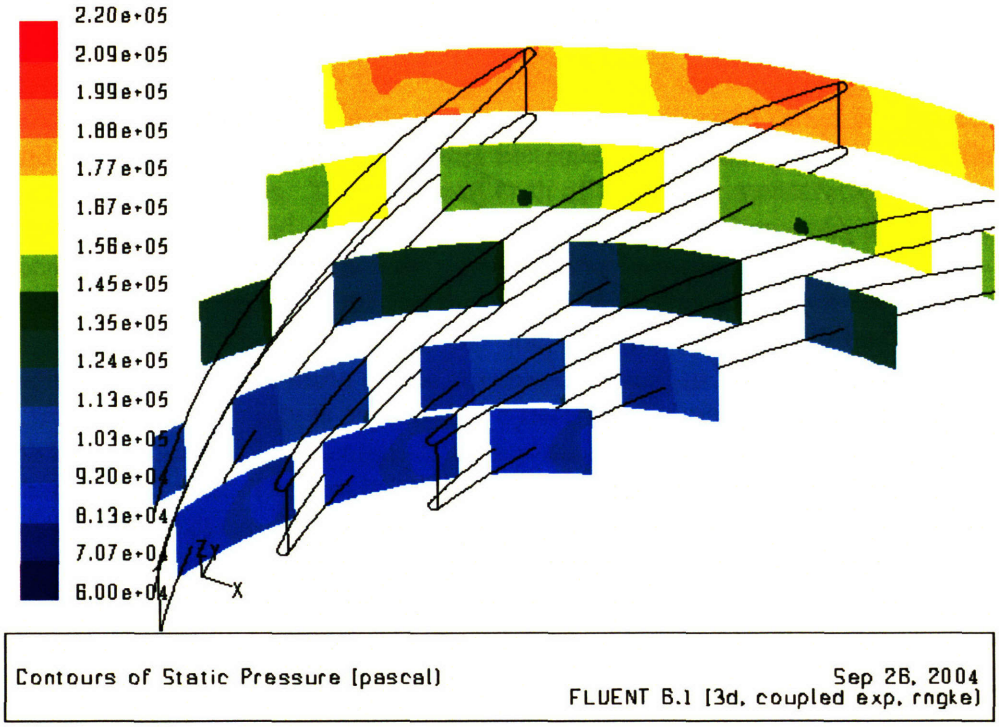

B.16. Impeller static pressure for different radial planes.

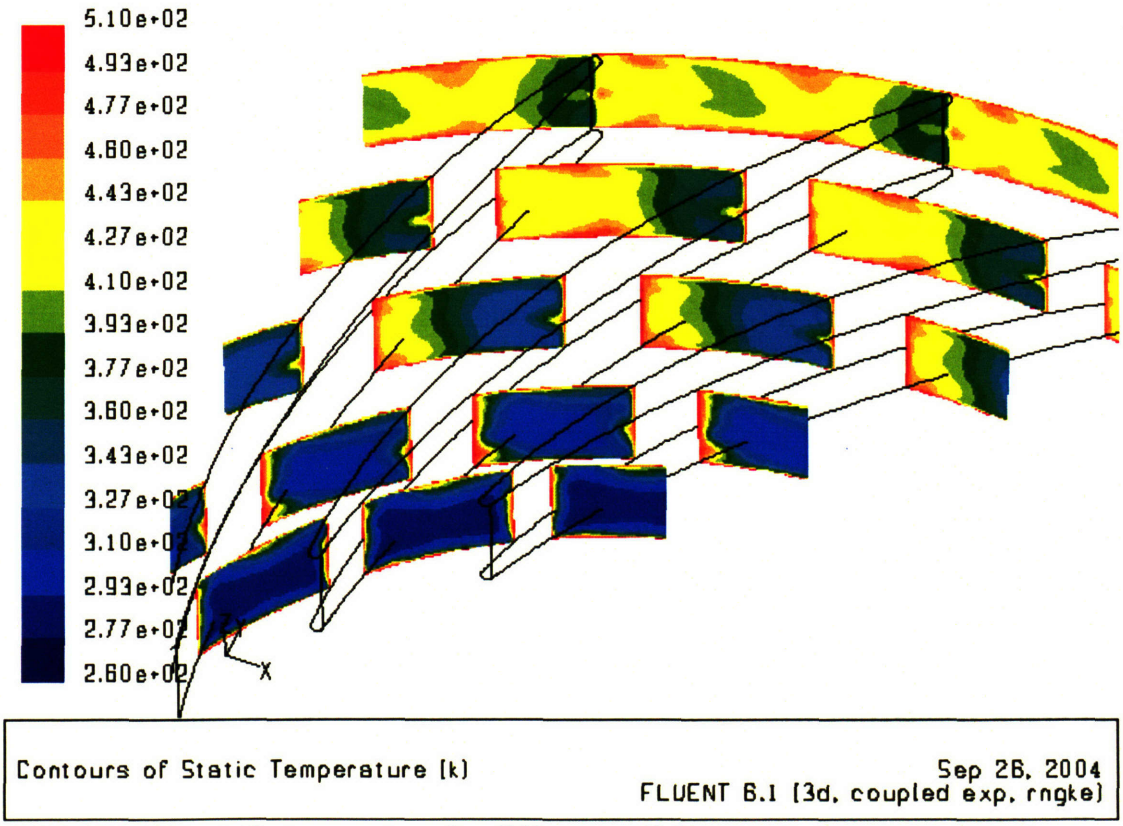

B.17. Impeller static temperature for different radial planes.

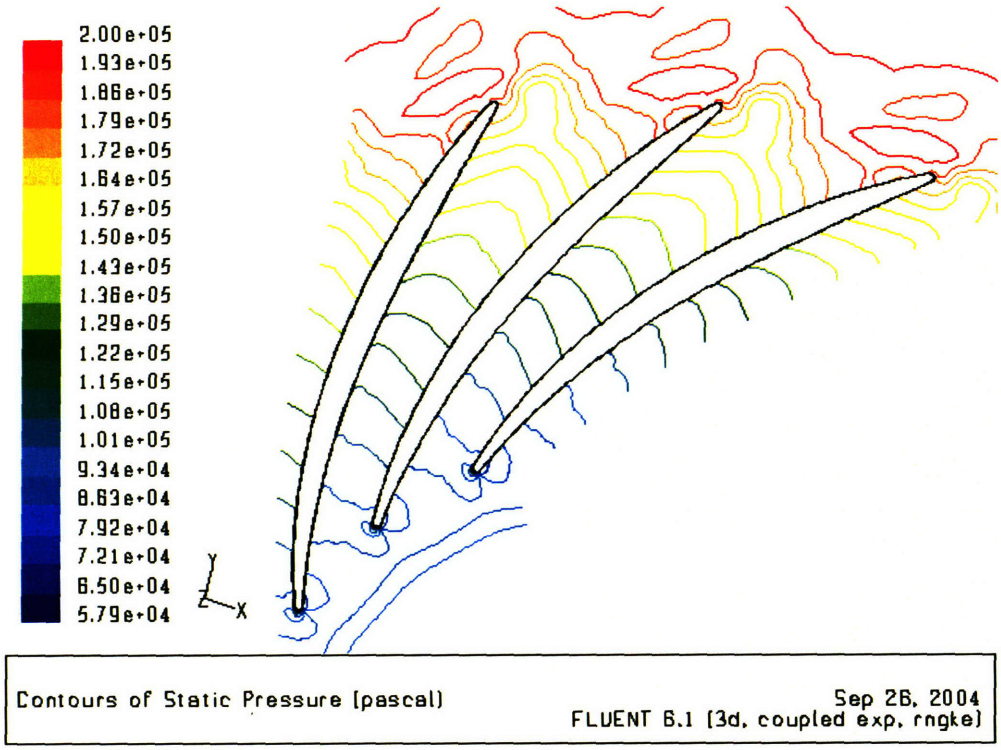

B.18. Impeller static pressure contours at mid-span.

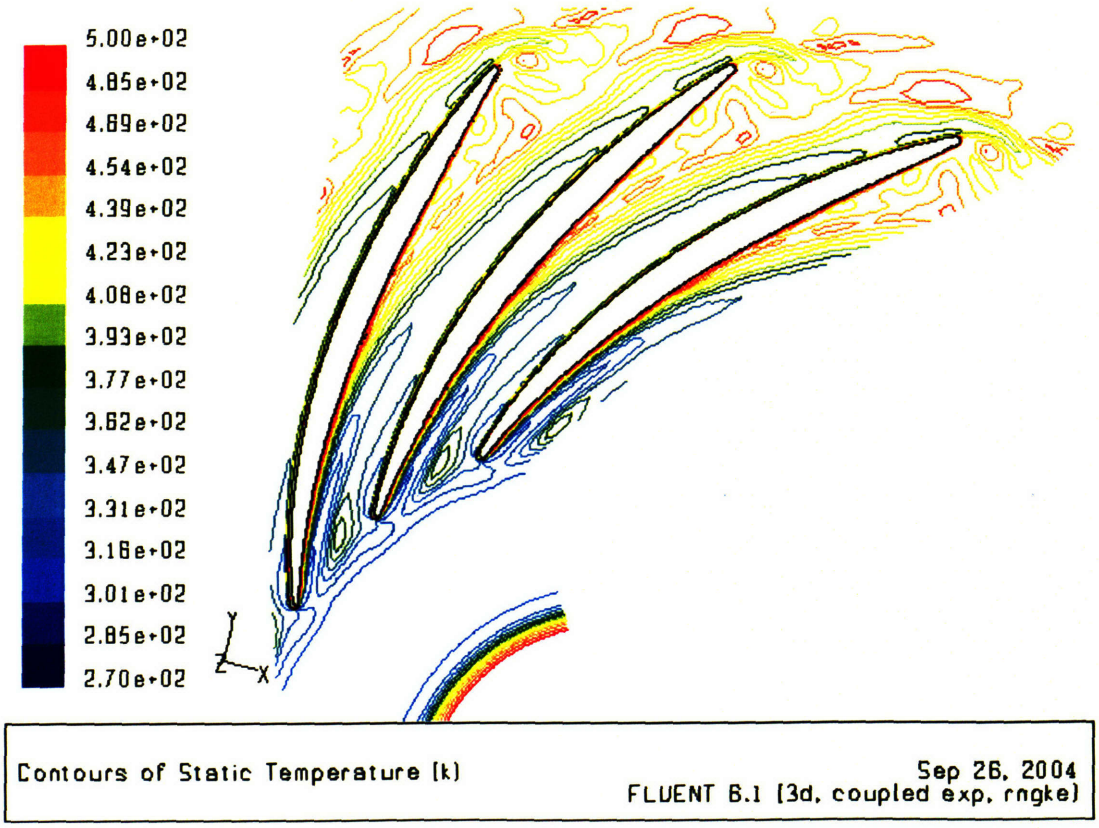

B.19. Impeller static temperature contours at mid-span.

EFFECT OF ENGINE SIZE ON MICRO-ENGINE POWER DENSITY

It was found in Chapter 5 that the performance of the micro-engine (efficiency, net power, and power density) increases continuously for the investigated range with increasing turbomachinery and engine size. The reason for this increase is the scaling of heat transfer and parasitic power loss in micro-engines. The effects of both of these detrimental mechanisms increase slower than engine mass-flow and net power. For a large engine, however, a reduction in size leads to an increase in the engine power density as a consequence of the cube-square scaling law. Therefore, it is expected that as the engine grows in size from the current micro-scale, the net heat transfer to the compressor and the parasitic losses will become less important and the increase in engine volume would reverse the trend in power density. An optimal engine size in terms of power density is expected. To determine approximately this optimal gas turbine size the system model is implemented. The key assumption in this study is that engine layout does not change with size. The results of the study are shown in Figure B.20 indicating that the proposed micro-engine design B is near the optimal gas turbine size in terms of power density. Since the investigated range of engine sizes is small, the assumption to keep the engine layout the same remains valid.

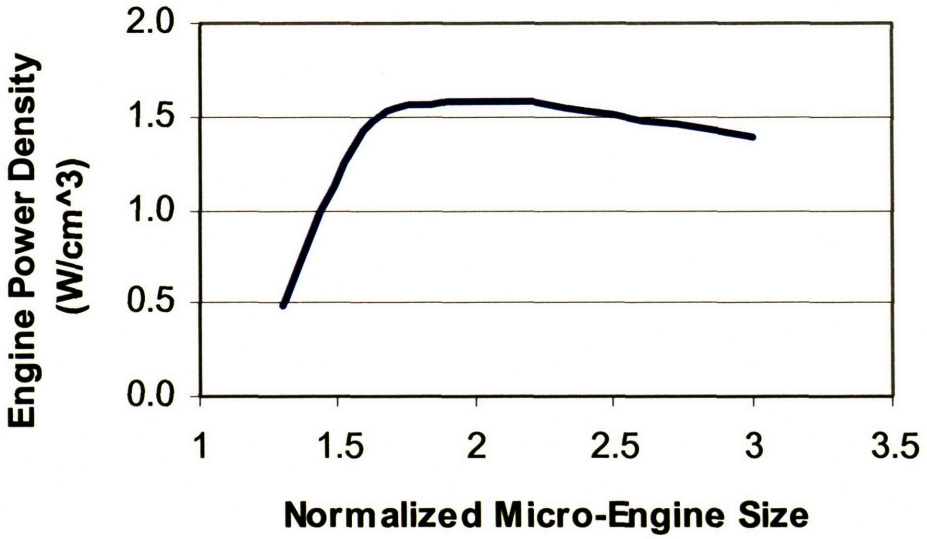

Figure B.20 Effect of engine size on power density